CHEMICAL REVIEWS

pubs.acs.org/CR

Review

Molecular Gold Nanoclusters for Advanced NIR-II Bioimaging and Therapy

Ani Baghdasaryan and Hongjie Dai*

Cite This: *Chem. Rev.* 2025, 125, 5195−5227

Read Online

ACCESS | Metrics & More | Article Recommendations

ABSTRACT: Small thiolate-protected gold molecular clusters have gained significant interest in research due to their unique size-dependent properties. Their molecular to nanoscale sizes lead to distinctive quantum confinement effects, resulting in a discrete electronic energy band gap structure and molecule-like properties, including HOMO−LUMO electronic transitions, enhanced photoluminescence, and intrinsic magnetism and chirality. Near-infrared II (NIR-II, 1000−3000 nm) emissive gold clusters have emerged as a fascinating class of nanomaterials that are well-suited for biomedical applications. The unique combination of stability, biocompatibility, and tunable emission properties position them as valuable tools for high-resolution and deep-tissue imaging, with potential real-world applications ranging from disease diagnostics and prognosis to therapeutics. In this review, we focus on the NIR-II photoluminescence properties of gold molecular clusters for preclinical in vivo NIR-II imaging of vasculature, brain, kidney, liver, and gastrointestinal organs, and molecular targeted tumor imaging and theranostic treatment. The imaging capabilities combined with fast excretion and a high safety profile make molecular gold clusters highly promising for clinical translation.

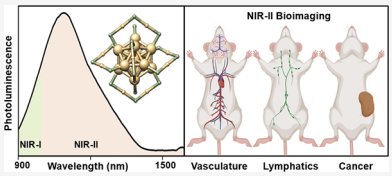

CONTENTS

Received: October 27, 2024
Revised: April 23, 2025
Accepted: April 30, 2025
Published: May 28, 2025

https://doi.org/10.1021/acs.chemrev.4c00835
Chem. Rev. 2025, 125, 5195−5227

1. INTRODUCTION

Atomically precise gold nanoclusters (AuNCs), referred to as molecular gold nanoclusters, constitute intriguing nanoscale materials with a core diameter below 2 nm, featuring unique size-dependent properties primarily arising from quantum confinement effects.[1,2] The quantization of the conduction band within these nanoclusters results in discrete electronic energy band gap structures, imparting distinct molecule-like characteristics.[3] These include features like HOMO (highest occupied molecular orbital)−LUMO (lowest unoccupied molecular orbital) electronic transitions, enhanced and tunable photoluminescence, and the presence of intrinsic molecular chirality and magnetism.[1−3] Following the first report on the synthesis of thiolate-protected Au nanoclusters by Brust−Schiffrin in 1994,[4] the synthetic methodologies employed in the synthesis of metal clusters with precise atomic compositions have undergone substantial evolution.[5−8] In the Brust−Schiffrin method, the nucleation and growth of metal nanoclusters are initiated by encapsulating nascent gold cores with a monolayer of thiol ligands following reduction within a biphasic water/organic solvent system.[4] The thiol monolayer plays a critical role in stabilizing the formed gold nanoclusters, effectively preventing aggregation by passivating the surface and thereby enhancing their colloidal stability. However, challenges persist in achieving absolute control over size distribution as the ligand-mediated reduction process frequently results in a polydisperse mixture of nanoclusters with varying nuclearities. To mitigate this issue, postsynthetic refinement strategies, including ligand exchange[9−12] and size focusing strategy (etching processes),[13−16] have been developed. Ligand exchange involves the substitution of the original stabilizing thiols with alternative ligands possessing stronger binding affinities or steric constraints, thereby influencing the thermodynamic stability of the specific cluster sizes. Meanwhile, the size-focusing strategy, typically achieved by employing an excess of thiol ligands, enables the selective dissolution of larger, less stable aggregates while promoting the formation of atomically precise, ultrasmall gold clusters with well-defined compositions.[13−16] This process leverages the dynamic nature of metal−ligand interactions, where excessive thiols induce a ligand-mediated etching effect, effectively breaking down larger clusters and facilitating the reorganization of gold atoms into thermodynamically favored nuclearities. Additionally, in the ligand exchange induced size/structure transformations (LEIST) strategy,[17−20] the ligand exchange can trigger unconventional and unexpected structural rearrangements, resulting in the formation of gold nanoclusters with distinct geometries and nuclearities. This process involves ligand-mediated reconfiguration of the cluster core, where selective removal and incorporation of gold atoms, coupled with ligand-induced surface restructuring, drive the emergence of new stable or metastable cluster species. Therefore, the size-focusing synthesis[16] and LEIST[9,17] became key avenues to prepare (mostly) spherical nanoclusters with flexible ligand shell structures. These approaches not only are instrumental in the diverse synthesis of clusters but also play a crucial role in finely tuning their optical properties in a controlled and systematic manner. Standardization of synthetic protocols and the implementation of rigorous control mechanisms during cluster growth under well-defined reaction parameters ensure high purity and reproducibility of certain cluster sizes. This development has significant implications for various applications in nanoscience, introducing a framework for the systematic exploration of novel functionalities and paving the way for advancements in nanotechnology and nanomedicine.

Intense effort in the past decades led to a library of atomically precise gold nanoclusters with a common formula of $Au_n(SR)_m^q$, where n is the number of gold atoms in the cluster ($15 \leq n \leq 246$), m is the number of thiol ligands (SR) ($13 \leq m \leq 80$), and q is the net charge of the cluster (negative, neutral and positive).[1,2,21] The ability to fine-tune the physicochemical properties of these clusters by controlling the number of gold atoms[21] and choosing appropriate protective ligands (monothiols,[7,22] bidentate thiol ligands,[11,23,24] phosphine ligands[25]), imparted rich structures and properties and rendered them effective nanoscale catalytic systems[8,26,27] or imaging and diagnostics agents for biomedical research.[28−32] The catalytic,[26] chiral,[33] and magnetic[34] properties of nanoclusters have garnered extensive attention and comprehensively reviewed in recent literature.[8,26,27,33,34] The scope of this review is to first summarize the optical properties of AuNCs and then focus on recent work on bioimaging utilizing the NIR-II (1000−3000 nm) fluorescence of gold nanoclusters.

2. IN VIVO FLUORESCENCE IMAGING IN NIR-II WINDOW

2.1. Synthesis of Molecular Gold Nanoclusters

The synthesis of atomically precise gold nanoclusters is an intricate process highly depending on reaction conditions (temperature, solvent, reducing agent, pH) and protective ligands (thiolates, phosphates, etc.).[1,2] These factors are pivotal in determining the size, stability, and functionality of the resulting clusters.[35] The nature and concentration of the reducing agent are crucial for controlling the nucleation and growth of gold clusters, while the choice of the ligand is fundamental to the stability and properties of gold clusters.[36] Ligands with thiol groups (−SH) are particularly effective in binding to gold surfaces, providing strong stabilization through the formation of Au−S bonds.[37] The molecular structure of the ligand, including its length, rigidity, and functional groups, influences the overall size and shape of the obtained clusters.[7] In applications where biocompatibility is essential, such as in biomedical imaging and drug delivery, the solubility of the clusters in biological media is critical. Hydrophilic ligands, such as glutathione (a tripeptide, GSH),[38] captopril,[39] etc.[40,41] not only stabilize the clusters but also render them soluble in aqueous environments, facilitating their interaction with biological systems.

Since the first report on the synthesis of thiolate-protected Au nanoclusters by Brust−Schiffrin in 1994,[4] several strategies have been developed over the years to prepare metal clusters with precise atomic compositions.[5−8] The size-focusing synthesis[16] and ligand exchange induced size/structure transformations,[9,17] pioneered by Jin's and Pradeep's laboratories, have emerged as key avenues to prepare (mostly) spherical nanoclusters with flexible ligand shell structures. For example, in size-focusing synthesis, the etching of an initially formed clusters species (obtained via kinetic control during reduction process) at relatively high temperatures in the presence of thiol ligands can selectively transform into thermodynamically stable cluster sizes (thermodynamic control).[35] $Au_{25}(SR)_{18}$ and $Au_{38}(SR)_{24}$ clusters are in fact produced during size-focusing synthesis (SR refers to 2-phenylethanethiol ligand).[10,11] Ligand exchange induced size/structure transformations are usually postsynthetic strategies for obtaining structurally different clusters from initial

https://doi.org/10.1021/acs.chemrev.4c00835
Chem. Rev. 2025, 125, 5195−5227

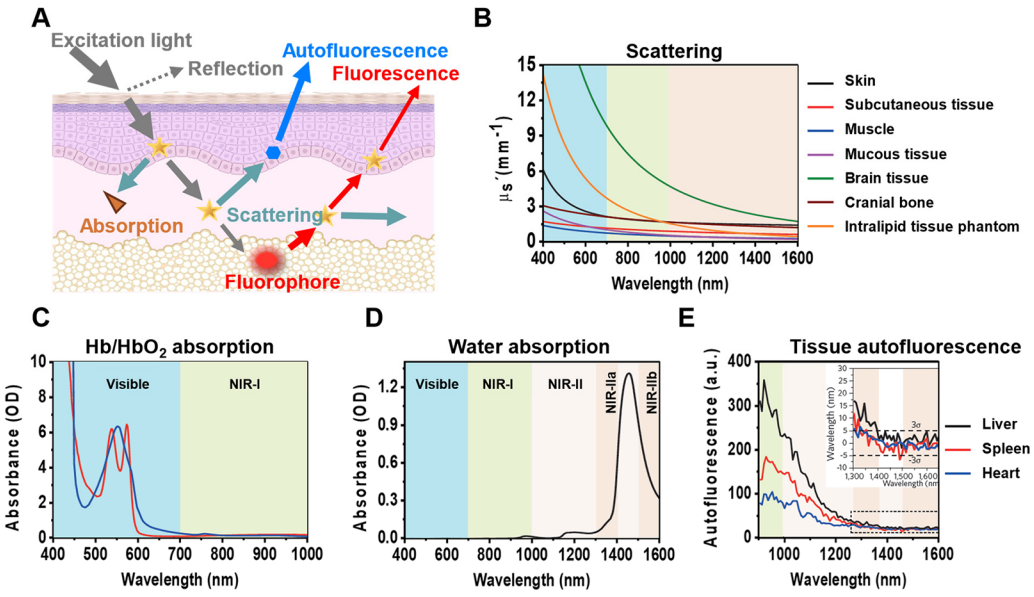

Figure 1. (A) Schematic representation of light-tissue interactions in biological tissue. Color codes of symbols: excitation light: solid gray, interface reflection: dashed gray, fluorescence: red, autofluorescence: blue, scattering: cyan, absorption: orange. Created with BioRender.com. (B) Reduced scattering coefficients for diverse biological tissues and intralipid tissue phantoms across wavelengths ranging from 400 to 1700 nm.[70] (C) Absorption spectra of oxyhemoglobin (red) and deoxyhemoglobin (blue) in human blood (1 mm-long path). (D) Absorption spectrum of water (1 mm-long path). OD, optical density. (E) Autofluorescence spectra of ex vivo mouse liver (black), spleen (red), and heart tissue (blue) under 808 nm excitation light with zero autofluorescence in the >1500 nm NIR-II window. Inset: Autofluorescence spectra at high wavelengths. Panels B−E are reproduced with permission from ref 70. Copyright 2017, Springer Nature.

atomically precise cluster (precursor) in the presence of excess ligand (different than in a precursor) that are otherwise difficult or impossible to obtain via size-focusing.[35] For example, face-centered cubic (fcc) $Au_{36}(SR')_{24}$ cluster can only be obtained from the size/structure transformation of bi-icosahedral $Au_{38}(SR)_{24}$ cluster in the presence of excess −SR′ ligands (−SR: 2-phenylethanethiol, −SR′: 4-*tert*-butylbenzenelthiol).[42]

Generally, organic thiol ligands offer greater control over the synthesis process, allowing researchers to precisely tune the size, shape, and composition of the gold nanoclusters. This, on the other hand, facilitates systematic investigations of the structure−property relationships of these clusters. However, achieving atomic precision with water-soluble gold nanoclusters is considerably more challenging. This difficulty further complicates the investigation of how clusters of different sizes and shapes interact with the biological environment. Recently, $Au_{22}(GSH)_{18}$,[43,44] $Au_{25}(GSH)_{18}$,[38,45] $Au_{25}(MBA)_{18}$[46] (note, MBA-protected Au_{25} nanoclusters were found to bind to bovine serum albumin (BSA)) and $Au_{44}(MBA)_{26}$[47,48] clusters (where MBA denotes 4-mercaptobenzoic acid ligand) were synthesized with high yield and purity via a one-pot reduction process at room temperature within an aqueous medium. Subsequent purification steps yielded highly monodispersed, single-sized clusters in aqueous solutions, rendering them suitable for various bio applications. Other ligands, including amino acids and peptides,[49] proteins and other biomolecules,[50] have also been successfully applied for the preparation of gold nanoclusters; however, in most cases, their structural information remains unknown.

The Xie lab has developed several scalable methods for synthesizing gram-scale gold nanoclusters with atomic precision. The NaOH-mediated $NaBH_4$ reduction method allowed for the rapid production of over one gram of thiolate-protected Au_{25} clusters.[41] Through the introduction of a CO-reduction process, the team achieved scalability for synthesizing Au_{10-12}, Au_{15}, Au_{18}, and Au_{25} clusters protected by glutathione ligands.[51] Recently, by further refining the synthetic protocol, they successfully obtained high-yield $Au_{22}(GSH)_{18}$ nanoclusters.[52]

Thus, optimized synthetic procedures are crucial for achieving size-controlled synthesis of molecular gold nanoclusters, as they profoundly impact their properties and broaden their potential applications.

2.2. Bioimaging in NIR-I vs NIR-II Windows

Imaging plays a profound role in modern medicine to "see" internal structures, visualize structural and biological processes in cells and organisms, monitor treatment outcomes, and scan for early signs of disease in both preclinical and clinical settings. The state-of-the-art imaging modalities including MRI,[53−55] X-rays,[56−58] ultrasound,[59−61] CT,[62−64] and PET[65−67] scans are instrumental in public health and preventative medicine and have aided devising curative and palliative treatment schemes. These techniques offer excellent tissue penetration depths but have limitations in resolution and molecular specificity. For example, MRI (tissue penetration: up to 30 cm, spatial resolution: 1−2 mm, temporal resolution: 1−5 s) and CT scans (tissue penetration: up to 25 cm, spatial resolution: 0.5−1 mm, temporal resolution: 0.2−0.5 s) may not provide the speed required for real-time imaging in clinical settings and typically offer spatial resolution at the submillimeter level. Molecular imaging, which involves imaging cells, tissues, or organisms with molecular specificity, can be challenging with certain techniques. Thus, it is crucial to advance noninvasive imaging techniques that provide both high spatial resolution and real-time feedback, while also enabling deep tissue penetration and molecular specificity.

Fluorescent imaging is an alternative noninvasive and cost-effective technique that relies on the visible-to-near-infrared light interactions with biological tissues to obtain subcellular and molecular information with high resolution.[68,69] Video rate, high

https://doi.org/10.1021/acs.chemrev.4c00835
Chem. Rev. 2025, 125, 5195−5227

temporal resolution (>∼30 frames per second) fluorescence imaging is readily achievable, which is beneficial for real-time imaging applications such as performing imaging-guided surgical interventions.[70] However, the main challenges for in vivo fluorescence imaging are scattering of light and autofluorescence of biomolecules, causing shallow tissue penetration depths and poor spatial resolutions. When a fluorophore in a body is excited by light, different light-tissue interactions will occur causing light scattering, reabsorption and tissue autofluorescence (Figure 1A). Scattering of light in biological tissues includes Raleigh scattering and Mie scattering due to light interactions with small molecules and particularly shaped organisms in the tissue (Figure 1B). Light absorption is mostly attributed to endogenous water and hemoglobin. Hemoglobin absorption is observed mostly in the visible range governed by the porphyrin rings (Figure 1C), while water absorbs little in the visible range of the spectrum and shows an absorption at 1450 nm due to the vibrational overtone (Figure 1D). Considering water absorption through vibrational overtones, tissue scattering, and the detection capabilities of InGaAs cameras within the range of approximately 900 to 2300 nm, the NIR-II window can be divided into distinct biologically transparent subwindows: NIR-IIa (1300−1400 nm), NIR-IIb (1500−1700 nm), NIR-IIc (1700−2000 nm), and NIR-IId (around 2100−2300 nm) windows.[71,72]

The autofluorescence of endogenous molecules (NADPH, flavin, elastin, etc.) is nearly diminished in the long end of NIR wavelengths (Figure 1E). Thus, fluorescence imaging with extended excitation and emission wavelengths in the NIR-II window affords reduced light scattering and autofluorescence in tissues, resulting in deeper penetration depth, reduced feature smearing and hence enhanced spatial resolution and high signal-to-background (SBR) ratios.

Since the first in vivo NIR-II imaging with single-walled carbon nanotube probes, numerous groups have shown that fluorescence imaging within the second near-infrared (1000−3000 nm) window,[70,73,74] also referred to as short-wave infrared (SWIR) region, afford much higher SBR and spatial resolution at greater tissue depths (approximately 5−20 mm) compared to imaging in the visible (400−700 nm) and the traditional first near-infrared (NIR-I, 700−900 nm) windows (around 1−3 mm). In particular, light scattering and nearly zero tissue autofluorescence are afforded for fluorescence detection in the NIR-IIb (1500−1700 nm) under 808 nm excitation.[75−78]

Over the years, many NIR-I and NIR-II fluorescent probes have been developed to carry out bioimaging in cell cultures, small animal models and in humans (only NIR-I), to reach effective tumor targeting for disease treatment, to follow immune responses in vivo and to develop novel and robust vaccines for diseases and viral infections.[79−83] Indocyanine green (ICG) was the first NIR-I fluorescent probe approved by the FDA (U.S. Food and Drug Administration) for clinical use in 1959.[84] It has since been widely used in various medical applications, including diagnostics and imaging of angiography,[85−88] liver function assessment,[89,90] and lymph node mapping.[91−94] Ever since, the list of NIR-I probes has been extended and many other probes have been developed and are currently under Phases 1−3 clinical trials.[95,96] IRDye800CW is another major NIR-I fluorophore (conjugated to various antibodies) that is currently under clinical trials for head and neck,[97−99] breast,[100] brain,[101,102] renal,[103] and colorectal[104] cancers.

NIR-II probes and imaging in the NIR-II window, however, are primarily in preclinical stages using small animal models for various diseases.[70,80−83,105] For example, single-walled carbon nanotubes (SWCNTs),[106−113] quantum dots (QDs),[114−125] down-conversion rare-earth nanoparticles,[78,126−130] small organic dyes,[131−138] polymeric nanoparticles,[139−148] and aggregation-induced emission (AIE) nanoparticles[149−158] have been extensively applied for vasculature imaging,[144,155,159] brain imaging,[125,142,145,158] tumor targeting,[119,120,143,146,147,154,157,158] treatment,[116,119,123,128] and monitoring of immune responses.[78,127,128] Despite the tremendous potential of NIR-II imaging, challenges remain, including the development of biocompatible probes, the standardization of imaging protocols, and the translation of research findings into clinical practice. Addressing these challenges is essential for the widespread adoption of NIR-II imaging in clinical settings.

Recently, molecular gold nanoclusters have emerged as a promising class of NIR-I and NIR-II probes, offering enhanced safety and biocompatibility. These nanoclusters exhibit wide NIR-I to NIR-II emissions, making them novel fluorescent agents for bioimaging with the potential for clinical translation (vide infra) (Table 1).[32,160,161]

2.3. Photoluminescence Mechanism in Common NIR-II Probes

Photoluminescence (PL) mechanisms in NIR-II probes are primarily dictated by intrinsic electronic transitions, which govern their optical properties and emission behavior. Quantum dots, as semiconducting nanostructures, exhibit pronounced quantum confinement effects, leading to discretized electronic states.[162−164] Upon excitation, an electron is promoted from the valence band to the conduction band, generating a Coulombically bound exciton. PL arises from exciton recombination, where radiative decay yields photon emission (Figure 2A). The quantum confinement effect modulates the energy gap between the conduction and valence bands,[162] resulting in size-dependent emission wavelengths that are tunable across the visible-to-NIR-II spectrum. Precise control over QD dimensions enables systematic tuning of emission profiles, making them versatile candidates for bioimaging in the NIR-II window.[163,164]

Similar quantum confinement effects govern the PL mechanisms in single-walled carbon nanotubes, which exhibit sharp electronic density of states maxima, known as van Hove singularities,[165] in their energy band structures.[166] Upon absorption of a photon with energy corresponding to the E_{22} interband transition,[167] an exciton is generated and subsequently undergoes ultrafast nonradiative relaxation to the lowest available energy states in both the conduction and valence bands (Figure 2B). The radiative recombination of this exciton via the E_{11} transition[168] results in strong PL emission, with emission wavelengths dependent on nanotube chirality and diameter. This intrinsic size-dependent electronic structure, combined with excitonic effects, underlies the tunable optical properties of SWCNTs, making them promising candidates for NIR-II bioimaging.[113]

Trivalent rare-earth ions exhibit characteristic 4f−4f electronic transitions, generating a rich spectrum of optical absorption and emission lines due to the shielding of the 4f orbitals by the outer 5s and 5p orbitals. The luminescence of rare-earth nanoparticles arises from the resonance levels upon excitation. In particular, the efficient $^4I_{13/2} \rightarrow {}^4I_{15/2}$ energy transition in Er^{3+} ions results in intense down-conversion emission centered at 1550 nm (Figure 2C).[78,126] Additionally,

https://doi.org/10.1021/acs.chemrev.4c00835
Chem. Rev. 2025, 125, 5195−5227

Table 1. Gold Nanocluster-based NIR-II Probes[a]

NIR-II probe	Ligand	Ex/Em wavelength, nm	NIR-II QY and the detection range	Application	Ref.
AuMHA/TDT[b]	6-Mercaptohexanoic acid and dithiol tetraethylene glycol	680/1200″	-	Vasculature imaging	182,210
		830/∼1050″	6%		
AuNCs[c]	Lipoic acid-based sulfobetaine	785/∼1000	0.6%	Vasculature imaging	184
		785/900	3.8%		
Au_7Cd_1-MHA/MPA	6-Mercaptohexanoic acid and 3-mercaptopropionic acid	808/1000	-	Vasculature imaging	183
$Au_{25}(GSH)_{18}$[b]	Glutathione	808/1120	∼0.13%; 900−1500 nm	Brain imaging, Tumor metastasis imaging	203,211
AuTPPTS/GSH	Triphenylphosphine-3,3′,3″-trisulfonic acid and glutathione	808/1026	-	Kidney imaging	212
AuMHA/Cystm[b]	6-Mercaptohexanoic acid and cysteamine	980/∼1050	1.4%; 1000−1400 nm	Kidney imaging	186
$Au_{24}Cd_1$MPA[b]	3-Mercaptopropionic acid	808/1020	1.1%; 1000−1700 nm	Kidney imaging	189
$Au_{21}Cu_1$GSH	Glutathione	808/925	0.16%	Kidney imaging	44
AuNAC[b]	N-Acetylcysteine	808/∼1050	0.5%	Kidney imaging	213
AuNPs	2,3-Dimethylaleic anhydride modified β-mercaptoethyl-amine and 2-diethylaminoethanethiol hydrochloride	808/1040	-	Kidney imaging	214
Ag_4Au_1NPs	Mercaptosuccinic acid	488/1120	-	Liver imaging	215
Ln@AuNCs[b]	N-Acetylcysteine	808/1100	0.52%	Liver imaging	216
AuNPs[b]	3-Mercaptopropyl trimethoxysilane and PEG-methyl ether thiol	488/1070	1.8%; 900−1400 nm	Liver imaging	217
		488/955	12%		
c-AuNPS[b]	Ethyl-3-mercaptopropanoate and Pluronic F-127	785/1080	1.6%	GI imaging	192
r-AuNPs[b]		785/1280	0.25%		
AuNCs[b]	RNase-A	808/1050	1.9%	GI imaging	218
$Au_{24}Cu_1$ and $Au_{24}Cd_1$	3-Mercaptopropionic acid	808/1050	-	GI imaging	219
AuNCs-DA[b]	GSH and (*poly*)dopamine	808/1050	0.65%; 850−1450 nm	Gastric acid imaging	220
$Au_{25}(GSH)_{18}$[b]	Glutathione	808/1050	0.27%	Bone imaging	221
$Au_{44}MBA_{26}$-P	4-Mercaptobenzoic acid and 3-amino-propane-1-phosphate	808/1080′ and 1280″	∼ 4.5%	Bone imaging and RA treatment	222
AuNCs[b]	Mercapto-β-CD	808/1050	0.11%	Tumor targeting	223
AuNCs-Pt[b]	Glutathione	808/1050	0.04%; 900−1500 nm	Tumor targeting	224
AuNCs[b]	AS1411	488/1030	0.2−0.4%; 900−1400 nm	Tumor targeting	225
AuGSH[c]	Glutathione and 4-aminophenylphosphoryl choline	808/1090	0.27%; 900−1500 nm	Lymph node imaging	45
AuPC[c]			0.38%; 900−1500 nm		
$Au_{25}(SR'')_n(SR')_{18-n}$	SR″: 11-mercaptoundecanoic acid, 11-mercaptoundecylphosphonic acid, 11-mercaptoundecylsulfonic acid (MUS)	808/1050	1.48%	Lymph node imaging and lymphatic metastasis treatment	226
	SR′: C5 thiolated zwitterionic ligand				
AuNCs[b]	BSA	808/1025	1.1%	Lymph node imaging, tumor targeting and PDT	227
AuNCs[b]	Min-23	808/1050	0.21%; 830−1300 nm	Tumor targeting and PDT	228
$Au_{44}MBA_{26}$	4-Mercaptobenzoic acid	808/1080′ and 1280″	∼4.5%	Tumor targeting, PDT/PTT and immunotherapy	47,48
AuNCs[b]	BSA	808/960′ and 1010″	3.5%; 900−1500 nm	Tumor targeting and PDT	229
D/UCNP@AuNCs	Mercapto-β-CD and GSH	808/1060	-	PDT and chemotherapy	230
Gd@AuNCs	BSA	808/∼1010″	∼3%	Tumor targeting and radiotherapy	231
AuPC[c]	Glutathione and 4-aminophenylphosphoryl choline	808/1090	0.38%, 900−1500 nm	Imaging-guided surgery and PTT	201
AuNCs	Mercapto-β-CD	808/1080	-	Chemotherapy	232

https://doi.org/10.1021/acs.chemrev.4c00835
Chem. Rev. 2025, 125, 5195−5227

Table 1. continued

[a]Note, Ex refers to excitation wavelength in QY detection, while Em wavelength relates to the PL peak position at that excitation wavelength. The notations ′ and ″ refer to the first and second emission peaks. [b]QY was determined using external reference. [c]QY was determined using integrating sphere method.

sensitization of Er^{3+} ions can be achieved through codoping with Yb^{3+} ions, which absorb near-infrared light around 980 nm via the $^2F_{7/2} \rightarrow {}^2F_{5/2}$ transition. This energy is transferred to the Er^{3+} ion, enhancing the overall luminescence efficiency and enabling more efficient excitation of the Er^{3+} emission bands. The Yb^{3+}/Er^{3+} codoping strategy significantly improves the brightness of the NIR-II emission, making these rare-earth doped nanoparticles promising candidates for advanced imaging applications.[78,127]

Lastly, small-molecule NIR-II dyes, such as indocyanine green, are typically designed with a donor−acceptor−donor (D−A−D) electronic architecture, where electron-rich donor groups are positioned on either side of a conjugated π-system that serves as an electron acceptor.[169,170] This structural motif facilitates efficient charge transfer and enhances the electronic transitions. The extended π-conjugation lowers the energy gap between HOMO and LUMO, leading to strong absorption and emission in the NIR region.[171] The D−A−D framework promotes intramolecular charge transfer (ICT), which further stabilizes excited-state configurations and enhances the fluorescence efficiency. In molecules with extensively conjugated π-electron systems, electron delocalization across the framework becomes more pronounced with increasing conjugation length, further reducing the HOMO−LUMO gap and redshifting the absorption and emission spectra.[171]

2.4. Photoluminescent Molecular Gold Nanoclusters

The first report on photoluminescence in gold, copper, and alloyed metals dates back to 1969[172] while the interest in fluorescent gold nanoclusters jumped after the synthesis of monodisperse thiolated AuNCs by Brust−Schiffrin in 1994.[4] The size-dependent photoluminescent properties of AuNCs are reflected by their quantized electronic states and determined by the energy band gaps they exhibit. To correlate size-property dependence and elucidate the PL mechanisms in AuNCs, it requires extensive experimental and computational efforts. AuNCs show rich absorption features in their optical spectra corresponding to different electronic transitions including intraband (sp→sp), interband (d→sp), and mixed intraband−interband transitions.[3] The PL mechanism in AuNCs, however, is far more complicated (Figure 3A). The visible-NIR luminescence in AuNCs involves both metal core states (pure gold transitions) and surface states (mixed gold−sulfur transitions, Figure 3B).[173−175] Thus, the fluorescence characteristics of gold clusters are intricately modulated by optimizing the number of gold atoms in the core and choosing appropriate surface ligands.[7,176,177] For more details on the luminescence mechanisms in gold nanoclusters, ranging from visible to NIR-II, the reader is referred to a recent comprehensive review by Jin and colleagues.[174] Unlike other NIR-II materials, the clusters tend to exhibit lower molar absorptivity and quantum yields (QY), which significantly hinder their applications in sensing and imaging. Over the years, various strategies have been proposed to enhance the brightness of AuNCs,[28,31] involving the engineering of ligand shells ("surface-regulated" PL enhancement)[7,31] and the modulation of the metallic frameworks ("core-regulated" PL enhancement).[178,179]

In a "surface-regulated PL" strategy, the surface ligands substantially influence the PL properties of clusters by facilitating the charge transfer to the metallic core via the Au−S bond and directly providing delocalized electrons from electron-rich atoms or functional groups to the metal core.[173,180] Therefore, ligands with robust electron-donating capabilities can

https://doi.org/10.1021/acs.chemrev.4c00835
Chem. Rev. 2025, 125, 5195−5227

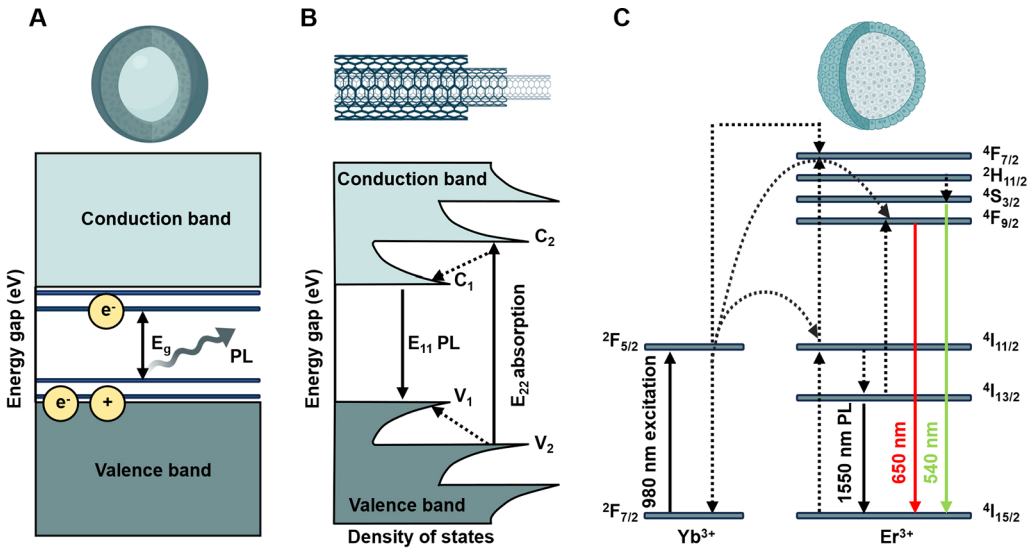

Figure 2. (A) Schematic illustration of the PL mechanism in QDs, depicting exciton generation upon photon absorption followed by carrier relaxation through nonradiative processes and radiative recombination of electron−hole pairs. The emission wavelength is determined by quantum confinement effects, with smaller QDs exhibiting blue-shifted emission and larger QDs emitting at longer wavelengths. (B) Schematic illustration of the PL mechanism in SWCNTs, showing exciton generation upon photon absorption at the E_{22} transition (first excited sub-band), followed by ultrafast nonradiative carrier relaxation to the E_{11} state (lowest energy sub-band). Radiative recombination from the E_{11} state leads to near-infrared emission, with the emission wavelength dictated by the nanotube's chirality and diameter. (C) Schematic illustration of the luminescence mechanism in doped Er^{3+} down-conversion nanoparticles under 980 nm excitation, highlighting Yb^{3+} sensitization and energy transfer to Er^{3+}, leading to characteristic 1550 nm emission. Nanoparticles structures were created with BioRender.com.

be considered as a pivotal strategy for enhancing the fluorescence intensity of gold clusters through ligand−metal charge transfer (LMCT), metal−ligand charge transfer (MLCT), or ligand−metal−metal charge transfer (LMMCT) mechanisms (Figure 3B).[180,181] Also, the rigidification of the ligand is sought to restrict the vibrational and rotational, i.e., thermal, motions of the ligands, thus promoting the radiative relaxation of excited electrons. This can be achieved by introducing the second ligand either directly attaching to the gold during synthesis[180,182] or through ligand exchange reactions[181,183] and conjugating/electrostatically attaching to the primary ligand.[46,181,184,185] For example, the ligand exchange of mercaptohexanoic acid (MHA) protected Au_{25} cluster with cysteamine (Cystm), 2-mercaptoethanol (ME), or DL-dithiothreitol (DTT) afforded a 10-fold enhancement in the NIR-II quantum yield.[186] Bis-Schiff base linkages between $Au_{22}(GSH)_{18}$ nanoclusters and 2,6-pyridinedicarboxaldehyde effectively restrict intramolecular motion of surface motifs at the single-cluster level, enhancing the luminescence quantum yield up to 48% in water-soluble gold nanoclusters within the NIR-I window.[187]

Since the electronic transitions in the core are dominant in emission processes, in a "core-regulated PL" strategy, the luminescent properties of AuNCs can be drastically improved and even shift from the visible to NIR region by simply modifying the number and the type of metals inside the core of the clusters. In general, with increasing the size of the clusters, the bang gap decreases and therefore, the emission peak undergoes a bathochromic shift.[176,188] Small clusters, typically comprising fewer than 20 gold atoms, exhibit emissions within the visible-to-NIR-I regions, while gradual increase in the gold atoms within the core results in a systematic red shift of the emission peaks toward NIR-II window.[174,176] The heteroatom doping of the metallic framework and substitution of at least one gold atom in the core or at the surface is also considered an alternative way of modulating the PL properties due to the electronic synergy between metals (Figure 3C).[44,183,189] For example, the doping of silver atoms inside the Au_{25} cluster core led electronic perturbation to the HOMO and LUMO orbitals by subsequently increasing the energy bandgap (thus blue shifting the PL from 827 to 680 nm) causing 200-fold PL enhancement (QY 40.1%).[190] A single substitution of the gold atom in the staple motif with a Cd atom in 3-mercaptopropionic acid (MPA)-protected Au_{25} cluster caused decrease of HOMO−LUMO gap and facilitated the radiative relaxation and hence resulted in ∼56-fold enhancement in NIR-II intensity (QY 1.1%).[189] In accordance with the PL enhancement by metal doping, the biological properties get affected as well.[183] For example, Cu-doping of GSH-protected Au_{22} cluster afforded 18-fold higher antioxidant, 90-fold higher catalase-like, and 3-fold higher superoxide dismutase-like activities.[44]

Encapsulating the clusters inside polymer nanoparticles[191,192] or introducing "lock rings" and "lock atoms"[193,194] in the cluster structure are alternative methods for improving the emission and increasing the PL quantum yield of clusters. The Xie group developed advanced synthetic ligand shell engineering strategies to enhance the NIR-II photoluminescence properties of gold nanoclusters.[195−198] By employing covalent and electrostatic interactions, AuNCs were effectively incorporated into diverse matrices, including polymers[196,197] and biomolecules[195,198] forming next-generation hydrophilic cluster-based nanoassemblies. This integration not only stabilized the nanoclusters in biological environments but also modulated their electronic and optical properties, leading to enhanced emission efficiency and improved biocompatibility for high contrast bioimaging of lung orthotopic tumors.[197]

Recently, the Jin group demonstrated that the absorption of gold nanoclusters can be tuned from the NIR-I to the NIR-IIb and IIc subwindows by modulating the aspect ratio in a series of rod-shaped gold clusters (Figure 3D).[199,200] The unidirectional

https://doi.org/10.1021/acs.chemrev.4c00835
Chem. Rev. 2025, 125, 5195−5227

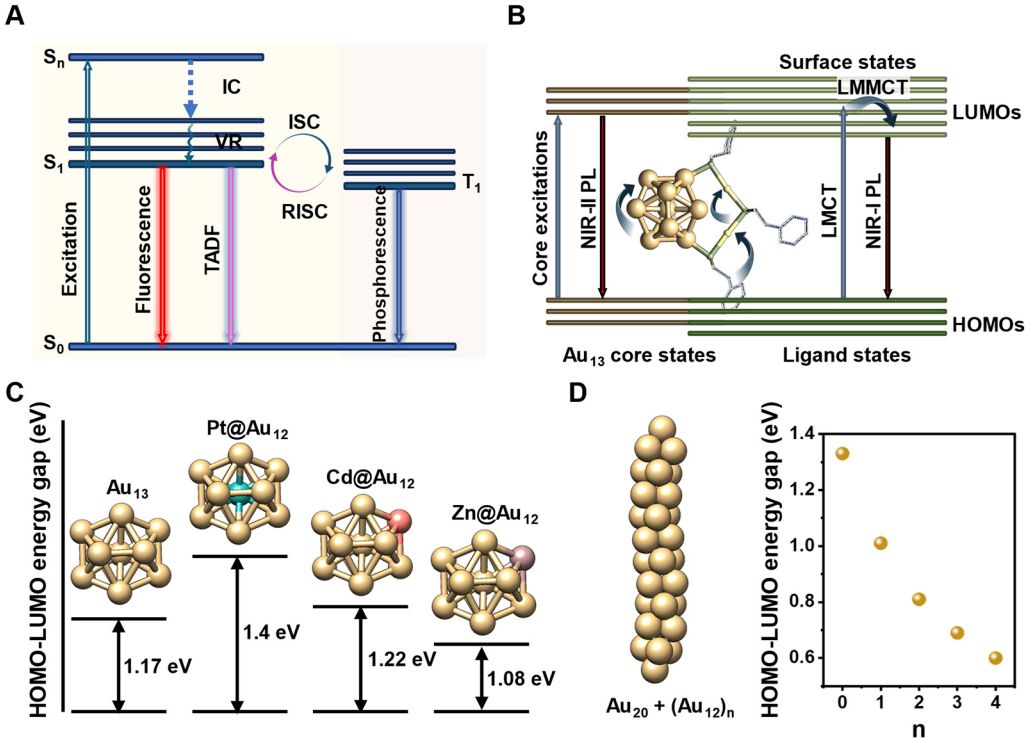

Figure 3. (A) Emission mechanisms of atomically precise metal nanoclusters upon excitation at a specific wavelength. IC: internal conversion, VR: vibrational relaxation, ISC: intersystem crossing, RISC: reverse intersystem crossing, and TADF: thermally activated delayed fluorescence. (B) The contribution of Au_{13} core state excitations to NIR-II emission, alongside LMCT and LMMCT charge transfers within the staple motifs to NIR-I emission in Au_{25} nanoclusters. (C) Heteroatom doping of the Au_{13} icosahedral core in Au_{25} nanoclusters as a strategy for tuning the HOMO−LUMO energy gap. For the sake of clarity, the staple motifs are omitted. The metal doping sites in Au_{25} nanoclusters are preferentially located at the center of the core for Group IX (Rh, Ir) and Group X (Ni, Pd, Pt) metals, while Group XI (Ag, Cu) and Group XII (Zn, Cd, Hg) metals predominantly occupy the core surface sites. The energy gap values were obtained from refs.[202,203] (D) Modification of the energy gap in metal nanocluster-based anisotropic rods across the series $Au_{42}(PET)_{32}$, $Au_{60}(PET)_{44}$, $Au_{78}(PET)_{56}$, $Au_{96}(PET)_{68}$, and $Au_{114}(PET)_{80}$. For clarity, the staple motifs have been omitted, and only the core of the cluster is represented as $Au_{20} + (Au_{12})_n$, where n denotes the number of repeating units. The energy gap values were obtained from ref 199. PET refers to the ligand 2-phenylethanethiol. The Au_{13} and Au_{32} core structures were prepared using UCSF Chimera program (version 1.16) based on crystal structures data published in refs 204 and 199, respectively.

elongation of these anisotropic clusters, achieved through the successive addition of $(Au_{12})_n$ repeating units to the Au_{42} cluster (which contains an Au_{20} core), resulted in a decreased HOMO−LUMO energy gap (Figure 3D) and a red-shift in absorption, extending deep into the NIR-II window up to 1800 nm. However, the PL properties in a series of rod-shaped clusters have not been reported yet.

Note that recently, we have demonstrated that Au_{25} clusters fluoresce across a broad range of excitations, exhibiting excitation-independent behavior without any change in the PL peak position (NIR-II PL max at 1090 nm).[201] In fact, in the photoluminescence excitation/emission (PLE) spectra, the clusters displayed an intense PL peak in the range of 900−1450 nm (recorded with an InGaAs detector) upon excitation in the 550−840 nm window. Visible to NIR-I fluorescence of clusters (recorded with a silicon-based PMT detector) exhibited a strong peak around 750 nm when excited in the 600−900 nm range.[201] Thus, we found that the Au clusters were emissive in a wide range of 600−1450 nm when excited at shorter wavelengths and could be imaged in the visible and NIR-I and NIR-II.

In vitro, as well as in vivo, the intrinsic properties of many fluorescent nanoparticles, including quantum dots and small noble metal clusters, are expected to change upon internalization or interaction with cellular components.[205−209] In particular, the intracellular stability of nanoparticles is strongly influenced by their size and surface coating, as well as the exposure of active sites upon interaction with biogenic thiols such as glutathione and cysteine.[206,209] Such intracellular events have been widely reported for relatively large nanoparticles and have been correlated with dynamic changes in the protonation/deprotonation of surface functional groups, particularly within the acidic lysosomal compartments following endocytic uptake. The fluorescence lifetime shortening of semiconducting QDs emitting in the red region was directly attributed to surface modifications and ligand displacement within the cytoplasm, as demonstrated by fluorescence lifetime imaging microscopy (FLIM).[208,209] In contrast to QDs, small gold nanoclusters exhibited remarkable stability in vitro, with no significant changes in their fluorescence lifetimes over 24 h of incubation. This stability is attributed to the strong Au−S bond formations on the cluster surface and effective shielding from protein corona formation or in vitro biothiol-induced etching processes.[209] We have recently demonstrated that our NIR-II emissive gold nanoclusters, protected with glutathione (AuGSH) and phosphorylcholine (AuPC, PC refers to phosphorylcholine) ligands, exhibited minimal interaction with serum proteins when incubated with fetal bovine serum (FBS). The formation of protein corona complexes accounted for only 2.7% and 1.74% for AuGSH and AuPC, respectively.[45] Additionally, strong NIR-II fluorescence signals were observed in the bladder and collected urine samples, further highlighting the in vivo integrity

https://doi.org/10.1021/acs.chemrev.4c00835
Chem. Rev. 2025, 125, 5195−5227

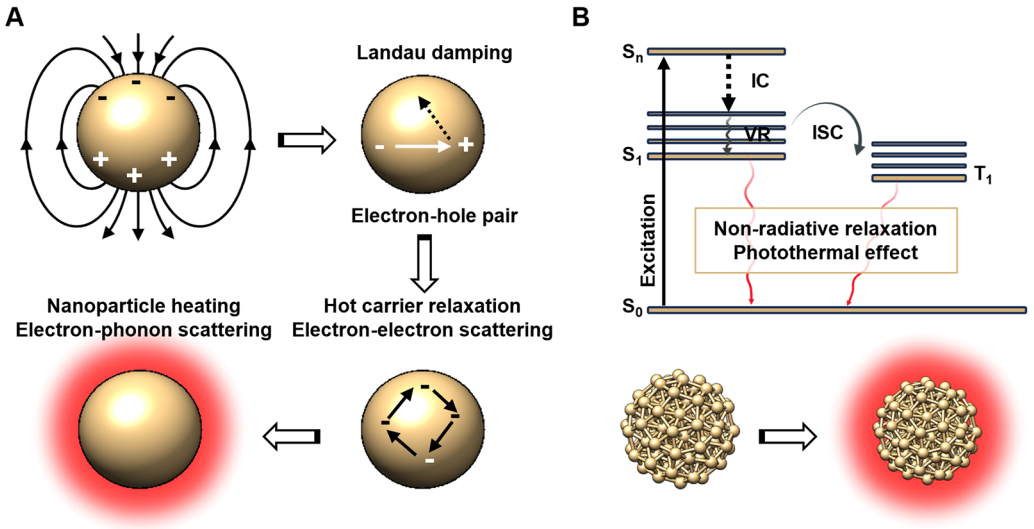

Figure 4. Schematic illustration of the photothermal mechanism in gold nanoparticles (AuNPs) and gold nanoclusters. (A) In plasmonic AuNPs, incident light excites collective oscillations of free electrons (surface plasmon resonance, SPR), followed by nonradiative Landau damping, electron−electron scattering, and electron−phonon coupling, leading to heat generation and thermal dissipation. (B) In AuNCs, photon absorption induces discrete electronic excitations, followed by IC and ISC, resulting in electron−phonon interactions that transfer energy to the lattice, leading to localized heating. The photothermal conversion efficiency in AuNCs is influenced by quantum confinement effects, electronic state density and ligand-induced surface modifications.

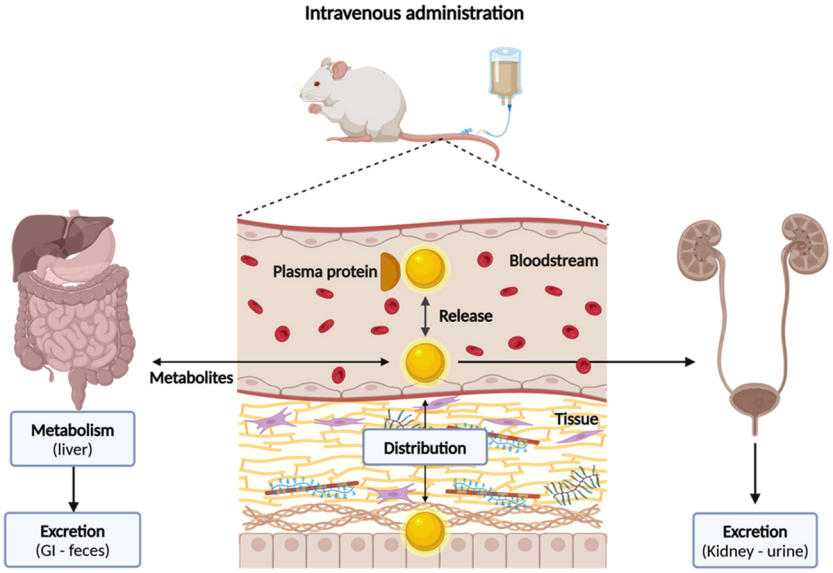

Figure 5. Schematic representation of the main pharmacokinetic processes, including absorption, distribution, metabolism, and excretion. Absorption refers to the entry of a substance into systemic circulation, while distribution describes its transport across tissues and organs. Metabolism involves biochemical modifications, primarily in the liver, affecting the bioavailability and activity. Excretion eliminates the substance via renal or hepatic pathways. Created with BioRender.com.

and stability of our developed probes with no substantial changes in fluorescence properties, at least in terms of intensity. However, investigating potential changes in the fluorescence lifetimes of NIR-II emissive clusters requires the development of an FLIM microscopy imaging platform compatible with the NIR-II window, which has yet to be established.

2.5. Photothermal Effects in Molecular Gold Nanoclusters

Unlike gold nanoparticles (AuNPs), which exhibit strong surface plasmon resonance (SPR) and efficient light-to-heat conversion, gold nanoclusters lack collective plasmonic oscillations due to their ultrasmall size, leading to distinct photothermal mechanisms. The photothermal (PT) mechanism in nanoparticles is governed by a sequential energy conversion process following light absorption.[233,234] Upon excitation, collective electron oscillations generate a strong electromagnetic field, leading to the formation of hot electron−hole pairs (Figure 4A). Through rapid nonradiative decay via Landau damping, the excited carriers transfer energy to the individual electrons. The energetic electrons then undergo electron−electron scattering, redistributing energy and forming a hot Fermi−Dirac distribution.[233] Subsequently, through electron−phonon coupling, the hot electrons transfer energy to the metal lattice, increasing its temperature. Finally, the accumulated heat dissipates into the surrounding environment via phonon−

https://doi.org/10.1021/acs.chemrev.4c00835
Chem. Rev. 2025, 125, 5195−5227

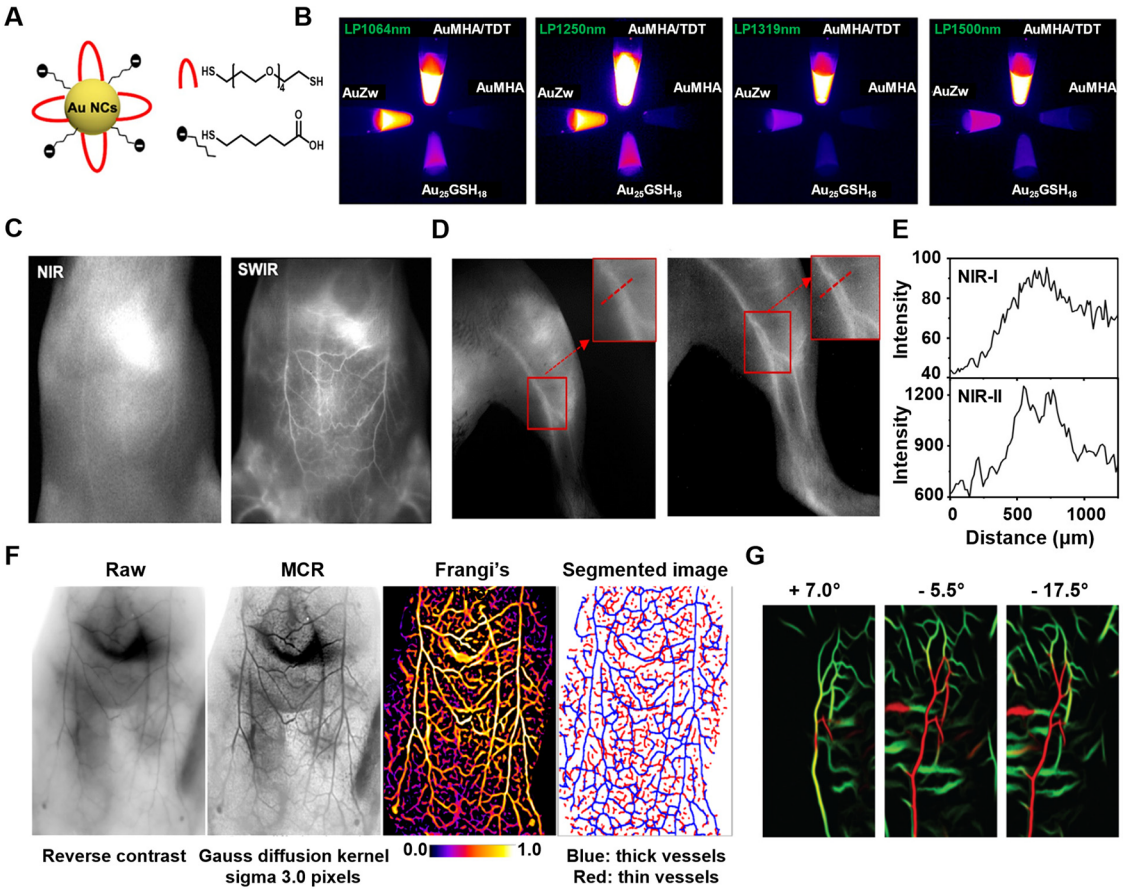

Figure 6. (A) Schematic representation of AuMHA/TDT biligand protected gold nanoclusters. MHA and TDT ligands are presented in black and red colors. (B) NIR-II images of AuMHA, AuMHA/TDT, $Au_{25}GSH_{18}$, and AuZw (300 μM in water) clusters under 830 nm excitation using 1064 nm (1 ms), 1250 nm (5 ms), 1319 nm (25 ms), and 1500 nm (250 ms) long pass filters. (C) NIR-I (excited at 780 nm and emission collected >830 nm) and NIR-II (excited at 830 nm and emission collected >1250 nm) imaging of blood vasculature in WT 129/Ola mice after intravenous injection of AuMHA/TDT clusters (200 μL, 360 μM).[210] Reproduced with permission from ref 210. Copyright 2020, American Chemical Society. (D) NIR-I (left) and NIR-II (right) images of blood vessels in the left leg of a wild type C57BL/6 mouse. The insets are zoomed-in regions highlighted within the red squares. (E) The cross-sectional intensity profiles of blood vessels in the leg in NIR-I (top image) and NIR-II (bottom image) windows.[184] Reproduced with permission from ref 184. Copyright 2017, American Chemical Society. (F) NIR-II images of a *Bmp9*-KO mouse vasculature post-i.v. injection of AuMHA/TDT probe. The raw vasculature image underwent Monte Carlo constrained restoration (MCR), a process designed to enhance the spatial resolution by reducing tissue scattering. Following the MCR process, Frangi's filtering and segmentation analyses were applied, enabling detailed mapping of the blood network based on vessel thickness.[210] Reproduced with permission from ref 210. Copyright 2020, American Chemical Society. (G) 3D SWIR imaging of blood vessel network at different angles.[182] Reproduced from ref 182 with permission from the Royal Society of Chemistry.

phonon interactions, completing the photothermal conversion process.[233]

In gold nanoclusters, the heat generation primarily arises from intrinsic electronic transitions and nonradiative relaxation mechanisms.[200] Instead of plasmonic Landau damping, the energy dissipates through internal conversion (IC) and intersystem crossing (ISC) pathways (Figure 4B).[235] IC process involves the rapid relaxation of excited electrons to lower energy states within the same electronic manifold (usually singlet states) via electron−electron scattering. In the ISC process, some excited electrons transition from singlet states to triplet states. The hot electrons created from the excited states are not in equilibrium with the lattice. Energy is transferred from the electrons to the lattice (phonons) through electron−phonon coupling. This process involves the interaction between the high-energy hot electrons and the vibrations of the atomic lattice. The electron−phonon coupling efficiency (which is relatively less efficient compared to nanoparticles) depends on several factors such as the size of the nanoclusters, ligand effects, and the cluster's electronic structure.[236−238] The energy transfer to the lattice causes an increase in the lattice temperature. Once the lattice is heated by electron−phonon interactions, the phonons propagate through the cluster and interact with one another through phonon−phonon scattering. This allows the energy to spread throughout the nanocluster. The dissipated heat is transferred to the surrounding environment, thereby cooling the nanocluster. This process is responsible for the thermal relaxation[238] of the system and plays a crucial role in photothermal applications in cancer therapy.

3. BIOMEDICAL APPLICATIONS OF AUNCS IN NIR-II IMAGING

3.1. Pharmacokinetics and Biodistribution of Clusters

Due to their nanoscale dimensions (<2 nm in diameter), the nanoclusters exhibit rapid pharmacokinetics (PK): these molecular probes could be absorbed more efficiently than larger molecules, facilitating rapid entry into the bloodstream and

https://doi.org/10.1021/acs.chemrev.4c00835
Chem. Rev. 2025, 125, 5195−5227

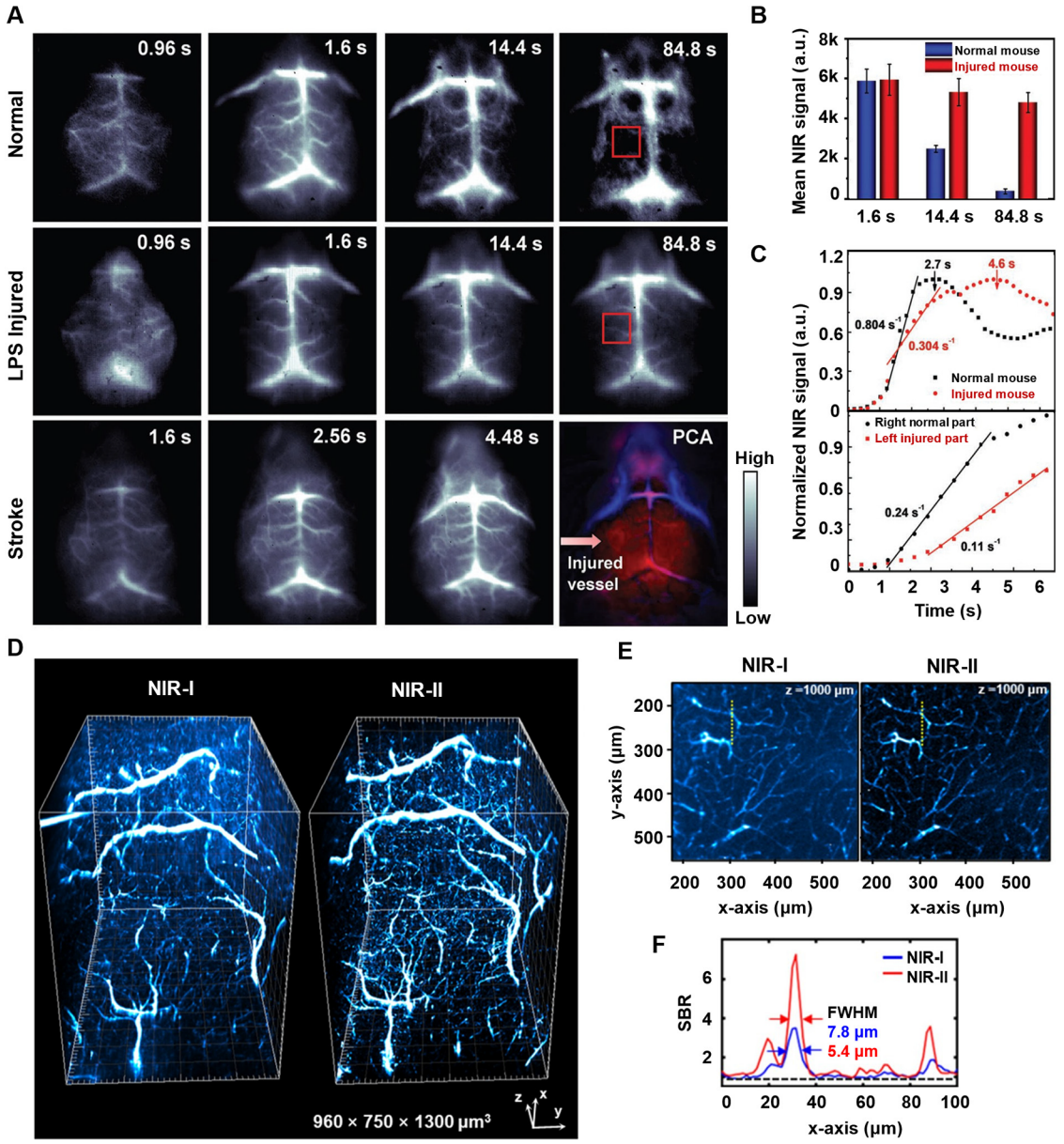

Figure 7. (A) Dynamic NIR-II brain imaging of healthy mice, LPS injured and stroke mouse models under an excitation of 808 nm at 140 mW/cm^2 with an exposure time of 300 ms. No significant NIR-II signal is found after 84.8 s in the healthy mouse, indicating rapid clearance from the brain, while the LPS injured mouse shows longer NIR-II signal retention in the blood vessel. In the case of the stroke mouse model, blocking and reopening of brain vessels cause vascular injury and neovascularization in the left brain, evidenced by more small vessels lightening up in the NIR-II window. Principal component analysis (PCA) overlay images of arterial (red) and venous (blue) vessels in a stroke mouse model indicated a more pronounced injury signal in the left hemisphere. (B) Time-dependent quantitative brain signals (highlighted within the red square) for a normal healthy mouse and an LPS-injured mouse. (C) Blood perfusion of normal healthy mouse/LPS injured mouse (top image) and stroke mouse model (bottom image).[203] Reproduced with permission from ref 203. Copyright 2019, WILEY-VCH Verlag GmbH & Co. KGaA, Weinheim. (D) Comparison of Airy LSM imaging of the three-dimensional structure of mouse cerebral vessels in the NIR-I and NIR-II regions. (E) $x-y$ cross-sectional images of blood vessel under different excitation wavelengths. (F) Intensity profiles along the line shown in panel F.[211] Reproduced with permission from ref 211. Copyright 2022, Elsevier Ltd.

subsequent distribution throughout the body (Figure 5). The distribution of nanoclusters is influenced by their physicochemical properties, including size[215,217] and surface charge.[186,212] The clusters typically have very short blood circulation half times of ≤30 min.[186,189,228] However, coating the cluster surface with a secondary ligand,[226] encapsulating inside the micelles/polymer networks[192] or doping on the surface of large nanoparticles,[216,230] can enhance their circulation time. Excretion of nanoclusters typically follows renal and occasionally hepatobiliary routes (when in vivo aggregation occurs due to protein-corona formation in vivo[215,217]). Since the clusters are usually smaller than 5−6 nm, they are generally cleared by the kidneys and excreted in the urine. For example, systemically administered AuGSH clusters exhibit rapid whole-body distribution <3 min postinjection, attributed to their swift intravasation from blood vessels and subsequent dissemination into major organs.[45,203] Within 30 min postinjection, the clusters underwent renal clearance with strong NIR-II signals appearing in the bladder and were excreted via urine, accounting for approximately 80% of the Au content in the collected urine

https://doi.org/10.1021/acs.chemrev.4c00835
Chem. Rev. 2025, 125, 5195−5227

samples post 24 h.[45,203] The biodistribution of gold in major organs was found to be negligible, thus indicating no toxicity at the cellular (in vitro cell viability test) and tissue levels (pathological examination). However, obvious skeletal signals were detected for AuGSH clusters (vide infra), potentially accounting for the remaining ∼20% of injected gold due to the probable affinity of GSH for the hydroxyapatite in the bone matrix.[45,221] The surface modification of AuGSH clusters with phosphorylcholine ligands imparted stealth properties, allowing for nearly 100% clearance of injected AuPC probe.[45] Thus, the pharmacokinetic profile of nanoclusters underscores their rapid absorption and distribution within the body. Their efficient entry into the bloodstream and dissemination across major organs highlight their potential as molecular probes in advancing biomedical imaging and therapeutic strategies, supported by their favorable pharmacokinetic behavior and minimal organ-level toxicity.

3.2. Vasculature Imaging

Noninvasive fluorescence imaging of vascular networks largely is important to assessing vascular disorders with minimum interventions and risks involved. Real-time monitoring of the vessel structure with intravenously (i.v.) administered NIR-II emissive probes affords higher resolution down to micrometer scale than other nonoptical modalities.

In 2019, Liu et al. employed water-soluble $Au_{15}(GSH)_{18}$ (QY 0.13%, Table 1) nanoclusters, emitting in the >1000 nm range, for through-skull brain imaging with a specific focus on high-contrast cerebral blood vessel visualization.[203] These nanoclusters enabled precise detection of vascular networks in vivo, particularly in models of lipopolysaccharide (LPS)-induced brain injury and stroke, offering enhanced resolution of the blood vessel architecture (vide infra).

Le Guevel group prepared a series of AuNCs with very high quantum yields in water for NIR-II imaging of vasculature and related disorders.[182,184,210,239] For instance, the surface rigidification of gold clusters by rigid dithiol ligand (LA-sulfobetaine: lipoic acid-based sulfobetaine, QY 3.8%, Table 1)[184] or introducing anisotropic biligand coating (MHA/TDT ligands; TDT: tetra(ethylene glycol) dithiol, QY 6%, Table 1)[182,210] drastically improved the quantum yield of clusters ∼1 order of magnitude (compared to previously reported AuNCs) in water (Figure 6A). Single metal doping in Au_8 clusters with biligand coating (MHA/MPA, MPA: mercaptopropionic acid) also afforded bright NIR-II clusters for vascular imaging.[183] Overall, the postsynthetic surface/core modifications of the clusters and fine-tuning the reaction parameters allowed to extend the imaging window up to 1500 nm without compromising the NIR-II brightness of the prepared clusters (Figure 6B).[210] In vivo, clear and deeper visualization of blood vasculature network in mice was achieved in the NIR-II (emission collected at >1250 nm) window while NIR-I imaging (780 nm excitation and >830 nm emission, Silicon camera) suffered from low spatial resolution and high background for the same probe administration (Figure 6C,D).[210] The blood vessels were successfully imaged at 1.5, 5, 25, and 65 s within a 15 min imaging window following probe administration.[210] Consequently, sharper and more detailed cross-sectional profiles can be obtained with NIR-II imaging (Figure 6E).[184] Monte Carlo and deep learning processing of images further improved the image quality by reducing the tissue scattering (Figure 6F).[182,210] It also became possible to reconstruct the 3D image of blood vessels at different angles and depths (Figure 6G).[182]

3.3. NIR-II Imaging of Small Animal Organs

3.3.1. Brain Imaging. Noninvasive neurological imaging using CT, PET, MRI techniques provides clinical diagnosis on physiological activity and cognitive function of the brain (healthy vs perturbed brain).[240,241] Although these techniques are remarkably advantageous for the clinical assessment of brain function, they lack the necessary cellular resolution for imaging and detecting changes in cellular structures before macroscopically or microscopically visible changes in cell morphology occur. In contrast, preclinical optical imaging and especially fluorescence imaging in the NIR-II window can afford high spatiotemporal imaging of brain structure and vasculature through intact skull of mice.[241−245] Noninvasive NIR-II emissive carbon nanotubes,[112] quantum dots,[125,243,244] down-conversion rare-earth nanoparticles,[78,246] and organic fluorophores[247,248] have provided a detailed structural and vascular imaging of brain and cerebrovascular diseases[249,250] in murine models at imaging depths of a few mm without craniotomy.

In 2019, Liu et al. performed the first through-scalp and through-skull cerebrovascular imaging in NIR-II window using intravenously injecting Au_{25} clusters (QY 0.13%, Table 1) in normal, LPS induced brain injury or ischemic stroke models (Figure 7A).[203] The cluster allowed for the visualization of inferior cerebral vein, superior sagittal sinus, transverse sinus, arterial, and venous vessels with high resolution in normal mice and disease models (LPS and stroke), revealing clear differences in NIR-II signals in the vessels at different time-points post i.v. injection (Figure 7B), corresponding to different diffusion and perfusion rates among different study groups (Figure 7C). Strong fluorescent signals associated with active neovascularization caused by the stroke can be distinguished in the left hemisphere of the brain (ischemic stroke), while completely absent in the right hemisphere (healthy brain side). For deeper imaging of brain tissue, the same group employed airy beam assisted NIR-II light sheet microscope.[211] Ex vivo imaging of a mouse brain (Figure 7D) after 5 min post-iv administration of the cluster (while the probe is still in circulation) in both NIR-I and NIR-II windows allowed for the visualization of the brain vessels of the cerebral cortex at imaging depths of 1.3 mm. Clearly, the imaging in NIR-II window afforded reduced background (Figure 7E) and ∼3-fold increase in SBR (Figure 7F), thus providing higher spatiotemporal resolution and the premise for deep tissue NIR-II microscopy.

3.3.2. Noninvasive Kidney Imaging. The kidney is a metabolic organ that functions as an organism's filtering system to remove xenobiotics and metabolic waste from the blood. Renal-clearable small chemotherapeutic drugs most often cause kidney injuries through renal function impairment. Clinical diagnosis of kidney function relies on noninvasive imaging modalities (SPECT,[251,252] PET,[251,253] MRI,[254] ultrasonography[255]) that suffer from high cost, radiation exposure and contrast agent nephrotoxicity. Although renal biopsy is informative, it is invasive and holds a risk of damaging other organs.[256] Blood and serum analyses of renal filtration markers (blood urea nitrogen: BUN, creatinine: CREA) are routine procedures for kidney functions assessment.[257] Unfortunately, these biomarkers are not sensitive to early stage kidney malfunction. Real-time optical imaging of kidney dysfunction is an alternative noninvasive imaging modality. The imaging of kidney and its dysfunction in murine models have been realized with a few NIR-I agents including silica dots,[258] small gold nanoclusters,[160,259] organic dye ZW800-CDPL[260] and NIR-II

https://doi.org/10.1021/acs.chemrev.4c00835
Chem. Rev. 2025, 125, 5195−5227

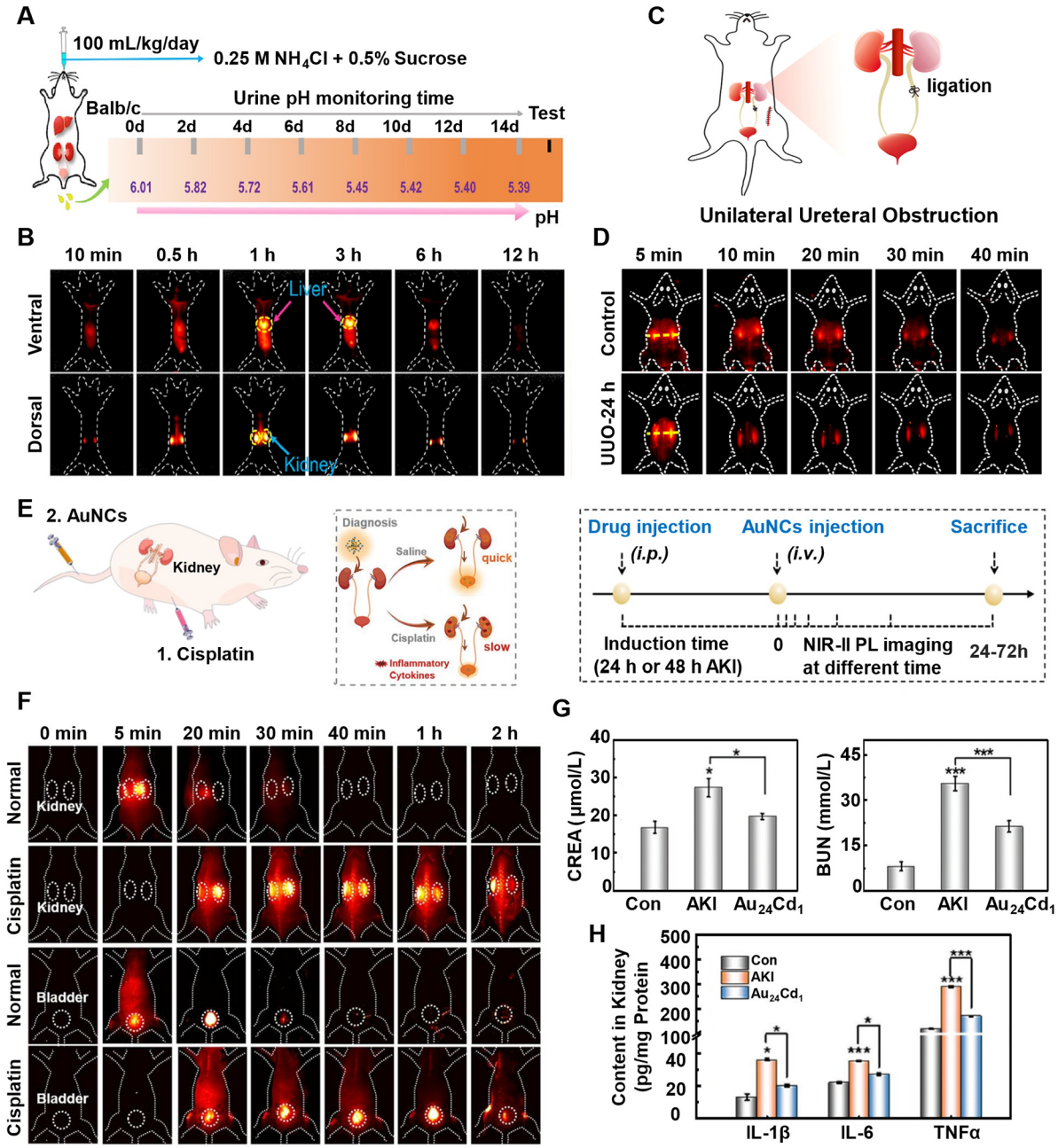

Figure 8. (A) Schematic representation of the NH_4Cl-induced metabolic acidosis mice model. (B) In vivo NIR-II fluorescence imaging of injured mice at different time points post-i.v. injection of TPPTS-AuNCs. The etching and exchange with liver sinusoidal GSH ligand activated bright NIR-II signal in the kidney and bladder with inhibited renal clearance rates in injured mice model.[212] Reproduced with permission from ref 212. Copyright 2023, American Chemical Society. (C) Schematic representation of the unilateral ureteral obstruction (UUO) model development in mice. (D) NIR-II fluorescence imaging of UUO mice with ureteral ligation for 0 min and 24 h at different time points post-i.v. injection of MHA/Cystm-AuNCs.[186] Reproduced with permission from ref 186. Copyright 2023, American Chemical Society. (E) Schematic representation of the cisplatin-induced AKI mice model development and the experimental timeline for intraperitoneal (i.p.) drug-intravenous cluster administration.[189,213] Reproduced with permission from refs 189, 213. Copyright 2023, Wiley-VCH GmbH and Copyright 2023, American Chemical Society. (F) Real-time in vivo NIR-II imaging of intravenously administered $Au_{21}Cu_1$ cluster signal in the kidney and bladder in the control and AKI groups under an 808 nm laser and 1000 nm long-pass filter. The renal clearance is fast (<30 min) in the normal heathy mice, while in AKI model the kidney drainage is increased up to 2 h post-i.v. injection causing longer attenuation of NIR-II signal in the kidney and slower excretion into bladder.[44] Reproduced with permission from ref 44. Copyright 2023, The American Association for the Advancement of Science. (G) CREA and BUN serum biomarkers and their expression levels 3 days post-AKI after treatment with $Au_{24}Cd_1$ (n = 3 per group), respectively. Control group: saline; AKI group: cisplatin (20 mg/kg); $Au_{24}Cd_1$ group: cisplatin+ $Au_{24}Cd_1$. (H) IL-1β, IL-6, and TNFα expression levels in kidney tissues 3-days post-AKI with or without clusters treatment (n = 3 per group).[189] Reproduced with permission from ref 189. Copyright 2023, Wiley-VCH GmbH.

probes such as organic macromolecules,[261,262] dyes,[263,264] lanthanide complexes,[265,266] and semiconductor probes.[267]

In particular, several NIR-II emissive gold nanoclusters have recently been reported for real-time preclinical in vivo imaging of kidney and assessment of its function in healthy and disease

https://doi.org/10.1021/acs.chemrev.4c00835
Chem. Rev. 2025, 125, 5195−5227

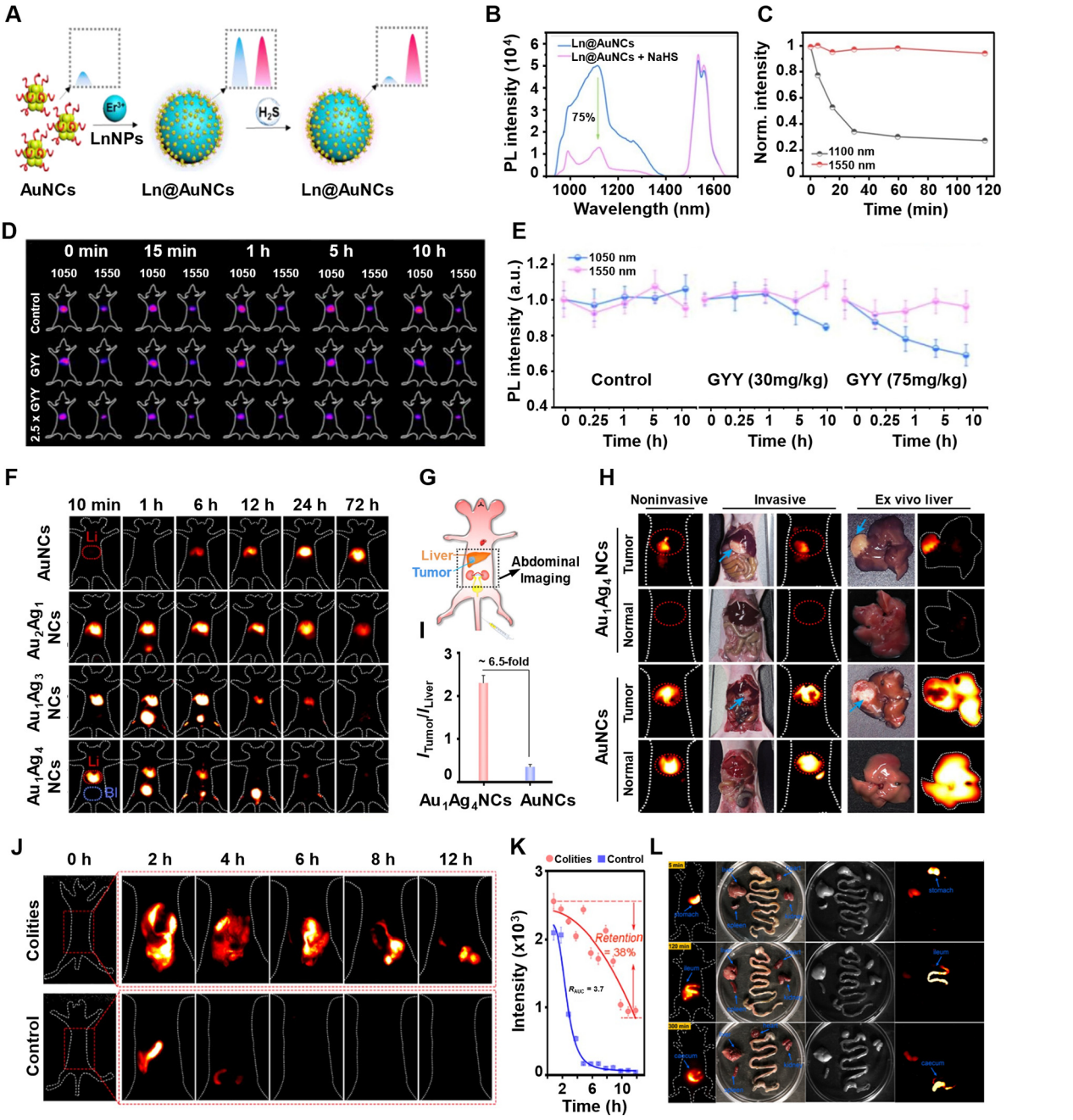

Figure 9. (A) Schematic representation of Ln@AuNCs synthesis and their NIR-II PL changes upon H_2S treatment. (B) In vitro H_2S detection based on the PL changes of Ln@AuNCs nanoprobe after NaHS treatment (80 μM). (C) Time-dependent PL intensity changes at 1100 and 1550 nm emission wavelengths. (D) NIR-II imaging of mice and (E) PL intensity changes at various treatments, including PBS (control group), low (30 mg/kg) and high dosage (75 mg/kg) of GYY4137 prodrug.[216] Reproduced with permission from ref 216. Copyright 2022, American Chemical Society. (F) NIR-II imaging of mice at various time points after the injection of AuNCs and Ag-doped clusters. The red and blue circles indicate regions of the liver and bladder, respectively. (G) Schematic representation of NIR-II imaging of mice bearing a liver tumor. (H) Noninvasive, invasive (open abdominal cavity), and ex vivo fluorescence imaging of liver post-12 h injection. The circles and arrows indicate the regions corresponding to the liver and tumor, respectively. (I) Ex vivo tumor-to liver (I_{Tumor}/I_{Liver}) fluorescence intensity ratios post-12 h of treatment with different nanoclusters.[215] Reproduced with permission from ref 215. Copyright 2022, American Chemical Society. (J) Time-dependent fluorescence imaging of the gastrointestinal tract after intragastrical (IG) administration of AuNC@polymer formulations and (K) the corresponding fluorescence intensity retention profiles.[192] Reproduced with permission from ref 192. Copyright 2022, American Chemical Society. (L) NIR-II imaging of gastrointestinal peristalsis by orally administered RNase-A@AuNCs (2 mg/kg dosage, 1000 nm LP, 200 ms, 808 nm excitation, 15 mW/cm^2).[218] Reproduced with permission from ref 218. Copyright 2020, Wiley-VCH GmbH.

model.[44,186,189,212] The structure modification of the native clusters by ligand shell engineering (mixed ligand clusters, QY 1.4%, Table 1)[186,212] or by doping the metallic framework with heteroatoms (doped clusters, QY 0.16−1.1%, Table 1)[44,189] has shown drastic enhancement in NIR-II brightness for in vivo kidney imaging. For instance, the in vivo ligand exchange of triphenylphosphine-3,3′,3″-trisulfonic acid (TPPTS)-AuNCs with liver sinusoid glutathione, imparted activable NIR-II

https://doi.org/10.1021/acs.chemrev.4c00835
Chem. Rev. 2025, 125, 5195−5227

properties in vivo and enhanced interactions with acidic renal tubular epithelial cells for noninvasive monitoring of acidosis induced early kidney injury (Figure 8A,B).[212] Furthermore, the therapeutic efficacy of antiacidosis drugs across diverse dosages and disease stages was effectively monitored in vivo utilizing AuNCs cocoated with a pH-responsive ligand.[214] Ex vivo ligand exchange of MHA-protected Au_{25} cluster with Cystm, ME, or DTT imparted a biligand engineered outer shell that was applied for the imaging of renal ischemia-reperfusion (RIR) and unilateral ureteral obstruction (UUO) in murine models (Figure 8C,D).[186]

Acute kidney injury (AKI) caused by cisplatin chemotherapeutic drug administration at nephrotoxic dosages is largely anticipated in cancer patients worldwide and is one of the major hallmarks of chemotherapy. Real-time NIR-II imaging of kidney and assessment of AKI noninvasively has been achieved with native (QY 0.5%, Table 1)[213] and doped AuNCs (QY 0.16−1.1%, Table 1)[44,189] (Figure 8E). In vivo NIR-II imaging of kidney and bladder signal post cluster administration can visualize the renal function differences in healthy and AKI models (Figure 8F). Significant delays in renal clearance[44,189,213] were typical symptoms for kidney dysfunction with elevated CREA and BUN levels in blood and serum (Figure 8G) accompanied by up-regulation of inflammatory cytokines and chemokines (Figure 8H).[189] The antioxidant and therapeutic activities of clusters, however, downregulated the expression of these markers to their normal serological and pathological levels, thus restoring renal function and decelerating the inflammatory responses.

3.3.3. Liver and Gastrointestinal Tract Imaging. NIR-II emissive CNTs, QDs, and rare-earth nanoparticles tend to nonspecifically accumulate in the reticuloendothelial system (RES, mostly due to their large sizes) and can be utilized for studying liver and spleen functions in vivo. However, fast pharmacokinetics and renal clearance of NIR-II emissive gold nanoclusters, mostly governed by their small sizes, hamper their ability to target and image other organs. A viable option to prolong the pharmacokinetics and increase the blood circulation of gold nanoclusters would be the doping of nanoclusters onto the surface of larger nanoparticles or forming nanocluster-nanoparticle assemblies.

In 2022, Li et al., through ligand-mediated anchoring, N-acetylcysteine (NAC)-protected AuNCs were assembled on a lanthanide NPs (LaNPs) surface (Figure 9A) leading to the formation of a nanocomposite with dual fluorescence in NIR-II window: 1100 nm associated with AuNCs (QY 0.52%, Table 1) and 1550 nm originated from LaNPs (Figure 9B).[216] Such structural modification not only caused 2.5-fold enhancement of 1100 nm PL due to restriction of intramolecular motions in AuNCs, but also improved the pharmacokinetics and completely changed the clearance from renal to biliary. In vitro, the sensitivity and selectivity of the emission at 1100 nm toward H_2S (Figure 9B and C) (due to the reduction of Au(I) in the staple motifs surrounding the cluster core by H_2S while the PL at 1550 nm remained unchanged) made the nanocomposite an ideal ratiometric probe for NIR-II detection of H_2S release from GYY4137 prodrug in the liver. Compared to the control group, the gradual decrease of the liver signal (Figure 9D) postprodrug administration (low dose and high dose, Figure 9E) indicated the successful accumulation of the prodrug and the release of H_2S in the liver and consequent quenching of the cluster emission. Such structural assembly not only allowed prolonging cluster circulation but also imparted diagnostic properties for in vivo drug efficacy monitoring. Alternatively, the cluster sizes and in vivo biodistributions can be modulated by incorporating them into micellar organizations. For instance, high concentrations of polymers (higher than critical micelle concentration: CMC) lead to the entrapment of clusters inside the hydrophobic cores of the micelles through hydrophobic interparticle interactions (QY 1.6%, Table 1).[192] At concentrations lower than the CMC, the clusters interact with polymeric unimers through intraparticle hydrophobic interactions. Either way, such structural modifications led to the formulation of biliary excretable AuNC based NIR-II probes for liver and gut imaging (QY 0.25%, Table 1).[192]

The liver accumulation of nanoparticles due to their larger sizes or in vivo instability (protein−corona formation) could lead to long-term retention and toxicity, hindering possible clinical translation. The capture of nanoparticles from the bloodstream and subsequent phagocytose in liver sinusoids through the mononuclear-phagocyte system (MPS) affects the circulatory retention of the particles, traps them in the liver without hepatic internalization, and hence shortens tumor targeting abilities. Tan et al. showed that silver metal-doping in NIR-II emissive gold clusters (that can form protein−corona complexes) alters the in vivo behavior of clusters by undergoing rapid biotransformation in liver sinusoids.[215] The oxidation of silver on the cluster surface by oxygen and subsequent etching with sinusoidal GSH led to cluster passivation (inhibiting protein-corona formation) and prompted the release back to the bloodstream (Figure 9F). As evidenced by in vivo NIR-II imaging, the renal clearance is directly proportional to the number of doped silver atoms in the cluster composition (Figure 9F). By controlling doping, the clusters can eventually be applied for liver tumor imaging (Figure 9G) without fluorescence interference from healthy liver tissue (Figure 9H,I).

Zhou et al. demonstrated that large gold nano assemblies (NIR-II emissive, QY 1.8%, Table 1) with silane and thiolated PEG ligand coatings could undergo a disassembly process at weak acidic media due to hydrolytic degradation of cross-linked Si−O−Si and transformed/disassembled into smaller nanoclusters (QY 12%, Table 1). Such a transformation not only changed the in vivo behavior from biliary excretion to renal clearance with negligible probe retentions in RES organs but also resulted in the emission blue shift and a 6-fold enhancement of obtained clusters (disassembly induced emission enhancement).[217]

Small gold nanoparticles and especially clusters, once transported to the liver, undergo active secretion from hepatocytes into biliary canaliculus, and drain into the intestines and initiate fecal excretion.[268] The biliary excretion pathway of clusters is beneficial for imaging the gastrointestinal (GI) tract and related disorders. For instance, Tang et al. utilized large AuNC@micelle and AuNC/unimer particles for injured intestinal mucosa in colitis imaging (Figure 9J).[192] Compared to healthy mice, the NIR-II signals in the injured mice decayed gradually with an intensity retention of 38% (Figure 9K) and remained longer in the inflammatory colon. Encapsulating metal-doped clusters inside liposomes covered with neutrophile and red blood cell membranes (for in vivo cloaking) afforded highly efficient ROS-scavenging NIR-II probe for inflammatory targeting, imaging and simultaneous therapeutic treatment of colitis.[219] Ribonuclease-A protected AuNCs (RNase-A@AuNCs, QY 1.9%, Table 1) were successfully applied for the GI tract imaging and monitoring of the probe passage in the digestive system (Figure 9L).[218] Pathological changes, impedi-

https://doi.org/10.1021/acs.chemrev.4c00835
Chem. Rev. 2025, 125, 5195−5227

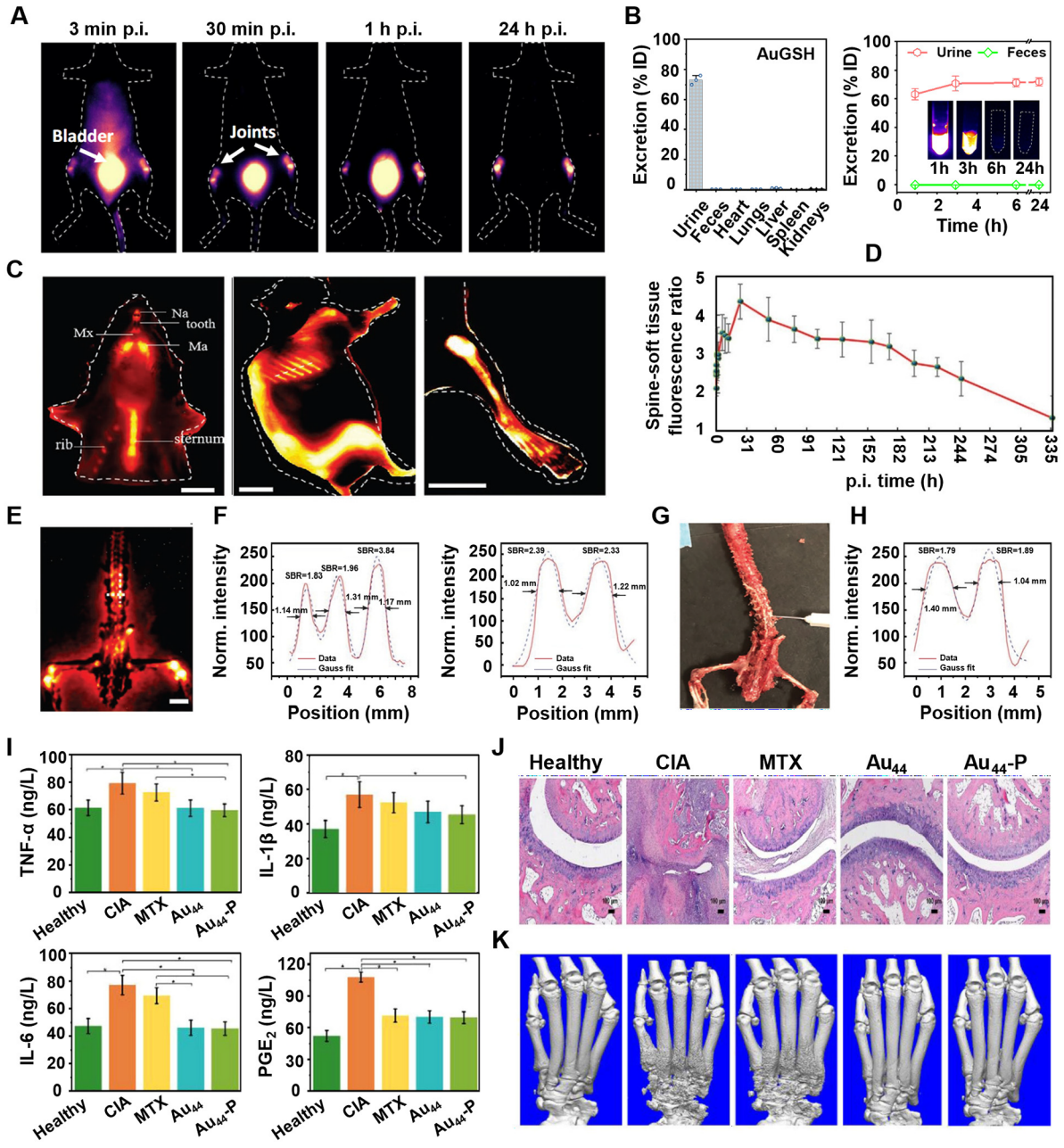

Figure 10. (A) In vivo wide-field NIR-II fluorescence imaging with i.v. injected AuGSH clusters (4×, ∼1.2 mg) excited by an 808 nm laser at a power density of 70 mW/cm^2, exposure times 40 ms, 1100 nm long pass filter at different time points (6 to 7 weeks old female Balb/c, n = 3). (B) Biodistribution in major organs at 24 h (left) and rapid renal excretion profiles (right) after iv administration of the AuGSH probe. The insets represent NIR-II fluorescence images of collected urine samples at different time points.[45] Reproduced with permission from ref 45. Copyright 2022, Springer Nature. (C) NIR-II imaging of skeletal system postiv injection of AuGSH clusters (40 μg/g weight, 200 μL). Fluorescence images of the upper body (left picture, nasal bone: NA, maxilla: Mx, mandible: Ma), ribs (middle picture), and hindlimb (right picture) 8.3 h p.i. of clusters (808 nm laser, 140 mW/cm^2 power density, 1000 nm long-pass filter, exposure time 3000 ms). (D) Time-dependent changes of SBR defined as the ratio of maximal fluorescence intensity on the spine (S) and the surrounding soft tissue (BR). (E) Ex vivo fluorescence imaging of spinal pedicles after the removal of the paravertebral muscles. (F) Analysis of the fwhm and SBRs for vertebrae pedicles: vertical (left) and horizontal (right) cross-sectional intensity profiles. (G) Scoliosis simulation on the bent spine and (H) horizontal cross-sectional profiles for pedicle and spinal canal differentiation under NIR-II imaging.[221] Reproduced with permission from ref 221. Copyright 2020, Wiley-VCH GmbH. (I) Serum levels of pro-inflammatory cytokines TNF-α, IL-1β, IL-6, and PGE$_2$ in collagen immunization-induced rheumatoid arthritis (CIA) rats over 6 weeks of treatment with saline, methotrexate (MTX), Au$_{44}$, and Au$_{44}$−P clusters and nonimmunized normal rats (healthy). (J) Histopathological images of joint sections from healthy and CIA rats. (K) Microcomputed tomography (micro-CT) images of metatarsal bone and ankle articulations in CIA rats.[222] Reproduced with permission from ref 222. Copyright 2023, John Wiley and Sons.

ment of peristaltic movements of clusters, and hence disrupted NIR-II signal distributions along the colon endorsed the noninvasive localization of the intestinal tumor and high accuracy. AuNCs encapsulated with (poly)dopamine (QY 0.65%, Table 1) and loaded with methylene blue as a quencher demonstrated pH-responsive gastric acid imaging in feeding, fasting, acid secretion-inhibited drug, and ulcer models.[220] In vivo recovery of cluster fluorescence, facilitated by the

https://doi.org/10.1021/acs.chemrev.4c00835
Chem. Rev. 2025, 125, 5195−5227

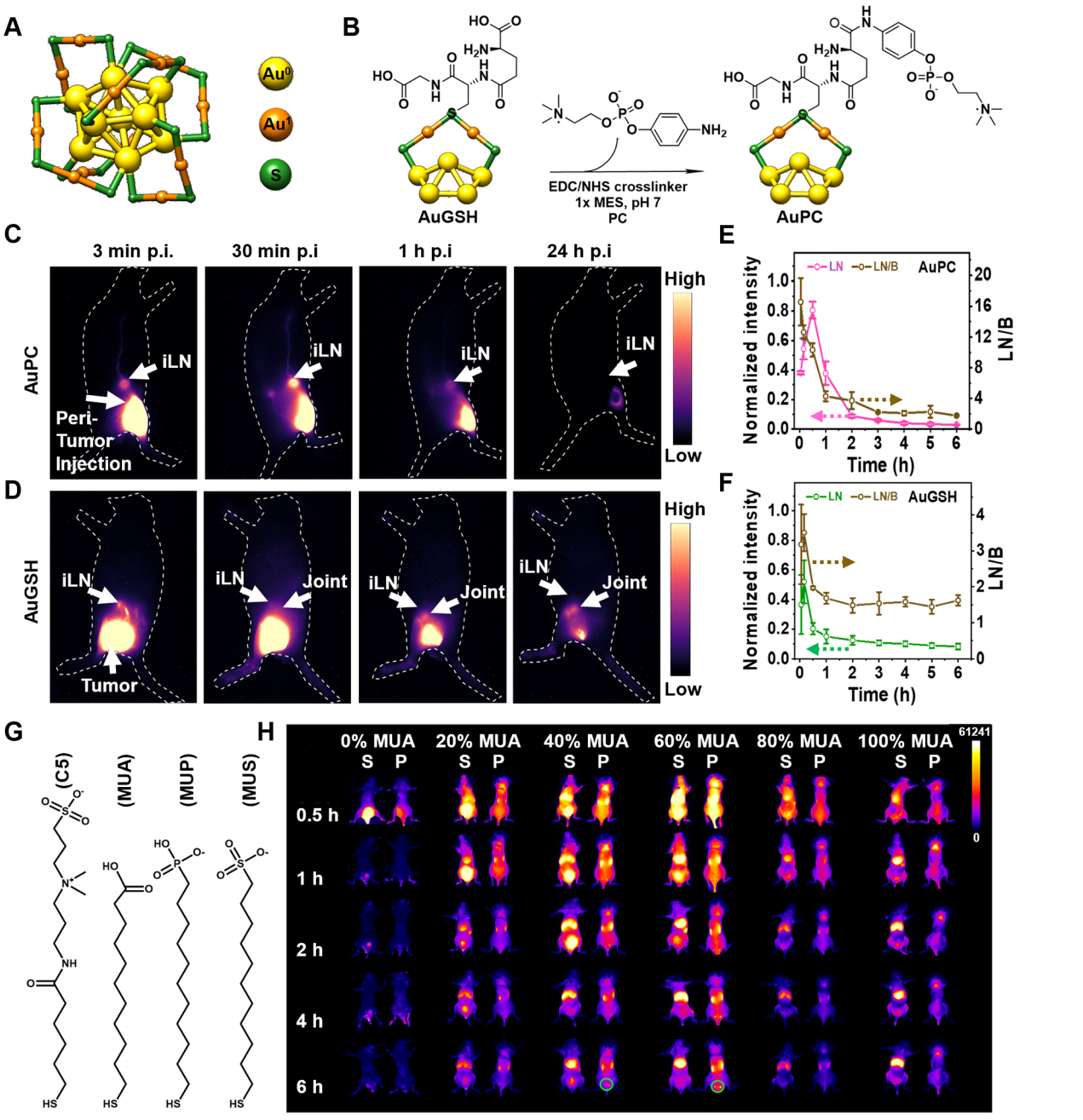

Figure 11. (A) Crystallographic structure of the Au_{25} cluster. Color codes of the elements: Au (0) in the core: yellow, Au (I) in the staple motif: orange, S in the staple motif: green. (B) Postfunctionalization of AuGSH cluster with phosphorylcholine ligand (PC ligand) resulted in the formation of AuPC conjugate. For clarity, only one staple motif and adjacent gold core atoms are shown. For simplicity, the conjugation of PC ligand to glycine carboxylic group is omitted and it is only shown with γ-glutamate carboxylic functional group of GSH. Wide-field NIR-II fluorescence images (excited by an 808 nm laser at a power density of 70 mW/cm^2, exposure times 20 and 40 ms for AuPC and AuGSH, respectively, 1100 nm long pass filter) of (peri) intratumoral (i.t.) injected (C) AuPC conjugate (1×, ~300 μg) and (D) AuGSH cluster (1×, ~300 μg) probes into a 4T1 tumor bearing mouse at different time points. Normalized fluorescence intensities (left Y axes) and lymph node signal-to-background (LN/B) ratios (right Y axes) postinjection of (E) AuPC conjugate and (F) AuGSH cluster.[45] Reproduced with permission from ref 45. Copyright 2022, Springer Nature. (G) The chemical structures of the thiolated C5 and anionic ligands used for the preparation of $Au_{25}(SR')_n(SR'')_{18-n}$ clusters. C5: thiolated zwitterionic ligand, MUA: 11-mercaptoundecanoic ligand, MUP: 11-mercaptoundecylphosphonic ligand, and MUS: 11-mercaptoundecylsulfonic ligand. (H) In vivo distribution of dual-ligand-capped AuNCs with different proportions of anionic ligands after i.v. injection of AuNCs (5 mg kg^{-1}) for 6 h (S, supine position; P, prone position). 40−60% MUA feeding ratio in AuNCs afforded effective accumulation in the LNs located in the sciatic area (labeled with green ovals, 30 ms, 20 mW/cm^2).[226] Reproduced with permission from ref 226. Copyright 2022, American Chemical Society.

protonation of polydopamine and release of methylene blue, enabled NIR-II imaging of the stomach without the need for dissection.

Thus, by utilization of various strategies for cluster size manipulation, the imaging and diagnostic properties of clusters for various organs can be tuned in a controlled manner in preclinical mouse models.

3.3.4. Skeletal System Imaging. Bone scintigraphy is vastly employed for the evaluation of bone pathologies during growth and remodeling, bone metastasis, and diseases.[269] Planar

https://doi.org/10.1021/acs.chemrev.4c00835
Chem. Rev. 2025, 125, 5195−5227

imaging largely relies on the intravenous administration of 99m-Tc diphosphonates radiopharmaceuticals as bone targeting agents specifically binding to the hydroxyapatite (HA) crystals in the bone matrix.[269] As an imaging modality and diagnostic tool in clinical practice and nuclear medicine, bone scintigraphy has been instrumental; however, it does raise many concerns regarding radioisotope administration for certain groups of patients. Thus, developing safer and cheaper imaging agents with high specificity toward the skeletal system remains a challenge.

Recently, NIR-II fluorescence imaging of bones with polymeric nanoparticles,[270] down-conversion rare-earth nanoparticles[271] and carbon nanotubes[111] allowed for noninvasive and long-term monitoring of bone pathology and diseases. It has been shown that glutathione protected Au_{25} clusters[45,221] (AuGSH, QY 0.27%, Table 1) and phosphorylated Au_{44} clusters[222] (Au_{44}−P, QY ∼ 4.5%, Table 1) have strong affinities in accumulating and nonspecifically (in case of AuGSH) or specifically (in case of Au_{44}−P) binding to the skeletal system in murine models regardless of administration route.[45,221] The strong binding of clusters to bones was mostly attributed to the strong affinity of the GSH and phosphate ligands toward HA of the bone matrix based on in vitro experiments.[221,222] Although these clusters are easily renal clearable (Figure 10A), a substantiable amount (∼25%) does remain in the body strongly bound to the skeletal system (Figure 10B).[45] The mandible, cervical vertebrae, ribs, sternum, femur, lumbar, knee, and pelvis of the skeletal system can be visualized in the NIR-II window (Figure 10C) with high resolution and extraordinary imaging quality without interference of internal organs (due to fast renal clearance) under intact skin (skin removal is usually performed for in vivo imaging with other bone affinity fluorophores).[221] All the bony structures in animals can be visualized within minutes postinjection of the AuGSH cluster (Figure 10C), thus drastically shortening the wait times usually acquired for other imaging modalities. High spine to normal soft tissue (SBR) ratios of >4 can be achieved 24 h postinjection of AuGSH clusters with a gradual decrease in intensity over the course of weeks (Figure 10D). Ex vivo imaging of spinal pedicles (Figure 10E) and SBR analyses on vertical and cross-sectional profiles (Figure 10F) allowed us to distinguish different pedicles and differentiate them from spinal canal, respectively. More importantly, the SBR differences between pedicles and spinal canal could be a way of simulating scoliosis under NIR-II imaging without the risk of nerve damaging during spine pedicle screw implantation (Figure 10G,H). Lastly, NIR-II imaging of bones can be developed into a diagnostic tool for imaging, evaluation of progression, or treatment efficacy in various bone diseases, e.g., rheumatoid arthritis. The specific targeting and accumulation of Au_{44}−P clusters in bones and joints (post 24 h of injection) facilitated in vivo NIR-II imaging and diagnosis, as well as the simultaneous monitoring of therapeutic efficacy in rheumatoid arthritis rats following cluster administration.[222] Additionally, these clusters demonstrated efficacy in down-regulating pro-inflammatory cytokines TNF-α, IL-1β, IL-6, and PGE_2 production (Figure 10I) and reversing bone erosion and joint deformities (Figure 10J,K).

3.4. Preclinical Cancer Imaging and Treatment

3.4.1. Sentinel Lymph Node Imaging. Tumor metastasis remains a hallmark in current oncology and accounts for more than 90% of deaths in cancer patients worldwide.[272] While surgical resections of primary tumors and immunochemotherapies afterward vastly improve patient outcomes, the metastatic spread of intravasated primary cells through circulatory system and colonization at a distant organ remains unpredictable and imminent.[273,274] Targeted molecular therapies against tumor progression and metastasis play a crucial role in preventing cancer recurrence and improving patient outcomes undergoing invasive surgical interventions and chemotherapeutic treatments.[275,276] Cancer metastasis through lymphatic spread is usually initiated in the first draining node, known as the sentinel lymph node (SLN). SLN biopsy (SLNB)[277] therefore is widely accepted oncological procedure for tumor metastasis evaluation and cancer staging that involves the peritumoral administration of technetium-99m radioisotope (lymphoscintigraphy),[278,279] indocyanine green (NIR-I dye)[93,94] and visual dye methylene blue (MB).[280] However, the established SLN detection methods sometimes show high mis-detection rates and suffer from harmful radiation exposure (in case of lymphoscintigraphy) and side effects (in case of organic dyes).

Recently, as an alternative to clinically approved ICG dye, NIR-II emissive gold clusters with specifically engineered ligand shells have been developed as effective LN-targeting agents in vivo.[45,226,227] Lymph node draining performances of NIR-II AuNCs were reported to drastically improve when modifying the surface coating of $Au_{25}(SR)_{18}$ clusters by postsynthetically coupling to another ligand[45] or introducing secondary thiolated ligand during synthesis.[226] For instance, covalently attaching phosphorylcholine ligand (PC ligand) to $Au_{25}(GSH)_{18}$ clusters (abbreviated as AuGSH, QY 0.27%, Table 1) via EDC chemistry (AuPC clusters, QY 0.38%, Table 1, Figure 11A,B), the intratumorally injected NIR-II emissive AuPC clusters showed drastically improved LN draining properties in preclinical breast (4T1 tumor) and colon (CT26 tumor) cancer models.[45] The surface coating with biocompatible hydrophilic PC ligand extended the SLN detection window up to ∼2 h (Figure 11C) compared to the parent AuGSH cluster (detection window ∼10 min, Figure 11D) or ICG (detection window exhibited variability across different groups, introducing uncertainty in the imaging results) thus allowing sufficient time from probe administration to LN detection with ∼2-fold higher lymph node-to-background (LN/B) ratios (Figure 11E, F). Besides, the AuPC clusters exhibited significantly reduced trapping and retention at both the injection site and throughout the body relative to ICG and AuGSH clusters. This behavior underscores their pronounced stealth characteristics, attributed to the surface phosphocholine ligands, which effectively minimized non-specific interactions with proteins, cells, and tissues. The reduced biofouling conferred by these ligands enhances the biocompatibility and circulation kinetics of the AuPC clusters, thereby mitigating the undesired accumulation in tissues or organs.

LN draining properties of gold nanoclusters are directly influenced by the surface charge state of the clusters. For example, in mixed ligand $Au_{25}(SR'')_n(SR')_{18-n}$ clusters (where SR″s are either MUA: 11-mercaptoundecanoic ligand, MUP: 11-mercaptoundecylphosphonic ligand or MUS: 11-mercaptoundecylsulfonic ligand, while SR′ is C5: thiolated zwitterionic ligand) LN draining properties strongly influenced by the feed ratio of the second SR″ ligand and the charge state of overall cluster (QY 1.48%, Table 1, Figure 11G).[226] For example, at full coverage of the zwitterionic SR′ ligand, the surface charge density is effectively neutralized, leading to superior antifouling properties and significantly reducing protein corona formation. As the proportion of anionic SR″ ligands increases, the net

https://doi.org/10.1021/acs.chemrev.4c00835
Chem. Rev. 2025, 125, 5195−5227

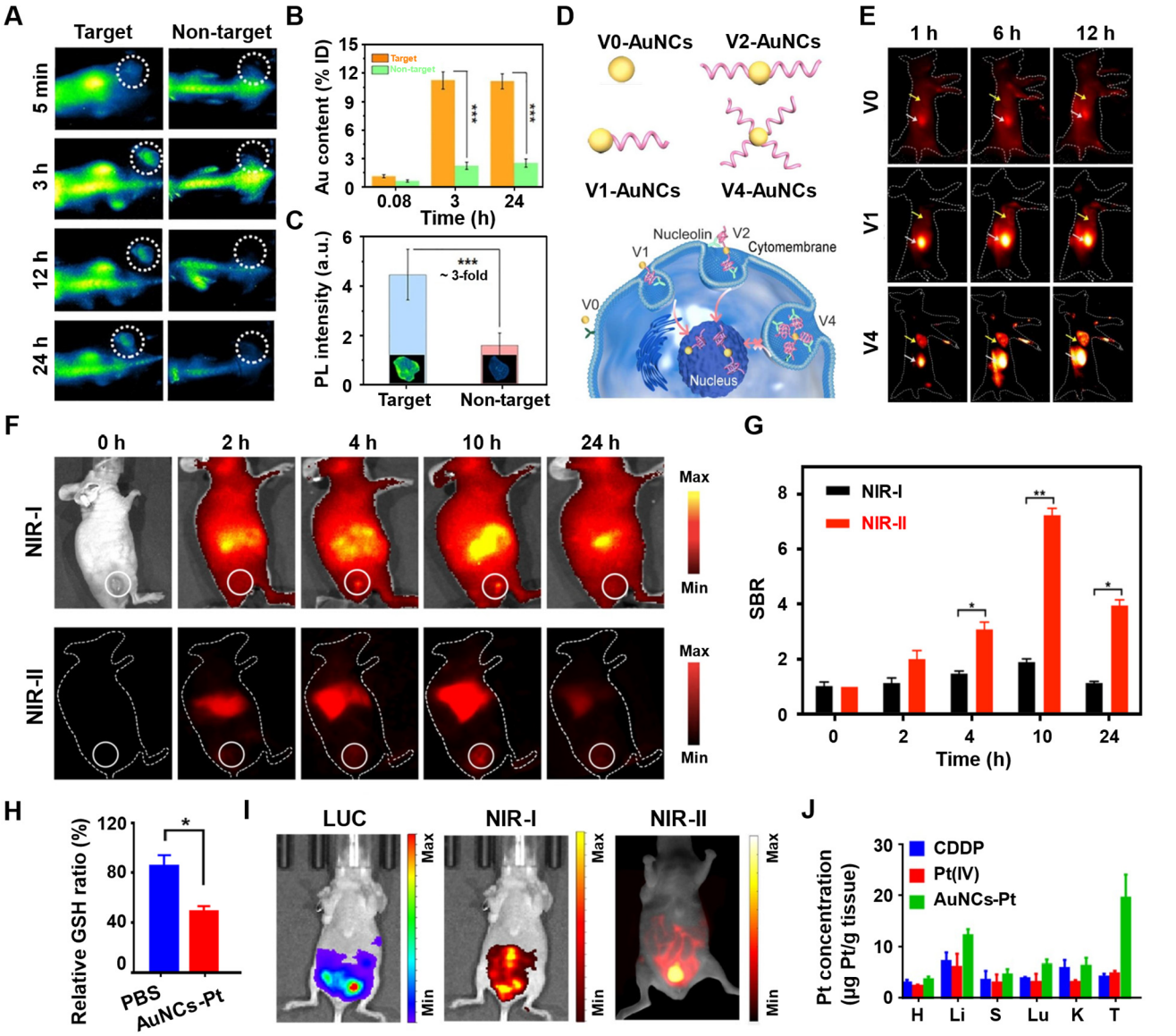

Figure 12. (A) NIR-II imaging of mice at various time points post-i.v. injection of CD-AuNCs (nontarget) and Ab@AuNCs (target). The circles indicate the tumor sites. (B) Time-dependent tumor accumulation of clusters after injection. (C) Ex vivo NIR-II images and PL intensity comparison of excised tumors post-24 h of injection. All NIR-II images were acquired by InGaAs camera upon 808 nm laser excitation (0.2 W/cm^2).[223] Reproduced with permission from ref 223. Copyright 2020, Wiley-VCH GmbH. (D) Schematic representation of AuNC@AS1411 with discrete DNA valences (top) and valence-dependent subcellular transport (bottom) in the tumor. (E) NIR-II images (lateral position) of 4T1 tumor-bearing mice at various time points postiv injection of probes. The yellow and gray arrows indicate the tumor location and kidney, respectively.[225] Reproduced with permission from ref 225. Copyright 2023, Wiley-VCH GmbH. (F) NIR-I and NIR-II images of 4T1 tumor-bearing mice at various time points post-i.v. injection of BSA@Au. (G) Comparison of SBR between in vivo NIR-I and NIR-II images of the 4T1 tumor. NIR-I imaging was performed using an excitation wavelength of 675 nm and an emission wavelength of 800 nm. For NIR-II imaging, the conditions included an excitation wavelength of 808 nm, a long-pass filter set at 1000 nm, and an exposure time of 800 ms.[229] Reproduced with permission from ref 229. Copyright 2022, MDPI. (H) Intracellular GSH level in 7404 cells treated with AuNCs-Pt conjugates. (I) In vivo LUC, NIR-I and NIR-II imaging at 12 h post-ip administration of AuNCs-Pt (Pt: 3.5 mg/kg). (J) Pt biodistribution in the heart (H), liver (Li), spleen (S), lung (Lu), kidney (K), and tumor (T) post-12 h injection.[224] Reproduced with permission from ref 224. Copyright 2020, American Chemical Society.

surface charge of the cluster shifts toward more negative values, thereby enhancing protein corona formation and prolonging systemic retention time in vivo. A 40−60% feed ratio of anionic ligands provided higher LN signals in vivo. A further increase of the second ligand introduced more negative charges and induced instability in vivo, causing protein−corona complex formation (Figure 11H). Consequently, the nanocluster biodistribution profiles switched from renal clearance to biliary excretion without draining to LNs. Moreover, ex vivo NIR-II imaging of the LN histological slices located the clusters (with 50% MUA feed) near the afferent lymphatics, in subcapsular sinus and follicular area thus making them excellent theragnostic agent for LN imaging and LN-invaded tumor metastasis treatment.

Proteins have long been exploited as capping ligands for the synthesis of NIR-I AuNCs. In early 2021, Tang et al. reported the first NIR-II gold clusters protected with bovine serum albumin (BSA, QY 1.1%, Table 1), a major circulatory protein.[227] Intradermally administered BSA-capped AuNCs

https://doi.org/10.1021/acs.chemrev.4c00835
Chem. Rev. 2025, 125, 5195−5227

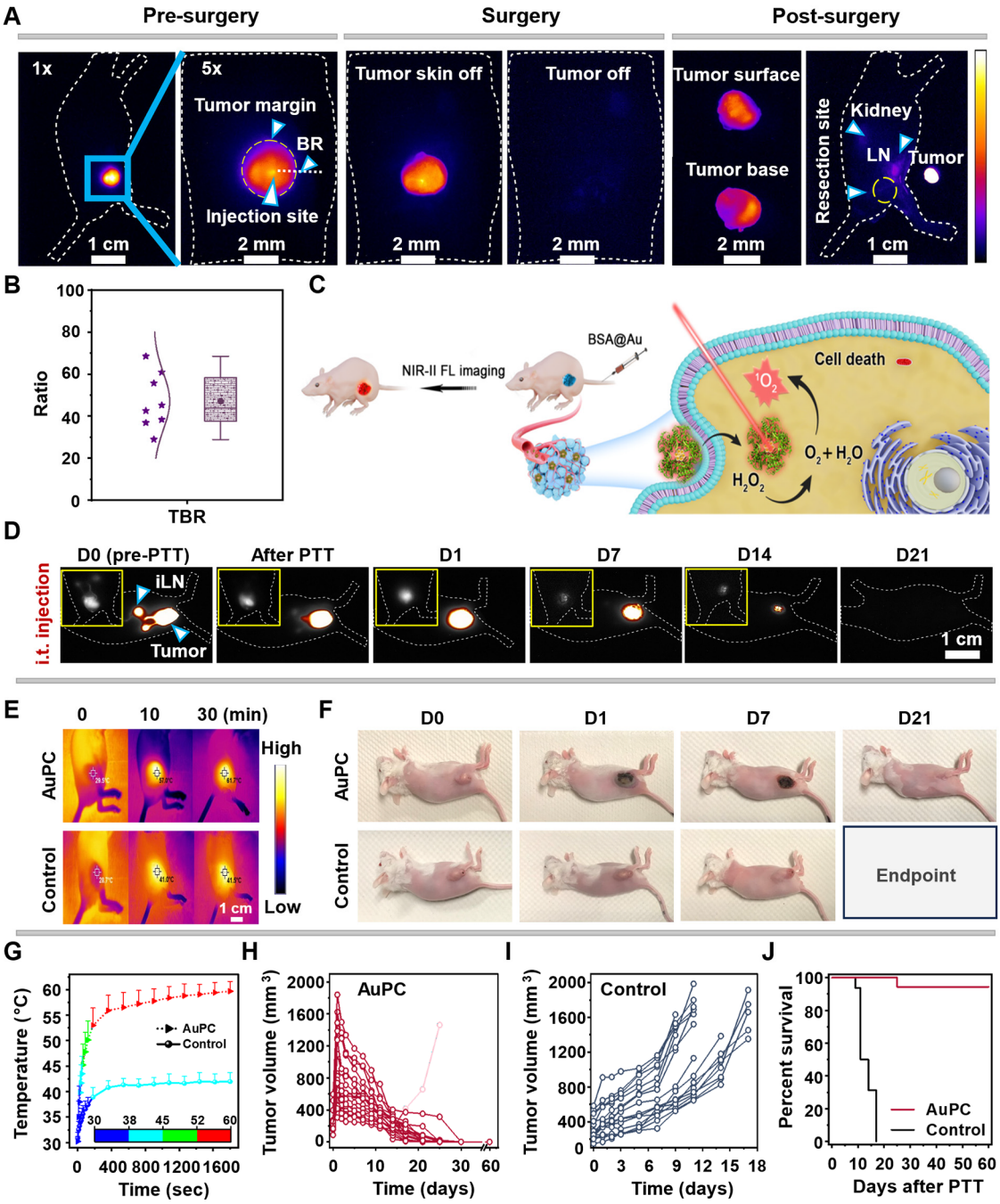

Figure 13. (A) In vivo NIR-II imaging-guided tumor resection was performed on a mouse bearing a 4T1 tumor on the right hindlimb (3 to 6-week-old female Balb/c, $n = 8$). The tumor was intratumorally administered with AuPC clusters in PBS buffer (pH 7.4, 1×, 300 μg). Presurgical, intraoperative, and postsurgical NIR-II imaging were conducted using a wide-field NIR-II fluorescence imaging system, with excitation provided by an 808 nm laser at a power density of 70 mW/cm^2. Exposure times were 3 and 7 ms for 1× and 5× magnifications, respectively, using a 1100 nm long-pass filter. The tumor area, indicated by a rectangle, was imaged at 5× magnification (exposure time 7 ms). For surgical resection, the skin covering the tumor was meticulously excised to allow NIR-II imaging of the exposed tumor, which was then removed in one step. Scale bars are 1 cm and 2 mm for 1× and 5× objectives, respectively. (B) The tumor-to-background tissue (TBR) ratio was calculated using the fluorescence intensity of tumor and nearby background after resection.[201] Reproduced with permission from ref 201. Copyright 2024, National Academy of Sciences. (C) Schematic illustration of BSA@Au nanoclusters as a PDT agent for cancer treatment.[229] Reproduced with permission from ref 229. Copyright 2022, MDPI. (D) Wide-field NIR-II imaging of mice before and after PTT, as well as at later time points, using an 808 nm laser excitation at a power density of 70 mW/cm^2 with a 1100 nm long-pass filter, exposure time was set to 40 ms. The insets display low-exposure (1 ms) NIR-II images. Arrows indicate the tumor and inguinal lymph node (iLN). A 1× objective; scale bar is 1 cm. (E) Thermal camera images of mice before and during PTT treatment; scale bar is 1 cm. (F) Color pictures of mice before and after PTT, showing obvious morphological changes on the tumor surface 1 day post-treatment, with noticeable scab formation. (G) Temperature and tumor volume changes in (H) AuPC and (I) control groups during and after post-PTT treatment, respectively. (J) Kaplan–Meier survival analyses of AuPC and control groups.[201] Reproduced with permission from ref 201. Copyright 2024, National Academy of Sciences.

https://doi.org/10.1021/acs.chemrev.4c00835
Chem. Rev. 2025, 125, 5195−5227

visualized the sacral and popliteal lymph nodes for an extended period (up to 3 days).

3.4.2. Tumor Imaging. The treatment efficacy of murine and clinical tumors relies on the efficient delivery of therapeutic agents or drug formulations to the tumor microenvironment via systemic administration with negligible "off-target" toxicity. Passive accumulation of anticancer drugs, fluorescent nanoparticles and organic dyes in solid tumors is mostly governed by the extravasation from the aberrant and leaky vasculature (EPR effect)[281] which results in low drug concentrations within tumor. In contrast, active targeting relies on directed delivery of drug-nanoparticle conjugates to overexpressed receptors on cancer cells thus assuring higher drug dosage availability in tumors.[282−284] Such targeting efficacy difference between passive and active delivery routes can directly be visualized on the molecular level with NIR-II imaging. Not only NIR-II imaging provides higher tissue-to-background (TBR) contrast compared to the NIR-I window, with active targeting at least an order of magnitude higher tumor-to-normal tissue (TNT) ratios can be achieved. High TNT values are prerequisites and qualitative measures for effective targeting assessment. Quantum dots,[75,125,128,285] organic dyes,[286,287] and rare-earth nanoparticles[78,128,288,289] with targeting moieties have been widely employed in preclinical research for tumor targeting, achieving TNT values of >40 for imaging in the NIR-IIb (>1500 nm) window.[128] In contrast, tumor targeting properties of gold nanoclusters are scarcely studied partially because of their small sizes, short blood circulations, and fast renal clearance. Although passive targeting with AuNCs via the EPR effect is ineffective, active targeting of AuNCs to tumors via conjugation to antibodies (directed targeting) or proteins (mostly altering the overall cluster size) can be achieved.

In 2021 Song et al. reported NIR-II emissive gold nanoclusters (QY 0.11%, Table 1) using thiolated cyclodextrin as both the ligand for cluster passivation and binding moiety for adamantly modified BSA (Ada-BSA) and anti-CD326 antibody (Ada-aCD326) via a host−guest complexation strategy.[223] The antibody-cluster formulation imparted active targeting properties (Figure 12A) providing ∼4-fold higher gold content (Figure 12B) and ∼3-fold stronger NIR-II cluster signals (Figure 12C) in a breast (MCF-7 tumors) cancer model. In breast (4T1 tumors) cancer model, active tumor targeting has been realized using sulfur functionalized AS1411 DNA aptamers (QY 0.2−0.4%, Table 1) with various valences in their designed sequences (Figure 12D, top).[225] In vitro, subcellular distributions of the AuNC@AS1411 were directly dependent on the DNA valences: moderate valences lead to the binding of the AuNC@AS1411 to the nucleolin protein in the nucleus, while higher DNA valences lead to the affective cell membrane binding (Figure 12D, bottom). In vivo, the designed probe was efficiently transported to the tumor site upon i.v. injection with strong NIR-II signals in the tumor persisting up to 12 h (Figure 12E).

Complexation of BSA to clusters[223] or directly preparing BSA-capped clusters[231] did induce targeting properties to some extent (much lower TNT values), it is passive in nature and is mostly due to the change in the apparent particle size to favor EPR effect and prolonged in vivo pharmacokinetics. For instance, BSA-AuNCs (QY 3.5%, Table 1) were able to passively target breast (4T1 tumors) cancer model and imaged in vivo in both NIR-I and NIR-II windows[229] (Figure 12F) reaching higher tumor signal at 6 h[227] and 10 h[229] post-i.v. injection. A high SBR of ∼7.3 with clearly visualized tumor margin could be observed for NIR-II window (Figure 12G).[229] An SBR of 8.2 was reached with BSA-AuNCs loaded with Gd ions (QY ∼ 3%, Table 1) allowing simultaneous NIR-II and MRI imaging of tumors.[231] Similar targeting properties were achieved (TNT of ∼7) when small ligand protected clusters were linked to Cy7 molecules[47] or Neutral Red (NR, QY 0.21%, Table 1)[228] via click reactions to afford a dye molecule-loaded AuNCs probes. In a recent study from the Xie group, a novel strategy for enhancing the tumor-targeting efficiency of gold nanoclusters was developed using organotropic engineering.[197] This approach involved modifying the surface chemistry of AuNCs through electrostatic interactions with positively charged chitosan, followed by coassembly with Gd^{3+}. These modifications significantly extended the circulation time of AuNCs and promoted their preferential accumulation of breast-cancer-infected (LUC^+ 4T1 tumors) orthotopic lung tumors, addressing the challenge of rapid renal clearance. In vivo studies demonstrated that these engineered AuNCs enabled high-contrast tumor imaging with SBR of ∼8, underscoring their potential for noninvasive cancer diagnostics and targeted imaging applications.

Drug-loaded clusters can also increase treatment efficacy by overcoming the tumor resistance toward chemotherapeutic drugs. One of the major obstacles for platinum drugs (cisplatin: CDDP, oxaliplatin: OxaPt, carboplatin: CarPt) resistance in cancer patients is sought to be triggered by overexpression of intracellular glutathione which binds to anticancer drugs and reduces the treatment efficacy.[290] Exogenous AuNCs (QY 0.04%, Table 1) were shown to scavenge and deplete GSH levels in cells (Figure 12H) and sensitize the drugs in vitro thus making even the resistant cells susceptible to treatment.[224] AuGSH-Pt prodrug formulations upon intraperitoneal administration to xenograft high-grade serous ovarian cancer model (HGSOC model, LUC^+ OVCAR8 tumors) assured effective accumulation of the probe inside the tumor (Figure 12I) with ∼4-fold higher Pt amounts compared to free CDDP (Figure 12J). In orthotopic tumor models, the AuGSH−Pt conjugate effectively suppressed tumor growth and extended the survival rate without significant systemic toxicity.

For more details on recent advances in tumor diagnosis and treatment using gold nanoclusters, the reader is referred to a recent comprehensive review by Zhang and colleagues.[291]

3.4.3. Image-Guided Surgical Resections and PDT/PTT Treatment. Once the tumors are successfully targeted (passively or actively), subsequent surgical or treatment actions can be followed. Alternatively, intratumoral (i.t.) injections may be employed for probes with insufficient systemic targeting abilities owing to their small sizes. For example, we have recently shown that AuPC clusters (QY 0.38%, Table 1) can successfully and uniformly distribute inside the preclinical breast (4T1) tumor bed <3 min postintratumoral administration (Figure 13A).[201] Due to its stealth nature, ∼33% and ∼31% of AuPC and AuGSH clusters respectively, penetrated the tumor interstitium and homogeneously spread out within the tumor bed, evidenced by the NIR-II signals in the extracted tumor interstitial fluid (TIF) samples and significant decrease in brightness in the excised tumors before and after centrifugation.[201] In contrast, only ∼6% of ICG was extracted into the TIF, while the tumor became even brighter due to strong association of ICG with tumor cells/proteins.[292] A high TBR ∼50 (Figure 13B) and homogeneous NIR-II signal across the tumor provided sufficiently improved tumor margin visualization and subsequent surgical resection. Notably that for intratumoral injection, few probes or drugs are known to distribute

https://doi.org/10.1021/acs.chemrev.4c00835
Chem. Rev. 2025, 125, 5195−5227

homogeneously inside tumors as most injected particles stayed predominantly localized near the injection site, hindering tumor imaging or therapeutic effects.

The gold nanoclusters served as photosensitizers for photodynamic therapy (PDT)[48,227−229] or heat generators for photothermal therapy (PTT)[47,48] for simultaneous NIR-II imaging and breast (4T1 tumors) cancer treatment applications. For example, BSA-protected AuNCs after passively targeting the tumors, showed catalase-like activity that decomposed endogenous H_2O_2 and converted released oxygen to singlet oxygen upon 808 nm laser irradiation (Figure 13C).[227,229] Thus, promoting sufficient ROS generation in hypoxic tumors for PDT treatment results from drastically inhibiting tumor growth to even complete eradication. The assembly of AuNCs-decorated up-conversion and down-conversion nanoparticles, loaded with doxorubicin for chemotherapy and methylene blue for PDT, conferred multimodal theragnostic capabilities for tumor treatment.[230] Additionally, ferrocene-loaded AuNCs were effectively utilized as chemotherapeutic agents, demonstrating the potential to generate reactive oxygen species (•OH in particular) from endogenous hydrogen peroxide within the breast (MCF-7) tumor microenvironment.[232] Atomically precise Au_{25}[201] (PC ligand, QY 0.38%, Table 1) and Au_{44}[47,48] (MBA ligand, QY ∼ 4.5%, Table 1) clusters showed high photothermal conversion efficiencies making them ideal candidates for PTT applications in breast (4T1 tumors) cancer model (Figure 13D). By leveraging the homogeneous distributions of AuPC clusters inside the tumor post intratumor administration, we have demonstrated its capability to uniformly heat the tumor up to 60 °C upon 808 nm laser irradiation, thus generating sufficient heat for tumor's thermal ablation (Figure 13E,G) and scab formation (Figure 13F).[201] Following PTT, the tumor volume drastically reduced, and overtime disappeared (Figure 13H), unlike the control group (Figure 13I), thus assuring 95%[201] (Figure 13J) survival rates. Moreover, intravenously injected PbS/CdS core−shell quantum dot[125,128]−Annexin V conjugates demonstrated a strong NIR-IIb signal localized to the tumor periphery 24 h post-PTT, with an absence of signal in the core, indicative of PTT-induced cellular death and vascular disruption. Furthermore, a 4-fold higher TNT ratio calculated for the AuPC-mediated PTT group compared to the control groups indicated that in vivo NIR-II molecular imaging of Annexin V enabled noninvasive, longitudinal assessment of apoptosis. Ex vivo flow cytometry and TUNEL staining of excised tumors 24 h post-PTT further corroborated the elevated levels of cellular apoptosis within tumor tissues.

Au[44] clusters conjugated to Cy7[47] or small-molecule immune checkpoint inhibitor NLG919[48] through a singlet oxygen-cleavable linker exhibited both PDT and PTT properties, while also allowing controlled release of NLG919 for cancer immunotherapy in breast (4T1 tumors) cancer model. In vivo, the PDT/PTT combined with the immunotherapeutic efficacy of the clusters generated reactive oxygen species (ROS) in primary tumors for PDT and elevated temperatures for PTT, leading to tumor ablation. The release of NLG919 activated the systemic immune response by upregulating the proliferation and activation of cytotoxic T lymphocytes, thereby suppressing the growth of both primary and distant tumors.[48]

4. SUMMARY AND OUTLOOK

This comprehensive review highlights recent advancements in atomically precise gold nanoclusters with a primary focus on their photoluminescent properties. We provide an in-depth discussion of the fundamental mechanisms governing photoluminescence pathways and strategic approaches for modulating radiative relaxation kinetics to enhance emission yields for fluorescence imaging. Furthermore, we outline the nonradiative decay processes that govern photothermal effects in clusters and that are crucial for effective photothermal therapy. However, here we aim to address the key challenges and potential solutions, beginning with the scalable synthesis required for mass production, followed by the precise tuning of their physicochemical properties, and concluding with the potential obstacles during their clinical translation.

4.1. Current Challenges in the Synthesis of NIR-II Emissive Molecular Gold Nanoclusters

Despite significant advancements in the synthesis of atomically precise gold nanoclusters, several critical challenges remain that hinder their widespread application in NIR-II imaging and biomedical research. The main obstacle in AuNC synthesis is obtaining atomically precise nanoclusters with a high yield. Unlike larger gold nanoparticles, whose properties, are size-dependent but not atomically defined, AuNCs require precise control at the atomic level to ensure uniformity in the electronic structure, optical properties, and stability. The formation of atomically precise clusters is highly sensitive to reaction conditions, including temperature, ligand-to-metal ratio, and reaction time. Small variations in reaction conditions can lead to polydisperse clusters with different nuclearities, necessitating additional postsynthetic purification steps to isolate atomically precise single clusters sizes. Besides, many synthetic approaches, such as ligand exchange and etching methods, yield only small quantities of desired AuNCs, limiting their large-scale production for applications. Although significant progress has been made in the synthesis and atomic-level control of composition for organic solvent-soluble gold nanoclusters, largely due to the greater availability of protective ligands and the ease of structural functionalization, achieving similar control for water-soluble clusters remains considerably more challenging. One major limitation is the restricted selection of water-soluble ligands suitable for stabilizing clusters during the synthesis. Additionally, pH regulation in aqueous solutions introduces another layer of complexity as it profoundly influences ligand binding, nucleation dynamics, and the overall stability of the clusters. Reproducibility is another hurdle in scaling up synthetic procedures for the mass production of gold nanoclusters. Variations in reaction conditions can lead to inconsistencies in the cluster size, composition, and optical properties. Maintaining consistent purity and preventing unwanted aggregation require fine-tuned control over the reaction kinetics, posing further challenges for large-scale production. Addressing these issues will require the development of robust, reproducible protocols that can be translated from the laboratory to the industrial-scale synthesis. Therefore, the realization of a truly selective "one synthesis, one size" approach remains a major challenge. We remain hopeful that future efforts, driven by extensive and systematic investigations into reaction conditions, will bring us closer to achieving precise size control in gold nanocluster synthesis for industrial mass-production.

4.2. Current Challenges in Modifying the Electronic and Optical Properties of NIR-II Emissive Molecular Gold Nanoclusters

The optical properties and stability of AuNCs are heavily influenced by ligand−metal interactions. However, designing

https://doi.org/10.1021/acs.chemrev.4c00835
Chem. Rev. 2025, 125, 5195−5227

ligands that provide both strong metal binding and desirable optical properties remains a major challenge. Many ligands used in AuNC synthesis (e.g., thiols and phosphines) can undergo exchange reactions in biological environments, leading to instability and aggregation. While strong metal−ligand interactions improve stability, they can also introduce nonradiative decay pathways that quench fluorescence. Most reported AuNCs and currently used ligands favor emissions in the visible or NIR-I range with limited success in pushing the emission beyond 1000 nm into the NIR-II window. The challenge lies in fine-tuning the electronic structure of AuNCs to achieve lower-energy transitions while maintaining a high quantum yield. Unlike semiconductor quantum dots, AuNCs rely on discrete molecular orbitals rather than extended band structures, limiting the ability to red-shift emissions. One significant limitation of AuNCs is their inherently low quantum yields in aqueous environments. For example, Au_{25} nanoclusters have shown potential as effective NIR-II probes for fluorescence imaging in small animals; their emission is typically peaked at around 1100 nm, with a relatively low quantum yield of 0.3%. This limited quantum yield constrains their sensitivity and effectiveness for in vivo imaging applications, emphasizing the need for further optimization to enhance fluorescence efficiency and achieve a further redshift in the PL peak toward the NIR-IIb window. Such optimization would enable enhanced tissue penetration, reduced scattering, and minimized background autofluorescence, thereby improving the signal-to-noise ratio and overall imaging performance. Similar to semiconducting QDs, as the energy gap decreases, the emission of gold nanoclusters undergoes a redshift. In fact, it has been demonstrated that doping the cluster core with heteroatoms is an effective strategy for modulating the energy gap, thereby enabling the tuning of photoluminescence in the desired direction. Meanwhile, the selection and optimization of ligands can significantly enhance the quantum yield, further improving the overall fluorescence efficiency. Similarly, increasing the size of the cluster allows for a red shift in emission, as the larger clusters typically exhibit smaller energy gaps. The Jin group has recently developed synthetic protocols for preparing rod-shaped nanoclusters that exhibit plasmonic-like absorption features, which can be further tuned to the NIR-IIc window. However, their PL properties have yet to be fully explored. Additionally, these clusters are soluble in organic solvents, and potential applications will likely involve their transfer into aqueous environments via their encapsulation into micellar vehicles. Therefore, achieving highly emissive gold nanoclusters with emission beyond 1100 nm remains a significant challenge. Controlling the synthesis to tune the optical properties and size with high precision is critical, especially when the demands for in vivo applications. Given the extensive focus on optimizing the properties of nanoclusters for bioimaging, this challenge aligns with our goal of enhancing their fluorescence efficiency while simultaneously shifting their emission into the NIR-IIb or even the NIR-IIc subwindows for better tissue penetration and lower autofluorescence. It will be interesting to see how developments in ligand engineering, doping strategies, and precise size control can overcome this hurdle in the future.

4.3. Current Challenges of NIR-II Emissive Molecular Gold Nanoclusters in Biomedical Applications

In this comprehensive review, we highlighted the recent advancements in near-infrared II (NIR-II) imaging utilizing atomically precise gold nanoclusters, i.e., molecular clusters. Gold nanoclusters offer significant advantages over carbon nanotubes, quantum dots, and small organic dyes due to their superior biocompatibility and smaller sizes. Unlike biliary excretable SWCNTs and QDs, which can remain in the liver and intestines longer, posing a higher risk of adverse effects, gold nanoclusters are rapidly filtered through the kidneys, thus minimizing the likelihood of long-term accumulation in the body and significantly reducing the risk of potential acute toxicity. These probes enable dynamic imaging of renal function over time, offering valuable insights into renal clearance rates and efficiency. This capability is essential for monitoring kidney health and disease progression, particularly in the early stages when standard imaging modalities and diagnostic tests may not provide adequate information. Compared with small organic dyes, molecular gold nanoclusters exhibit significantly enhanced long-term stability, resistance to photobleaching, and minimal interaction with tissues, thereby ensuring a much lower background signal. Unlike QDs and CNTs, the short circulation time of gold nanoclusters limits their efficacy for systemic tumor targeting. Thus, refining synthetic strategies to produce long-wavelength emissive gold nanoclusters with significantly improved blood circulation could greatly enhance their tumor targeting properties, achieving higher TNT ratios. This advancement could pave the way for designing more effective treatment options and rendering them ideal for vaccine applications. Recent studies have shown that doping clusters onto the surface of larger nanoparticles or preparing protein−cluster complexes can enhance their circulation half-life. However, these processes have not yet been fully refined and require further modifications and optimization to achieve consistent and efficient results. Long-circulating clusters would significantly benefit cancer-targeting interventions by providing an extended time for tumor accumulation, improving the overall efficacy of targeting strategies, and enhancing therapeutic outcomes. We have demonstrated that AuNCs hold great promise for cancer treatment, serving as both imaging probes and photothermal therapy agents. This dual-functional platform enables enhanced diagnosis and treatment, particularly when administered locally to targeted areas, allowing for more precise and effective therapeutic interventions and monitoring of treatment. However, for PTT applications of gold nanoclusters, further synthetic advancements are needed to increase photothermal conversion rates, potentially at the expense of fluorescence, to optimize their effectiveness in cancer therapy. Therefore, there is a trade-off between fluorescence imaging and thermal effects, which must be carefully balanced, depending on the specific application being targeted. As we have already mentioned above, one significant limitation of AuNCs is their inherently low quantum yields in aqueous environments. Therefore, there is a strong emphasis on manipulating their properties and structures to achieve the maximum quantum efficiency for bioimaging.

4.4. Potential Applications of AuNCs in Other Imaging Modalities

AuNCs exhibit unique optical properties that make them promising candidates for potential time-domain in vivo imaging applications. Their ultrasmall size results in discrete electronic states, leading to fluorescence emission that is highly dependent on both cluster size and surface chemistry. One of the key advantages of AuNCs in time-domain imaging is their tunable fluorescence lifetime, which can range from nanoseconds to microseconds depending on the core structure, ligand environ-

https://doi.org/10.1021/acs.chemrev.4c00835
Chem. Rev. 2025, 125, 5195−5227

ment, solvent interactions, and local biological milieu. Their long-lived fluorescence lifetimes, especially when modified with specific surface ligands, can significantly reduce background autofluorescence in biological tissues, enhancing signal-to-noise ratios for improved imaging contrast. This property is particularly useful in detecting subtle biochemical changes in the tumor microenvironment, monitoring metabolic processes, and studying the real-time pharmacokinetics of nanomedicines. This property enables their potential use in fluorescence lifetime imaging microscopy, where lifetime variations can provide molecular and environmental insights independent of fluorescence intensity. However, combining the fluorescence lifetime imaging of AuNCs with their fluorescence imaging tuned for the NIR-II window is still far from realization due to several fundamental and technical challenges. One major limitation is the relatively weak fluorescence quantum yield of AuNCs in the aqueous phase in the NIR-II region, which often results in lower photon counts, making accurate lifetime measurements challenging, especially in deep-tissue imaging, where scattering and absorption further attenuate the signal. Additionally, the fluorescence lifetimes of AuNCs are highly dependent on their surface chemistry, aggregation state, and surrounding biological environment, leading to variability that complicates precise lifetime quantification in complex in vivo settings. Furthermore, existing time-domain detection systems optimized for FLIM predominantly operate in the visible to NIR-I range (400−900 nm), whereas efficient time-resolved detection in the NIR-II region (1000−3000 nm) remains technologically underdeveloped. The limited availability of high-sensitivity detectors, such as superconducting nanowire single-photon detectors (SNSPDs) and high-efficiency InGaAs-based time-resolved photodetectors, further restricts the effective implementation of NIR-II FLIM. Additionally, challenges in designing NIR-II fluorophores with both long fluorescence lifetimes and high brightness must be addressed to fully exploit time-gated imaging for deep-tissue applications. Overcoming these hurdles will require advances in cluster engineering to enhance the NIR-II fluorescence quantum yield, improvements in time-resolved detection technologies, and the development of biocompatible probes with optimized lifetime properties for in vivo imaging. Despite these challenges, the combination of FLIM and NIR-II fluorescence imaging holds immense potential for high-contrast, functional imaging of deep tissues, enabling new possibilities in disease diagnostics, neuroimaging, and theragnostic applications.

4.5. Potential Clinical Translation of NIR-II Emissive Molecular Gold Nanoclusters

The potential clinical translation of NIR-II emissive molecular gold nanoclusters holds great promise for advancing noninvasive bioimaging techniques, offering enhanced tissue penetration, reduced scattering, and minimal autofluorescence. By leveraging their unique optical properties, these clusters could significantly improve the accuracy of early disease detection, guide surgical procedures, and enable the real-time monitoring of therapeutic interventions. However, successful clinical translation will require addressing challenges in synthesis, stability, biodistribution, and optimization of their fluorescence and photothermal properties for specific medical applications. The real-life application of NIR-II emissive molecular gold nanoclusters requires several key translational steps. (i) The synthesis of nanoclusters needs to be scaled up for cost-effective mass production, addressing current challenges related to reproducibility and consistency. This would involve refining synthetic protocols for large-scale production while maintaining high-quality and size-controlled nanoclusters. (ii) Optimizing their biocompatibility, stability, and biodistribution is essential for safe in vivo applications. Developing suitable strategies for functionalization and surface modification will be critical to ensure their stability in biological environments and enhance tumor-targeting capabilities. (iii) Rigorous preclinical studies must be conducted to assess the efficacy and safety of these nanoclusters for fluorescence imaging and disease treatment. This includes long-term toxicity studies, pharmacokinetics, and biodistribution analysis to ensure minimal toxicity and effective targeting. (iv) The clinical translation of these nanoclusters will involve regulatory approval processes, including compliance with Good Manufacturing Practices (GMP) for clinical-grade nanomaterials and demonstrating their cost-effectiveness relative to current diagnostic and therapeutic technologies. Addressing these factors, such as the high costs of production, will be crucial for making NIR-II emissive gold nanoclusters viable for widespread clinical use, ensuring that their potential in cancer treatment and diagnostic imaging can be fully realized. Finally, we provide a preliminary estimate of the potential cost per dose in Table 2.

Table 2. Research and Development Costs

Study stage	Dose calculation	Estimated cost (USD)
Preclinical studies (in vitro and in vivo)	AuNCs concentration: 10 mg/mL	1 g of gold is 93$ (value from gold avenue)
	Desired dose for in vivo imaging: 1 mg per mouse	AuNCs yield is ∼30% (0.3 g)
	Injection volume: 100 μL	1 g AuNCs would cost ∼310$
Clinical trials (Phases I−III)	1−5 mg per kg of body weight for humans	Cost per dose: 22−103$
	Average adult human weighs ∼70 kg	
	Injection dose: 70 mg (for 1 mg/kg) to 350 mg (for 5 mg/kg)	

Note, these roughly estimated values would increase drastically considering factors such as extended clinical trial durations, unforeseen regulatory hurdles, complex manufacturing scale-up, the need for specialized storage and distribution (e.g., cold chain logistics), intellectual property-related costs, and potential postmarket surveillance requirements.

In conclusion, considering the stealth, biocompatibility, and multifunctional capabilities of molecular gold clusters, we hold a highly optimiztic outlook for their eventual integration into clinical practice for disease diagnostics, advanced imaging, and targeted treatment. Their intrinsic fluorescence, tunable NIR-II emission, and efficient renal clearance position them as ideal candidates for noninvasive, high-contrast imaging and precision medicine. With continuous advancements in synthetic strategies, surface engineering, and biomedical applications, these nanoclusters are on a promising trajectory toward revolutionizing patient care. As research progresses and regulatory frameworks adapt to emerging nanotechnologies, molecular gold clusters have the potential to transform diagnostics and therapy, enabling safer, more effective, and highly specific medical interventions that improve patient outcomes and redefine modern healthcare.

https://doi.org/10.1021/acs.chemrev.4c00835
Chem. Rev. 2025, 125, 5195−5227

AUTHOR INFORMATION

Corresponding Author

Hongjie Dai − *Department of Chemistry and Bio-X, Stanford University, Stanford, California 94305, United States; Department of Chemistry, Department of Mechanical Engineering, School of Biomedical Sciences, School of Medicine, and Jockey Club STEM Lab of Nanoscience and Nanomedicine, The University of Hong Kong, Hong Kong 999077, P. R. China; Materials Innovation Institute for Life Science and Energy (MILES), HKU-SIRI, Shenzhen 518000, P. R. China;* orcid.org/0000-0002-4906-4502; Email: hdai@stanford.edu

Author

Ani Baghdasaryan − *Department of Chemistry and Bio-X, Stanford University, Stanford, California 94305, United States*

Complete contact information is available at: https://pubs.acs.org/10.1021/acs.chemrev.4c00835

Author Contributions

CRediT: Ani Baghdasaryan conceptualization, data curation, methodology, visualization, writing - original draft, writing−review and editing. Hongjie Dai conceptualization, data curation, methodology, visualization, writing, writing−review and editing, supervision and funding acquisition. CRediT: **Ani Baghdasaryan** writing - original draft, writing - review & editing; **Hongjie Dai** writing - review & editing.

Notes

The authors declare no competing financial interest.

Biographies

Hongjie Dai is currently the Sapientia Eminence Professor in Chemistry, Mechanical Engineering and the School of Biomedical Sciences at the University of Hong Kong. He is also the Jackson-Wood Professor of Chemistry, Emeritus at Stanford University. He has made seminal contributions to the fields of nanoscience and nanomedicine, including the synthesis of carbon nanotubes and graphene nanoribbons, elucidating fundamental physics in these quasi-one-dimensional systems and opening new applications of these materials in biomedical and renewable energy fields. Dai pioneered NIR-II/SWIR fluorescence imaging in 2009 by detecting the intrinsic fluorescence of carbon nanotubes in vivo, subsequently developed a series of NIR-II emitters including sulfide-based quantum dots, donor−acceptor−donor molecules and down-conversion rare-earth nanoparticles, and advanced light sheet microscopy and confocal microscopy in NIR-II/SWIR. Dai is a Member of the US National Academy of Sciences, the US National Academy of Medicine, Fellow of the American Academy of Arts and Sciences, and Foreign Member of the Chinese Academy of Sciences. Dai received the APS James McGroddy Prize for New Materials, the ACS Pure Chemistry Award, the MRS Mid-Career Researcher Award, the NIH Director's Pioneer Award, and the Humboldt Research Award, among others.

Ani Baghdasaryan received her Ph.D. in Chemistry in 2020 from the University of Geneva under the supervision of Prof. Thomas Bürgi. Her doctoral research focused on the designed synthesis and surface modification of atomically precise metal nanoclusters, employing ligand-exchange reactions to tailor their chiroptical properties. Through meticulous structural and spectroscopic studies, she elucidated the mechanisms governing chiral induction in these nanoscale systems, contributing to the fundamental understanding of cluster-based optical activity. Following her Ph.D., she joined Professor Hongjie Dai's lab at Stanford University as a postdoctoral researcher, where she has been working at the interface of nanomaterials, bioimaging, and cancer theragnostic. Her research focuses on the development of highly emissive metal nanoclusters for NIR-II fluorescence imaging, enabling deep-tissue visualization with exceptional resolution, minimal autofluorescence, and improved penetration depth compared to conventional imaging techniques. She has designed nanoclusters with optimized surface chemistries to enhance their photostability, quantum yield, and in vivo biosafety, making them promising candidates for noninvasive imaging of vasculature, lymphatic systems, and tumor microenvironments. Her work has contributed to the advancement of imaging-guided surgical navigation, where these nanoclusters provide high-contrast visualization of tumors and sentinel lymph nodes, aiding in precise tumor resection.

ACKNOWLEDGMENTS

The work reviewed here by us was supported by the National Institutes of Health Pioneer Award NIH DP1-NS-105737. Dai's current work is supported by General Research Fund (17212424) from the Research Grants Council of Hong Kong SAR.

REFERENCES

(1) Jin, R.; Zeng, C.; Zhou, M.; Chen, Y. Atomically Precise Colloidal Metal Nanoclusters and Nanoparticles: Fundamentals and Opportunities. *Chem. Rev.* **2016**, *116*, 10346−10413.

(2) Chakraborty, I.; Pradeep, T. Atomically Precise Clusters of Noble Metals: Emerging Link between Atoms and Nanoparticles. *Chem. Rev.* **2017**, *117*, 8208−8271.

(3) Zhou, M.; Jin, R. Optical Properties and Excited-State Dynamics of Atomically Precise Gold Nanoclusters. *Annu. Rev. Phys. Chem.* **2021**, *72*, 121−142.

(4) Brust, M.; Walker, M.; Bethell, D.; Schiffrin, D. J.; Whyman, R. Synthesis of Thiol-Derivatised Gold Nanoparticles in a Two-Phase Liquid-Liquid System. *J. Chem. Soc., Chem. Commun.* **1994**, *0* (7), 801−802.

(5) Yan, Q.; Yuan, Z.; Wu, Y.; Zhou, C.; Dai, Y.; Wan, X.; Yang, D.; Liu, X.; Xue, N.; Zhu, Y.; Yang, Y. Atomically Precise Water-Soluble Gold Nanoclusters: Synthesis and Biomedical Application. *Precision Chemistry* **2023**, *1*, 468−479.

(6) Zhang, J.; Li, Z.; Zheng, K.; Li, G. Synthesis and Characterization of Size-Controlled Atomically Precise Gold Clusters. *Physical Sciences Reviews* **2018**, *3*, 20170083.

(7) Zhang, B.; Chen, J.; Cao, Y.; Chai, O. J. H.; Xie, J. Ligand Design in Ligand-Protected Gold Nanoclusters. *Small* **2021**, *17*, 2004381.

(8) Zhu, Q.; Huang, X.; Zeng, Y.; Sun, K.; Zhou, L.; Liu, Y.; Luo, L.; Tian, S.; Sun, X. Controllable Synthesis and Electrocatalytic Applications of Atomically Precise Gold Nanoclusters. *Nanoscale Adv.* **2021**, *3*, 6330−6341.

(9) Wang, Y.; Bürgi, T. Ligand Exchange Reactions on Thiolate-Protected Gold Nanoclusters. *Nanoscale Adv.* **2021**, *3*, 2710−2727.

(10) Baghdasaryan, A.; Martin, K.; Lawson Daku, L. M.; Mastropasqua Talamo, M.; Avarvari, N.; Bürgi, T. Ligand Exchange Reactions on the Chiral Au 38 Cluster: CD Modulation Caused by the Modification of the Ligand Shell Composition. *Nanoscale* **2020**, *12*, 18160−18170.

(11) Baghdasaryan, A.; Brun, E.; Wang, Y.; Salassa, G.; Lacour, J.; Bürgi, T. Combined Spectroscopic Studies on Post-Functionalized Au_{25} Cluster as an ATR-FTIR Sensor for Cations. *Chem. Sci.* **2021**, *12*, 7419−7427.

(12) Zhao, J.; Ziarati, A.; Rosspeintner, A.; Wang, Y.; Bürgi, T. Engineering Ligand Chemistry on Au 25 Nanoclusters: From Unique Ligand Addition to Precisely Controllable Ligand Exchange. *Chem. Sci.* **2023**, *14*, 7665−7674.

(13) Shichibu, Y.; Negishi, Y.; Tsunoyama, H.; Kanehara, M.; Teranishi, T.; Tsukuda, T. Extremely High Stability of Glutathionate-

Protected Au25 Clusters Against Core Etching. *Small* **2007**, *3*, 835−839.
(14) Dharmaratne, A. C.; Krick, T.; Dass, A. Nanocluster Size Evolution Studied by Mass Spectrometry in Room Temperature Au 25 (SR) 18 Synthesis. *J. Am. Chem. Soc.* **2009**, *131*, 13604−13605.
(15) Schaaff, T. G.; Whetten, R. L. Controlled Etching of Au:SR Cluster Compounds. *J. Phys. Chem. B* **1999**, *103*, 9394−9396.
(16) Jin, R.; Qian, H.; Wu, Z.; Zhu, Y.; Zhu, M.; Mohanty, A.; Garg, N. Size Focusing: A Methodology for Synthesizing Atomically Precise Gold Nanoclusters. *J. Phys. Chem. Lett.* **2010**, *1*, 2903−2910.
(17) Kang, X.; Zhu, M. Transformation of Atomically Precise Nanoclusters by Ligand-Exchange. *Chem. Mater.* **2019**, *31*, 9939−9969.
(18) Zeng, C.; Qian, H.; Li, T.; Li, G.; Rosi, N. L.; Yoon, B.; Barnett, R. N.; Whetten, R. L.; Landman, U.; Jin, R. Total Structure and Electronic Properties of the Gold Nanocrystal Au 36 (SR) 24. *Angew. Chem., Int. Ed.* **2012**, *51*, 13114−13118.
(19) Das, A.; Liu, C.; Zeng, C.; Li, G.; Li, T.; Rosi, N. L.; Jin, R. Cyclopentanethiolato-Protected Au 36 (SC 5 H 9) 24 Nanocluster: Crystal Structure and Implications for the Steric and Electronic Effects of Ligand. *J. Phys. Chem. A* **2014**, *118*, 8264−8269.
(20) Nimmala, P. R.; Knoppe, S.; Jupally, V. R.; Delcamp, J. H.; Aikens, C. M.; Dass, A. Au 36 (SPh) 24 Nanomolecules: X-Ray Crystal Structure, Optical Spectroscopy, Electrochemistry, and Theoretical Analysis. *J. Phys. Chem. B* **2014**, *118*, 14157−14167.
(21) Liu, H.; Wang, L.; Xue, Z.; Zhang, X. Atomic Precise Gold Nanoclusters: Toward the Customize Synthesis, Precision Medicine. *Particle & Particle Systems Characterization* **2023**, *40*, 2300084.
(22) McCandler, C. A.; Pihlajamäki, A.; Malola, S.; Häkkinen, H.; Persson, K. A. Gold-Thiolate Nanocluster Dynamics and Intercluster Reactions Enabled by a Machine Learned Interatomic Potential. *ACS Nano* **2024**, *18*, 19014−19023.
(23) Ma, H.; Liu, L.; He, H.; Sun, S.; Yang, S.; Huang, Y.; Li, Y.; Tan, K.; Liu, H.; Liu, S.; Li, Y.; Liu, C.; Liu, P.; Wang, H.; Zhang, X.-D. Atomically Precise Ag Clusters for Intelligent NIR-II Imaging. *Matter* **2024**, *7*, 1660−1676.
(24) Ramankutty, K. K.; Yang, H.; Baghdasaryan, A.; Teyssier, J.; Nicu, V. P.; Buergi, T. Molecule-like and Lattice Vibrations in Metal Clusters. *Phys. Chem. Chem. Phys.* **2022**, *24*, 13848−13859.
(25) Adnan, R. H.; Madridejos, J. M. L.; Alotabi, A. S.; Metha, G. F.; Andersson, G. G. A Review of State of the Art in Phosphine Ligated Gold Clusters and Application in Catalysis. *Advanced Science* **2022**, *9*, 2105692.
(26) Yuan, X.; Zhu, M. Recent Advances in Atomically Precise Metal Nanoclusters for Electrocatalytic Applications. *Inorg. Chem. Front* **2023**, *10*, 3995−4007.
(27) Li, S.; Du, X.; Liu, Z.; Li, Y.; Shao, Y.; Jin, R. Size Effects of Atomically Precise Gold Nanoclusters in Catalysis. *Precision Chemistry* **2023**, *1*, 14−28.
(28) Xiao, Y.; Wu, Z.; Yao, Q.; Xie, J. Luminescent Metal Nanoclusters: Biosensing Strategies and Bioimaging Applications. *Aggregate* **2021**, *2*, 114−132.
(29) Nonappa. Luminescent Gold Nanoclusters for Bioimaging Applications. *Beilstein J. Nanotechnol.* **2020**, *11*, 533−546..
(30) Zhang, C.; Gao, X.; Chen, W.; He, M.; Yu, Y.; Gao, G.; Sun, T. Advances of Gold Nanoclusters for Bioimaging. *iScience* **2022**, *25*, 105022.
(31) Mordini, D.; Mavridi-Printezi, A.; Menichetti, A.; Cantelli, A.; Li, X.; Montalti, M. Luminescent Gold Nanoclusters for Bioimaging: Increasing the Ligand Complexity. *Nanomaterials* **2023**, *13*, 648.
(32) Ma, H.; Wang, J.; Zhang, X.-D. Near-Infrared II Emissive Metal Clusters: From Atom Physics to Biomedicine. *Coord. Chem. Rev.* **2021**, *448*, 214184.
(33) Zeng, C.; Jin, R. Chiral Gold Nanoclusters: Atomic Level Origins of Chirality. *Chem. Asian J.* **2017**, *12*, 1839−1850.
(34) Li, Y.; Jin, R. Magnetism of Atomically Precise Gold and Doped Nanoclusters: Delocalized Spin and Interparticle Coupling. *J. Phys. Chem. C* **2021**, *125*, 15773−15784.
(35) Li, Y.; Zhou, M.; Jin, R. Programmable Metal Nanoclusters with Atomic Precision. *Adv. Mater.* **2021**, *33*, 2006591.
(36) Li, S.; Tian, W.; Liu, Y. The Ligand Effect of Atomically Precise Gold Nanoclusters in Tailoring Catalytic Properties. *Nanoscale* **2021**, *13*, 16847−16859.
(37) Kawawaki, T.; Ebina, A.; Hosokawa, Y.; Ozaki, S.; Suzuki, D.; Hossain, S.; Negishi, Y. Thiolate-Protected Metal Nanoclusters: Recent Development in Synthesis, Understanding of Reaction, and Application in Energy and Environmental Field. *Small* **2021**, *17*, 2005328.
(38) Katla, S. K.; Zhang, J.; Castro, E.; Bernal, R. A.; Li, X. Atomically Precise Au25(SG)18 Nanoclusters: Rapid Single-Step Synthesis and Application in Photothermal Therapy. *ACS Appl. Mater. Interfaces* **2018**, *10*, 75−82.
(39) Bhattacharya, S. R.; Bhattacharya, K.; Xavier, V. J.; Ziarati, A.; Picard, D.; Bürgi, T. The Atomically Precise Gold/Captopril Nanocluster Au $_{25}$ (Capt) $_{18}$ Gains Anticancer Activity by Inhibiting Mitochondrial Oxidative Phosphorylation. *ACS Appl. Mater. Interfaces* **2022**, *14*, 29521−29536.
(40) Chen, T.; Fung, V.; Yao, Q.; Luo, Z.; Jiang, D. E.; Xie, J. Synthesis of Water-Soluble [Au25(SR)18]- Using a Stoichiometric Amount of NaBH4. *J. Am. Chem. Soc.* **2018**, *140*, 11370−11377.
(41) Yuan, X.; Zhang, B.; Luo, Z.; Yao, Q.; Leong, D. T.; Yan, N.; Xie, J. Balancing the Rate of Cluster Growth and Etching for Gram-Scale Synthesis of Thiolate-Protected Au25 Nanoclusters with Atomic Precision. *Angewandte Chemie - International Edition* **2014**, *53*, 4623−4627.
(42) Zeng, C.; Liu, C.; Pei, Y.; Jin, R. Thiol Ligand-Induced Transformation of Au 38 (SC 2 H 4 Ph) 24 to Au 36 (SPh- t -Bu) 24. *ACS Nano* **2013**, *7*, 6138−6145.
(43) Yu, Y.; Luo, Z.; Chevrier, D. M.; Leong, D. T.; Zhang, P.; Jiang, D. E.; Xie, J. Identification of a Highly Luminescent Au22(SG)18 Nanocluster. *J. Am. Chem. Soc.* **2014**, *136*, 1246−1249.
(44) Ma, H.; Zhang, X.; Liu, L.; Huang, Y.; Sun, S.; Chen, K.; Xin, Q.; Liu, P.; Yan, Y.; Wang, Y.; Li, Y.; Liu, H.; Zhao, R.; Tan, K.; Chen, X.; Yuan, X.; Li, Y.; Liu, Y.; Dai, H.; Liu, C.; Wang, H.; Zhang, X.-D. Bioactive NIR-II Gold Clusters for Three-Dimensional Imaging and Acute Inflammation Inhibition. *Sci. Adv.* **2023**, *9*, No. eadh7828.
(45) Baghdasaryan, A.; Wang, F.; Ren, F.; Ma, Z.; Li, J.; Zhou, X.; Grigoryan, L.; Xu, C.; Dai, H. Phosphorylcholine-Conjugated Gold-Molecular Clusters Improve Signal for Lymph Node NIR-II Fluorescence Imaging in Preclinical Cancer Models. *Nat. Commun.* **2022**, *13*, 5613.
(46) Bertorelle, F.; Wegner, K. D.; PerićBakulić, M.; Fakhouri, H.; Comby-Zerbino, C.; Sagar, A.; Bernadó, P.; Resch-Genger, U.; Bonačić-Koutecký, V.; Le Guével, X.; Antoine, R. Tailoring the NIR-II Photoluminescence of Single Thiolated Au $_{25}$ Nanoclusters by Selective Binding to Proteins. *Chem. Eur. J.* **2022**, *28*, No. e202200570.
(47) Yang, G.; Mu, X.; Pan, X.; Tang, Y.; Yao, Q.; Wang, Y.; Jiang, F.; Du, F.; Xie, J.; Zhou, X.; Yuan, X. Ligand Engineering of Au $_{44}$ Nanoclusters for NIR-II Luminescent and Photoacoustic Imaging-Guided Cancer Photothermal Therapy. *Chem. Sci.* **2023**, *14*, 4308−4318.
(48) Yang, G.; Pan, X.; Feng, W.; Yao, Q.; Jiang, F.; Du, F.; Zhou, X.; Xie, J.; Yuan, X. Engineering Au $_{44}$ Nanoclusters for NIR-II Luminescence Imaging-Guided Photoactivatable Cancer Immunotherapy. *ACS Nano* **2023**, *17*, 15605−15614.
(49) Ma, J.; Yang, M.; Zhang, B.; Niu, M. The Roles of Templates Consisting of Amino Acids in the Synthesis and Application of Gold Nanoclusters. *Nanoscale* **2024**, *16*, 7287−7306.
(50) Hao, D.; Zhang, X.; Su, R.; Wang, Y.; Qi, W. Biomolecule-Protected Gold Nanoclusters: Synthesis and Biomedical Applications. *J. Mater. Chem. B* **2023**, *11*, 5051−5070.
(51) Yu, Y.; Chen, X.; Yao, Q.; Yu, Y.; Yan, N.; Xie, J. Scalable and Precise Synthesis of Thiolated Au $_{10-12}$, Au $_{15}$, Au $_{18}$, and Au $_{25}$ Nanoclusters via PH Controlled CO Reduction. *Chem. Mater.* **2013**, *25*, 946−952.
(52) Srinivasulu, Y. G.; Goswami, N.; Yao, Q.; Xie, J. High-Yield Synthesis of AIE-Type Au $_{22}$ (SG) $_{18}$ Nanoclusters through Precursor Engineering and Its PH-Dependent Size Transformation. *J. Phys. Chem. C* **2021**, *125*, 4066−4076.

https://doi.org/10.1021/acs.chemrev.4c00835
Chem. Rev. 2025, 125, 5195−5227

(53) Nayak, K. S.; Lim, Y.; Campbell-Washburn, A. E.; Steeden, J. Real-Time Magnetic Resonance Imaging. *Journal of Magnetic Resonance Imaging* **2022**, *55*, 81−99.
(54) Geethanath, S.; Vaughan, J. T. Accessible Magnetic Resonance Imaging: A Review. *Journal of Magnetic Resonance Imaging* **2019**, *49*, No. e65-e77.
(55) Thomas, K. E.; Fotaki, A.; Botnar, R. M.; Ferreira, V. M. Imaging Methods: Magnetic Resonance Imaging. *Circ Cardiovasc Imaging* **2023**, *16*, No. E014068.
(56) Heck, L.; Herzen, J. Recent Advances in X-Ray Imaging of Breast Tissue: From Two- to Three-Dimensional Imaging. *Physica Medica* **2020**, *79*, 69−79.
(57) Siewerdsen, J. H. Image Quality Models for 2D and 3D X-ray Imaging Systems: A Perspective Vignette. *Med. Phys.* **2023**, *50*, 109−116.
(58) Staufer, T.; Grüner, F. Review of Development and Recent Advances in Biomedical X-Ray Fluorescence Imaging. *Int. J. Mol. Sci.* **2023**, *24*, 10990.
(59) Golemati, S.; Cokkinos, D. D. Recent Advances in Vascular Ultrasound Imaging Technology and Their Clinical Implications. *Ultrasonics* **2022**, *119*, 106599.
(60) Carson, P. L. Ultrasound: Imaging, Development, Application. *Med. Phys.* **2023**, *50*, 35−39.
(61) Fadel, B. M.; Kazzi, B.; Mohty, D. Ultrasound Imaging of the Superior Vena Cava: A State-of-the-Art Review. *Journal of the American Society of Echocardiography* **2023**, *36*, 447−463.
(62) Böttcher, B.; Zsarnoczay, E.; Varga-Szemes, A.; Schoepf, U. J.; Meinel, F. G.; van Assen, M.; De Cecco, C. N. Dual-Energy Computed Tomography in Cardiac Imaging. *Radiol Clin North Am.* **2023**, *61*, 995−1009.
(63) Ibad, H. A.; de Cesar Netto, C.; Shakoor, D.; Sisniega, A.; Liu, S. Z.; Siewerdsen, J. H.; Carrino, J. A.; Zbijewski, W.; Demehri, S. Computed Tomography. *Invest Radiol* **2023**, *58*, 99−110.
(64) Vinogradskiy, Y. CT-Based Ventilation Imaging in Radiation Oncology. *BJR|Open* **2019**, *1*, 20180035.
(65) Tai, Y.-C. High-Resolution Imaging Using Virtual-Pinhole PET Concept. *PET Clin* **2024**, *19*, 69−82.
(66) Schwenck, J.; Sonanini, D.; Cotton, J. M.; Rammensee, H.-G.; la Fougère, C.; Zender, L.; Pichler, B. J. Advances in PET Imaging of Cancer. *Nat. Rev. Cancer* **2023**, *23*, 474−490.
(67) Rahmim, A.; Lodge, M. A.; Karakatsanis, N. A.; Panin, V. Y.; Zhou, Y.; McMillan, A.; Cho, S.; Zaidi, H.; Casey, M. E.; Wahl, R. L. Dynamic Whole-Body PET Imaging: Principles, Potentials and Applications. *Eur. J. Nucl. Med. Mol. Imaging* **2019**, *46*, 501−518.
(68) Yoon, S.; Cheon, S. Y.; Park, S.; Lee, D.; Lee, Y.; Han, S.; Kim, M.; Koo, H. Recent Advances in Optical Imaging through Deep Tissue: Imaging Probes and Techniques. *Biomater Res.* **2022**, *26*, 57.
(69) Pirovano, G.; Roberts, S.; Kossatz, S.; Reiner, T. Optical Imaging Modalities: Principles and Applications in Preclinical Research and Clinical Settings. *J. Nucl. Med.* **2020**, *61*, 1419−1427.
(70) Hong, G.; Antaris, A. L.; Dai, H. Near-Infrared Fluorophores for Biomedical Imaging. *Nat. Biomed Eng.* **2017**, *1*, 0010.
(71) Wang, F.; Zhong, Y.; Bruns, O.; Liang, Y.; Dai, H. In Vivo NIR-II Fluorescence Imaging for Biology and Medicine. *Nat. Photonics* **2024**, *18*, 535−547.
(72) Schmidt, E. L.; Ou, Z.; Ximendes, E.; Cui, H.; Keck, C. H. C.; Jaque, D.; Hong, G. Near-Infrared II Fluorescence Imaging. *Nature Reviews Methods Primers* **2024**, *4*, 23.
(73) Smith, A. M.; Mancini, M. C.; Nie, S. Second Window for in Vivo Imaging. *Nat. Nanotechnol* **2009**, *4*, 710−711.
(74) Li, C.; Wang, Q. Challenges and Opportunities for Intravital Near-Infrared Fluorescence Imaging Technology in the Second Transparency Window. *ACS Nano* **2018**, *12*, 9654−9659.
(75) Ma, Z.; Wang, F.; Zhong, Y.; Salazar, F.; Li, J.; Zhang, M.; Ren, F.; Wu, A. M.; Dai, H. Cross-Link-Functionalized Nanoparticles for Rapid Excretion in Nanotheranostic Applications. *Angewandte Chemie - International Edition* **2020**, *59*, 20552−20560.
(76) Zhang, M.; Yue, J.; Cui, R.; Ma, Z.; Wan, H.; Wang, F.; Zhu, S.; Zhou, Y.; Kuang, Y.; Zhong, Y.; Pang, D. W.; Dai, H. Bright Quantum Dots Emitting at ∼ 1,600 Nm in the NIR-IIb Window for Deep Tissue Fluorescence Imaging. *Proc. Natl. Acad. Sci. U. S. A.* **2018**, *115*, 6590−6595.
(77) Diao, S.; Hong, G.; Antaris, A. L.; Blackburn, J. L.; Cheng, K.; Cheng, Z.; Dai, H. Biological Imaging without Autofluorescence in the Second Near-Infrared Region. *Nano Res.* **2015**, *8*, 3027−3034.
(78) Zhong, Y.; Ma, Z.; Wang, F.; Wang, X.; Yang, Y.; Liu, Y.; Zhao, X.; Li, J.; Du, H.; Zhang, M.; Cui, Q.; Zhu, S.; Sun, Q.; Wan, H.; Tian, Y.; Liu, Q.; Wang, W.; Garcia, K. C.; Dai, H. In Vivo Molecular Imaging for Immunotherapy Using Ultra-Bright near-Infrared-IIb Rare-Earth Nanoparticles. *Nat. Biotechnol.* **2019**, *37*, 1322−1331.
(79) Li, W.; Zhang, G.; Liu, L. Near-Infrared Inorganic Nanomaterials for Precise Diagnosis and Therapy. *Front Bioeng Biotechnol* **2021**, *9*, 768927.
(80) Cao, J.; Zhu, B.; Zheng, K.; He, S.; Meng, L.; Song, J.; Yang, H. Recent Progress in NIR-II Contrast Agent for Biological Imaging. *Front Bioeng Biotechnol* **2020**, *7*, 487.
(81) Ding, F.; Zhan, Y.; Lu, X.; Sun, Y. Recent Advances in Near-Infrared II Fluorophores for Multifunctional Biomedical Imaging. *Chem. Sci.* **2018**, *9*, 4370−4380.
(82) Dunn, B.; Hanafi, M.; Hummel, J.; Cressman, J.; Veneziano, R.; Chitnis, P. NIR-II Nanoprobes: A Review of Components-Based Approaches to Next-Generation Bioimaging Probes. *Bioengineering* **2023**, *10*, 954.
(83) Liu, Y.; Li, Y.; Koo, S.; Sun, Y.; Liu, Y.; Liu, X.; Pan, Y.; Zhang, Z.; Du, M.; Lu, S.; Qiao, X.; Gao, J.; Wang, X.; Deng, Z.; Meng, X.; Xiao, Y.; Kim, J. S.; Hong, X. Versatile Types of Inorganic/Organic NIR-IIa/IIb Fluorophores: From Strategic Design toward Molecular Imaging and Theranostics. *Chem. Rev.* **2022**, *122*, 209−268.
(84) Lu, C.-H.; Hsiao, J.-K. Indocyanine Green. *Tzu Chi Med. J.* **2021**, *33*, 317−322.
(85) SPARTALIS, E.; NTOKOS, G.; GEORGIOU, K.; ZOGRAFOS, G.; TSOUROUFLIS, G.; DIMITROULIS, D.; NIKITEAS, N. I. Intraoperative Indocyanine Green (ICG) Angiography for the Identification of the Parathyroid Glands: Current Evidence and Future Perspectives. *In Vivo (Brooklyn)* **2020**, *34*, 23−32.
(86) Lütken, C. D.; Achiam, M. P.; Svendsen, M. B.; Boni, L.; Nerup, N. Optimizing Quantitative Fluorescence Angiography for Visceral Perfusion Assessment. *Surg Endosc* **2020**, *34*, 5223−5233.
(87) Son, G. M.; Ahn, H.; Lee, I. Y.; Lee, S. M.; Park, S.-H.; Baek, K.-R. Clinical Effect and Standardization of Indocyanine Green Angiography in the Laparoscopic Colorectal Surgery. *Journal of Minimally Invasive Surgery* **2021**, *24*, 113−122.
(88) Norat, P.; Soldozy, S.; Elsarrag, M.; Sokolowski, J.; Yağmurlu, K.; Park, M. S.; Tvrdik, P.; Kalani, M. Y. S. Application of Indocyanine Green Videoangiography in Aneurysm Surgery: Evidence, Techniques, Practical Tips. *Front Surg* **2019**, *6*, 34.
(89) Sakka, S. G. Assessment of Liver Perfusion and Function by Indocyanine Green in the Perioperative Setting and in Critically Ill Patients. *J. Clin Monit Comput* **2018**, *32*, 787−796.
(90) Gasperi, A. De; Mazza, E.; Prosperi, M. Indocyanine Green Kinetics to Assess Liver Function: Ready for a Clinical Dynamic Assessment in Major Liver Surgery? *World J. Hepatol* **2016**, *8*, 355.
(91) Papadia, A.; Gasparri, M. L.; Buda, A.; Mueller, M. D. Sentinel Lymph Node Mapping in Endometrial Cancer: Comparison of Fluorescence Dye with Traditional Radiocolloid and Blue. *J. Cancer Res. Clin Oncol* **2017**, *143*, 2039−2048.
(92) Kim, J.-H.; Ku, M.; Yang, J.; Byeon, H. K. Recent Developments of ICG-Guided Sentinel Lymph Node Mapping in Oral Cancer. *Diagnostics* **2021**, *11*, 891.
(93) Jimenez-Lillo, J.; Villegas-Tovar, E.; Momblan-Garcia, D.; Turrado-Rodriguez, V.; Ibarzabal-Olano, A.; De Lacy, B.; Diaz-Giron-Gidi, A.; Faes-Petersen, R.; Martinez-Portilla, R. J.; Lacy, A. Performance of Indocyanine-Green Imaging for Sentinel Lymph Node Mapping and Lymph Node Metastasis in Esophageal Cancer: Systematic Review and Meta-Analysis. *Ann. Surg Oncol* **2021**, *28*, 4869−4877.
(94) Lin, N.; Gao, J.; Wang, H.; Zhang, H.; Xiang, Y.; Ma, X. Diagnostic Value of Indocyanine Green for Sentinel Lymph Node

https://doi.org/10.1021/acs.chemrev.4c00835
Chem. Rev. 2025, 125, 5195−5227

Mapping and Lymph Node Metastasis in Oral/Oropharyngeal Carcinoma. *Oral Oncol* **2021**, *122*, 105563.
(95) Seah, D.; Cheng, Z.; Vendrell, M. Fluorescent Probes for Imaging in Humans: Where Are We Now? *ACS Nano* **2023**, *17*, 19478−19490.
(96) Liu, R.; Xu, Y.; Xu, K.; Dai, Z. Current Trends and Key Considerations in the Clinical Translation of Targeted Fluorescent Probes for Intraoperative Navigation. *Aggregate* **2021**, *2*, No. e23.
(97) Voskuil, F. J.; de Jongh, S. J.; Hooghiemstra, W. T. R.; Linssen, M. D.; Steinkamp, P. J.; de Visscher, S. A. H. J.; Schepman, K.-P.; Elias, S. G.; Meersma, G.-J.; Jonker, P. K. C.; Doff, J. J.; Jorritsma-Smit, A.; Nagengast, W. B.; van der Vegt, B.; Robinson, D. J.; van Dam, G. M.; Witjes, M. J. H. Fluorescence-Guided Imaging for Resection Margin Evaluation in Head and Neck Cancer Patients Using Cetuximab-800CW: A Quantitative Dose-Escalation Study. *Theranostics* **2020**, *10*, 3994−4005.
(98) Rosenthal, E. L.; Warram, J. M.; de Boer, E.; Chung, T. K.; Korb, M. L.; Brandwein-Gensler, M.; Strong, T. V.; Schmalbach, C. E.; Morlandt, A. B.; Agarwal, G.; Hartman, Y. E.; Carroll, W. R.; Richman, J. S.; Clemons, L. K.; Nabell, L. M.; Zinn, K. R. Safety and Tumor Specificity of Cetuximab-IRDye800 for Surgical Navigation in Head and Neck Cancer. *Clin. Cancer Res.* **2015**, *21*, 3658−3666.
(99) Gao, R. W.; Teraphongphom, N.; de Boer, E.; van den Berg, N. S.; Divi, V.; Kaplan, M. J.; Oberhelman, N. J.; Hong, S. S.; Capes, E.; Colevas, A. D.; Warram, J. M.; Rosenthal, E. L. Safety of Panitumumab-IRDye800CW and Cetuximab-IRDye800CW for Fluorescence-Guided Surgical Navigation in Head and Neck Cancers. *Theranostics* **2018**, *8*, 2488−2495.
(100) Lamberts, L. E.; Koch, M.; de Jong, J. S.; Adams, A. L. L.; Glatz, J.; Kranendonk, M. E. G.; Terwisscha van Scheltinga, A. G. T.; Jansen, L.; de Vries, J.; Lub-de Hooge, M. N.; Schröder, C. P.; Jorritsma-Smit, A.; Linssen, M. D.; de Boer, E.; van der Vegt, B.; Nagengast, W. B.; Elias, S. G.; Oliveira, S.; Witkamp, A. J.; Mali, W. P. Th. M.; Van der Wall, E.; van Diest, P. J.; de Vries, E. G. E.; Ntziachristos, V.; van Dam, G. M. Tumor-Specific Uptake of Fluorescent Bevacizumab-IRDye800CW Microdosing in Patients with Primary Breast Cancer: A Phase I Feasibility Study. *Clin. Cancer Res.* **2017**, *23*, 2730−2741.
(101) Miller, S. E.; Tummers, W. S.; Teraphongphom, N.; van den Berg, N. S.; Hasan, A.; Ertsey, R. D.; Nagpal, S.; Recht, L. D.; Plowey, E. D.; Vogel, H.; Harsh, G. R.; Grant, G. A.; Li, G. H.; Rosenthal, E. L. First-in-Human Intraoperative near-Infrared Fluorescence Imaging of Glioblastoma Using Cetuximab-IRDye800. *J. Neurooncol* **2018**, *139*, 135−143.
(102) Warram, J. M.; de Boer, E.; Korb, M.; Hartman, Y.; Kovar, J.; Markert, J. M.; Gillespie, G. Y.; Rosenthal, E. L. Fluorescence-Guided Resection of Experimental Malignant Glioma Using Cetuximab-IRDye 800CW. *Br J. Neurosurg* **2015**, *29*, 850−858.
(103) Hekman, M. C.; Rijpkema, M.; Muselaers, C. H.; Oosterwijk, E.; Hulsbergen-Van de Kaa, C. A.; Boerman, O. C.; Oyen, W. J.; Langenhuijsen, J. F.; Mulders, P. F. Tumor-Targeted Dual-Modality Imaging to Improve Intraoperative Visualization of Clear Cell Renal Cell Carcinoma: A First in Man Study. *Theranostics* **2018**, *8*, 2161−2170.
(104) Harlaar, N. J.; Koller, M.; de Jongh, S. J.; van Leeuwen, B. L.; Hemmer, P. H.; Kruijff, S.; van Ginkel, R. J.; Been, L. B.; de Jong, J. S.; Kats-Ugurlu, G.; Linssen, M. D.; Jorritsma-Smit, A.; van Oosten, M.; Nagengast, W. B.; Ntziachristos, V.; van Dam, G. M. Molecular Fluorescence-Guided Surgery of Peritoneal Carcinomatosis of Colorectal Origin: A Single-Centre Feasibility Study. *Lancet Gastroenterol Hepatol* **2016**, *1*, 283−290.
(105) Zhang, N.; Lu, C.; Chen, M.; Xu, X.; Shu, G.; Du, Y.; Ji, J. Recent Advances in Near-Infrared II Imaging Technology for Biological Detection. *J. Nanobiotechnology* **2021**, *19*, 132.
(106) Gong, H.; Peng, R.; Liu, Z. Carbon Nanotubes for Biomedical Imaging: The Recent Advances. *Adv. Drug Deliv Rev.* **2013**, *65*, 1951−1963.
(107) Mandal, A. K.; Wu, X.; Ferreira, J. S.; Kim, M.; Powell, L. R.; Kwon, H.; Groc, L.; Wang, Y.; Cognet, L. Fluorescent Sp3 Defect-Tailored Carbon Nanotubes Enable NIR-II Single Particle Imaging in Live Brain Slices at Ultra-Low Excitation Doses. *Sci. Rep* **2020**, *10*, 5286.
(108) Takeuchi, T.; Iizumi, Y.; Yudasaka, M.; Kizaka-Kondoh, S.; Okazaki, T. Characterization and Biodistribution Analysis of Oxygen-Doped Single-Walled Carbon Nanotubes Used as *in Vivo* Fluorescence Imaging Probes. *Bioconjug Chem.* **2019**, *30*, 1323−1330.
(109) Nagai, Y.; Hamano, R.; Nakamura, K.; Widjaja, I. A.; Tanaka, N.; Zhang, M.; Tanaka, T.; Kataura, H.; Yudasaka, M.; Fujigaya, T. Bright NIR-II Fluorescence from Biocompatible Gel-Coated Carbon Nanotubes for in Vivo Imaging. *Carbon N Y* **2024**, *218*, 118728.
(110) Welsher, K.; Sherlock, S. P.; Dai, H. Deep-Tissue Anatomical Imaging of Mice Using Carbon Nanotube Fluorophores in the Second near-Infrared Window. *Proc. Natl. Acad. Sci. U. S. A.* **2011**, *108*, 8943−8948.
(111) Kofoed Andersen, C.; Khatri, S.; Hansen, J.; Slott, S.; Pavan Parvathaneni, R.; Mendes, A. C.; Chronakis, I. S.; Hung, S.-C.; Rajasekaran, N.; Ma, Z.; Zhu, S.; Dai, H.; Mellins, E. D.; Astakhova, K. Carbon Nanotubes—Potent Carriers for Targeted Drug Delivery in Rheumatoid Arthritis. *Pharmaceutics* **2021**, *13*, 453.
(112) Hong, G.; Diao, S.; Chang, J.; Antaris, A. L.; Chen, C.; Zhang, B.; Zhao, S.; Atochin, D. N.; Huang, P. L.; Andreasson, K. I.; Kuo, C. J.; Dai, H. Through-Skull Fluorescence Imaging of the Brain in a New near-Infrared Window. *Nat. Photonics* **2014**, *8*, 723−730.
(113) Hong, G.; Diao, S.; Antaris, A. L.; Dai, H. Carbon Nanomaterials for Biological Imaging and Nanomedicinal Therapy. *Chem. Rev.* **2015**, *115*, 10816−10906.
(114) Yang, H.; Li, R.; Zhang, Y.; Yu, M.; Wang, Z.; Liu, X.; You, W.; Tu, D.; Sun, Z.; Zhang, R.; Chen, X.; Wang, Q. Colloidal Alloyed Quantum Dots with Enhanced Photoluminescence Quantum Yield in the NIR-II Window. *J. Am. Chem. Soc.* **2021**, *143*, 2601−2607.
(115) Li, B.; Wang, G.; Tong, Y.; Zhang, Y.; Sun, S.-K.; Yu, C. Noninvasive Gastrointestinal Tract Imaging Using BSA-Ag_2Te Quantum Dots as a CT/NIR-II Fluorescence Dual-Modal Imaging Probe in Vivo. *ACS Biomater Sci. Eng.* **2023**, *9*, 449−457.
(116) Li, Y.; Zhang, P.; Tang, W.; McHugh, K. J.; Kershaw, S. V.; Jiao, M.; Huang, X.; Kalytchuk, S.; Perkinson, C. F.; Yue, S.; Qiao, Y.; Zhu, L.; Jing, L.; Gao, M.; Han, B. Bright, Magnetic NIR-II Quantum Dot Probe for Sensitive Dual-Modality Imaging and Intensive Combination Therapy of Cancer. *ACS Nano* **2022**, *16*, 8076−8094.
(117) Yang, L.-L.; Zhao, W.; Liu, Z.-Y.; Ren, M.; Kong, J.; Zong, X.; Luo, M.-Y.; Tang, B.; Xie, J.; Pang, D.-W.; Liu, A.-A. Acid-Resistant Near-Infrared II Ag_2Se Quantum Dots for Gastrointestinal Imaging. *Anal. Chem.* **2023**, *95*, 15540−15548.
(118) Jeong, S.; Jung, Y.; Bok, S.; Ryu, Y.; Lee, S.; Kim, Y.; Song, J.; Kim, M.; Kim, S.; Ahn, G.; Kim, S. Multiplexed In Vivo Imaging Using Size-Controlled Quantum Dots in the Second Near-Infrared Window. *Adv. Healthc Mater.* **2018**, *7*, 1800695.
(119) Wang, P.; Li, J.; Wei, M.; Yang, R.; Lou, K.; Dang, Y.; Sun, W.; Xue, F.; Liu, X. Tumor-Microenvironment Triggered Signal-to-Noise Boosting Nanoprobes for NIR-IIb Fluorescence Imaging Guided Tumor Surgery and NIR-II Photothermal Therapy. *Biomaterials* **2022**, *287*, 121636.
(120) Zhang, J.; Lin, Y.; Zhou, H.; He, H.; Ma, J.; Luo, M.; Zhang, Z.; Pang, D. Cell Membrane-Camouflaged NIR II Fluorescent Ag_2Te Quantum Dots-Based Nanobioprobes for Enhanced In Vivo Homotypic Tumor Imaging. *Adv. Healthc Mater.* **2019**, *8*, 1900341.
(121) Awasthi, P.; An, X.; Xiang, J.; Kalva, N.; Shen, Y.; Li, C. Facile Synthesis of Noncytotoxic PEGylated Dendrimer Encapsulated Silver Sulfide Quantum Dots for NIR-II Biological Imaging. *Nanoscale* **2020**, *12*, 5678−5684.
(122) Qu, S.; Jia, Q.; Li, Z.; Wang, Z.; Shang, L. Chiral NIR-II Fluorescent Ag2S Quantum Dots with Stereospecific Biological Interactions and Tumor Accumulation Behaviors. *Sci. Bull. (Beijing)* **2022**, *67*, 1274−1283.
(123) Yang, L.; Yuan, M.; Ma, P.; Chen, X.; Cheng, Z.; Lin, J. Assembling AgAuSe Quantum Dots with Peptidoglycan and Neutrophils to Realize Enhanced Tumor Targeting, NIR (II) Imaging, and Sonodynamic Therapy. *Small Methods* **2023**, *7*, 2201706.
(124) Chen, L.; Zhao, L.; Wang, Z.; Liu, S.; Pang, D. Near-Infrared-II Quantum Dots for In Vivo Imaging and Cancer Therapy. *Small* **2022**, *18*, 2104567.

https://doi.org/10.1021/acs.chemrev.4c00835
Chem. Rev. 2025, 125, 5195−5227

(125) Wang, F.; Ren, F.; Ma, Z.; Qu, L.; Gourgues, R.; Xu, C.; Baghdasaryan, A.; Li, J.; Zadeh, I. E.; Los, J. W. N.; Fognini, A.; Qin-Dregely, J.; Dai, H. In Vivo Non-Invasive Confocal Fluorescence Imaging beyond 1,700 Nm Using Superconducting Nanowire Single-Photon Detectors. *Nat. Nanotechnol* **2022**, *17*, 653−660.
(126) Zhong, Y.; Dai, H. A Mini-Review on Rare-Earth down-Conversion Nanoparticles for NIR-II Imaging of Biological Systems. *Nano Res.* **2020**, *13*, 1281−1294.
(127) Fang, Z.; Wang, C.; Yang, J.; Song, Z.; Xie, C.; Ji, Y.; Wang, Z.; Du, X.; Zheng, Q.; Chen, C.; Hu, Z.; Zhong, Y. Oxyhaemoglobin Saturation NIR-IIb Imaging for Assessing Cancer Metabolism and Predicting the Response to Immunotherapy. *Nat. Nanotechnol* **2024**, *19*, 124−130.
(128) Ren, F.; Wang, F.; Baghdasaryan, A.; Li, Y.; Liu, H.; Hsu, R.; Wang, C.; Li, J.; Zhong, Y.; Salazar, F.; Xu, C.; Jiang, Y.; Ma, Z.; Zhu, G.; Zhao, X.; Wong, K. K.; Willis, R.; Christopher Garcia, K.; Wu, A.; Mellins, E.; Dai, H. Shortwave-Infrared-Light-Emitting Probes for the in Vivo Tracking of Cancer Vaccines and the Elicited Immune Responses. *Nat. Biomed Eng.* **2024**, *8*, 726−739.
(129) Wang, F.; Qu, L.; Ren, F.; Baghdasaryan, A.; Jiang, Y.; Hsu, R.; Liang, P.; Li, J.; Zhu, G.; Ma, Z.; Dai, H. High-Precision Tumor Resection down to Few-Cell Level Guided by NIR-IIb Molecular Fluorescence Imaging. *Proc. Natl. Acad. Sci. U. S. A.* **2022**, *119*, No. e2123111119.
(130) Ge, X.; Wei, R.; Sun, L. Lanthanide Nanoparticles with Efficient Near-Infrared-II Emission for Biological Applications. *J. Mater. Chem. B* **2020**, *8*, 10257−10270.
(131) Su, Y.; Yu, B.; Wang, S.; Cong, H.; Shen, Y. NIR-II Bioimaging of Small Organic Molecule. *Biomaterials* **2021**, *271*, 120717.
(132) Zhou, H.; Ren, T. Recent Progress of Cyanine Fluorophores for NIR-II Sensing and Imaging. *Chem. Asian J.* **2022**, *17*, No. e202200147.
(133) Jiang, Z.; Ding, Y.; Lovell, J. F.; Zhang, Y. Design and Application of Organic Contrast Agents for Molecular Imaging in the Second near Infrared (NIR-II) Window. *Photoacoustics* **2022**, *28*, 100426.
(134) Li, C.; Guan, X.; Zhang, X.; Zhou, D.; Son, S.; Xu, Y.; Deng, M.; Guo, Z.; Sun, Y.; Kim, J. S. NIR-II Bioimaging of Small Molecule Fluorophores: From Basic Research to Clinical Applications. *Biosens Bioelectron* **2022**, *216*, 114620.
(135) Dang, H.; Yan, L. Organic Fluorescent Nanoparticles with NIR-II Emission for Bioimaging and Therapy. *Biomedical Materials* **2021**, *16*, 022001.
(136) Mu, J.; Xiao, M.; Shi, Y.; Geng, X.; Li, H.; Yin, Y.; Chen, X. The Chemistry of Organic Contrast Agents in the NIR-II Window. *Angew. Chem., Int. Ed.* **2022**, *61*, No. e202114722.
(137) Zhang, X.; Li, S.; Ma, H.; Wang, H.; Zhang, R.; Zhang, X.-D. Activatable NIR-II Organic Fluorescent Probes for Bioimaging. *Theranostics* **2022**, *12*, 3345−3371.
(138) Zhu, S.; Tian, R.; Antaris, A. L.; Chen, X.; Dai, H. Near-Infrared-II Molecular Dyes for Cancer Imaging and Surgery. *Adv. Mater.* **2019**, *31*, 1900321.
(139) Wei, Q.; Xu, D.; Li, T.; He, X.; Wang, J.; Zhao, Y.; Chen, L. Recent Advances of NIR-II Emissive Semiconducting Polymer Dots for In Vivo Tumor Fluorescence Imaging and Theranostics. *Biosensors (Basel)* **2022**, *12*, 1126.
(140) Verma, M.; Chan, Y.-H.; Saha, S.; Liu, M.-H. Recent Developments in Semiconducting Polymer Dots for Analytical Detection and NIR-II Fluorescence Imaging. *ACS Appl. Bio Mater.* **2021**, *4*, 2142−2159.
(141) Gupta, N.; Chan, Y.; Saha, S.; Liu, M. Near-Infrared-II Semiconducting Polymer Dots for Deep-tissue Fluorescence Imaging. *Chem. Asian J.* **2021**, *16*, 175−184.
(142) Liu, Y.; Liu, J.; Chen, D.; Wang, X.; Zhang, Z.; Yang, Y.; Jiang, L.; Qi, W.; Ye, Z.; He, S.; Liu, Q.; Xi, L.; Zou, Y.; Wu, C. Fluorination Enhances NIR-II Fluorescence of Polymer Dots for Quantitative Brain Tumor Imaging. *Angew. Chem., Int. Ed.* **2020**, *59*, 21049−21057.
(143) Li, Y.; Su, S.; Yang, C.; Liu, M.; Lo, P.; Chen, Y.; Hsu, C.; Lee, Y.; Chiang, H. K.; Chan, Y. Molecular Design of Ultrabright Semiconducting Polymer Dots with High NIR-II Fluorescence for 3D Tumor Mapping. *Adv. Healthc Mater.* **2021**, *10*, 2100993.
(144) Liu, M.; Zhang, Z.; Yang, Y.; Chan, Y. Polymethine-Based Semiconducting Polymer Dots with Narrow-Band Emission and Absorption/Emission Maxima at NIR-II for Bioimaging. *Angew. Chem., Int. Ed.* **2021**, *60*, 983−989.
(145) Zhang, Z.; Fang, X.; Liu, Z.; Liu, H.; Chen, D.; He, S.; Zheng, J.; Yang, B.; Qin, W.; Zhang, X.; Wu, C. Semiconducting Polymer Dots with Dual-Enhanced NIR-IIa Fluorescence for Through-Skull Mouse-Brain Imaging. *Angew. Chem.* **2020**, *132*, 3720−3727.
(146) Zhou, X.; Liu, Q.; Yuan, W.; Li, Z.; Xu, Y.; Feng, W.; Xu, C.; Li, F. Ultrabright NIR-II Emissive Polymer Dots for Metastatic Ovarian Cancer Detection. *Advanced Science* **2021**, *8*, 2000441.
(147) Fang, L.; Ai, R.; Wang, W.; Tan, L.; Li, C.; Wang, D.; Jiang, R.; Qiu, F.; Qi, L.; Yang, J.; Zhou, W.; Zhu, T.; Tan, W.; Jiang, Y.; Fang, X. Hyperbranched Polymer Dots with Strong Absorption and High Fluorescence Quantum Yield for In Vivo NIR-II Imaging. *Nano Lett.* **2023**, *23*, 8734−8742.
(148) Hsu, K.-F.; Su, S.-P.; Lu, H.-F.; Liu, M.-H.; Chang, Y. J.; Lee, Y.-J.; Chiang, H. K.; Hsu, C.-P.; Lu, C.-W.; Chan, Y.-H. TADF-Based NIR-II Semiconducting Polymer Dots for *in Vivo* 3D Bone Imaging. *Chem. Sci.* **2022**, *13*, 10074−10081.
(149) Jiang, Y.; Zhu, L.; Wu, W. Theranostic Nanoprobes with Aggregation-Induced NIR-II Emission: From Molecular Design to Biomedical Application. *ChemBioChem.* **2023**, *24*, No. e202200777.
(150) Yin, S.; Song, J.; Liu, D.; Wang, K.; Qi, J. NIR-II AIEgens with Photodynamic Effect for Advanced Theranostics. *Molecules* **2022**, *27*, 6649.
(151) Shi, T.; Huang, C.; Li, Y.; Huang, F.; Yin, S. NIR-II Phototherapy Agents with Aggregation-Induced Emission Characteristics for Tumor Imaging and Therapy. *Biomaterials* **2022**, *285*, 121535.
(152) Fan, X.; Xia, Q.; Zhang, Y.; Li, Y.; Feng, Z.; Zhou, J.; Qi, J.; Tang, B. Z.; Qian, J.; Lin, H. Aggregation-Induced Emission (AIE) Nanoparticles-Assisted NIR-II Fluorescence Imaging-Guided Diagnosis and Surgery for Inflammatory Bowel Disease (IBD). *Adv. Healthc Mater.* **2021**, *10*, 2101043.
(153) Xu, R.; Jiao, D.; Long, Q.; Li, X.; Shan, K.; Kong, X.; Ou, H.; Ding, D.; Tang, Q. Highly Bright Aggregation-Induced Emission Nanodots for Precise Photoacoustic/NIR-II Fluorescence Imaging-Guided Resection of Neuroendocrine Neoplasms and Sentinel Lymph Nodes. *Biomaterials* **2022**, *289*, 121780.
(154) Qu, Q.; Zhang, Z.; Guo, X.; Yang, J.; Cao, C.; Li, C.; Zhang, H.; Xu, P.; Hu, Z.; Tian, J. Novel Multifunctional NIR-II Aggregation-Induced Emission Nanoparticles-Assisted Intraoperative Identification and Elimination of Residual Tumor. *J. Nanobiotechnology* **2022**, *20*, 143.
(155) Li, Y.; Hu, D.; Sheng, Z.; Min, T.; Zha, M.; Ni, J.-S.; Zheng, H.; Li, K. Self-Assembled AIEgen Nanoparticles for Multiscale NIR-II Vascular Imaging. *Biomaterials* **2021**, *264*, 120365.
(156) Lin, J.; Zeng, X.; Xiao, Y.; Tang, L.; Nong, J.; Liu, Y.; Zhou, H.; Ding, B.; Xu, F.; Tong, H.; Deng, Z.; Hong, X. Novel Near-Infrared II Aggregation-Induced Emission Dots for *in Vivo* Bioimaging. *Chem. Sci.* **2019**, *10*, 1219−1226.
(157) Wu, W.; Yang, Y.; Yang, Y.; Yang, Y.; Zhang, K.; Guo, L.; Ge, H.; Chen, X.; Liu, J.; Feng, H. Molecular Engineering of an Organic NIR-II Fluorophore with Aggregation-Induced Emission Characteristics for In Vivo Imaging. *Small* **2019**, *15*, 1805549.
(158) Wang, J.; Liu, Y.; Morsch, M.; Lu, Y.; Shangguan, P.; Han, L.; Wang, Z.; Chen, X.; Song, C.; Liu, S.; Shi, B.; Tang, B. Z. Brain-Targeted Aggregation-Induced-Emission Nanoparticles with Near-Infrared Imaging at 1550 Nm Boosts Orthotopic Glioblastoma Theranostics. *Adv. Mater.* **2022**, *34*, 2106082.
(159) Wan, H.; Yue, J.; Zhu, S.; Uno, T.; Zhang, X.; Yang, Q.; Yu, K.; Hong, G.; Wang, J.; Li, L.; Ma, Z.; Gao, H.; Zhong, Y.; Su, J.; Antaris, A. L.; Xia, Y.; Luo, J.; Liang, Y.; Dai, H. A Bright Organic NIR-II Nanofluorophore for Three-Dimensional Imaging into Biological Tissues. *Nat. Commun.* **2018**, *9*, 1171.
(160) Yu, M.; Xu, J.; Zheng, J. Renal Clearable Luminescent Gold Nanoparticles: From the Bench to the Clinic. *Angew. Chem.* **2019**, *131*, 4156−4172.

https://doi.org/10.1021/acs.chemrev.4c00835
Chem. Rev. 2025, 125, 5195−5227

(161) van de Looij, S. M.; Hebels, E. R.; Viola, M.; Hembury, M.; Oliveira, S.; Vermonden, T. Gold Nanoclusters: Imaging, Therapy, and Theranostic Roles in Biomedical Applications. *Bioconjug Chem.* **2022**, *33*, 4−23.
(162) Moreels, I.; Lambert, K.; Smeets, D.; De Muynck, D.; Nollet, T.; Martins, J. C.; Vanhaecke, F.; Vantomme, A.; Delerue, C.; Allan, G.; Hens, Z. Size-Dependent Optical Properties of Colloidal PbS Quantum Dots. *ACS Nano* **2009**, *3*, 3023−3030.
(163) Qin, N.; Han, H.; Guan, G.; Han, M.-Y. Structurally Altered Size, Composition, Shape and Interface-Dependent Optical Properties of Quantized Nanomaterials. *Nano Res.* **2024**, *17*, 10543−10569.
(164) Lu, H.; Carroll, G. M.; Neale, N. R.; Beard, M. C. Infrared Quantum Dots: Progress, Challenges, and Opportunities. *ACS Nano* **2019**, *13*, 939−953.
(165) Saito, R.; Dresselhaus, G.; Dresselhaus, M. S. Trigonal Warping Effect of Carbon Nanotubes. *Phys. Rev. B* **2000**, *61*, 2981−2990.
(166) Bachilo, S. M.; Strano, M. S.; Kittrell, C.; Hauge, R. H.; Smalley, R. E.; Weisman, R. B. Structure-Assigned Optical Spectra of Single-Walled Carbon Nanotubes. *Science* **2002**, *298*, 2361−2366.
(167) Ma, Y.-Z.; Valkunas, L.; Bachilo, S. M.; Fleming, G. R. Exciton Binding Energy in Semiconducting Single-Walled Carbon Nanotubes. *J. Phys. Chem. B* **2005**, *109*, 15671−15674.
(168) Hertel, T.; Perebeinos, V.; Crochet, J.; Arnold, K.; Kappes, M.; Avouris, P. Intersubband Decay of 1-D Exciton Resonances in Carbon Nanotubes. *Nano Lett.* **2008**, *8*, 87−91.
(169) Du, Y.; Liu, X.; Zhu, S. Near-Infrared-II Cyanine/Polymethine Dyes, Current State and Perspective. *Front Chem.* **2021**, *9*, 718709.
(170) Ji, A.; Lou, H.; Qu, C.; Lu, W.; Hao, Y.; Li, J.; Wu, Y.; Chang, T.; Chen, H.; Cheng, Z. Acceptor Engineering for NIR-II Dyes with High Photochemical and Biomedical Performance. *Nat. Commun.* **2022**, *13*, 3815.
(171) Zhu, S.; Yung, B. C.; Chandra, S.; Niu, G.; Antaris, A. L.; Chen, X. Near-Infrared-II (NIR-II) Bioimaging *via* Off-Peak NIR-I Fluorescence Emission. *Theranostics* **2018**, *8*, 4141−4151.
(172) Mooradian, A. Photoluminescence of Metals. *Phys. Rev. Lett.* **1969**, *22*, 185−187.
(173) Kang, X.; Zhu, M. Tailoring the Photoluminescence of Atomically Precise Nanoclusters. *Chem. Soc. Rev.* **2019**, *48*, 2422−2457.
(174) Liu, Z.; Luo, L.; Jin, R. Visible to NIR-II Photoluminescence of Atomically Precise Gold Nanoclusters. *Adv. Mater.* **2024**, *36*, 2309073.
(175) Weerawardene, K. L. D. M.; Aikens, C. M. Theoretical Insights into the Origin of Photoluminescence of Au 25 (SR) 18 - Nanoparticles. *J. Am. Chem. Soc.* **2016**, *138*, 11202−11210.
(176) Zheng, J.; Nicovich, P. R.; Dickson, R. M. Highly Fluorescent Noble-Metal Quantum Dots. *Annu. Rev. Phys. Chem.* **2007**, *58*, 409−431.
(177) Yang, T.-Q.; Peng, B.; Shan, B.-Q.; Zong, Y.-X.; Jiang, J.-G.; Wu, P.; Zhang, K. Origin of the Photoluminescence of Metal Nanoclusters: From Metal-Centered Emission to Ligand-Centered Emission. *Nanomaterials* **2020**, *10*, 261.
(178) Krishnadas, K. R.; Sementa, L.; Medves, M.; Fortunelli, A.; Stener, M.; Fürstenberg, A.; Longhi, G.; Bürgi, T. Chiral Functionalization of an Atomically Precise Noble Metal Cluster: Insights into the Origin of Chirality and Photoluminescence. *ACS Nano* **2020**, *14*, 9687−9700.
(179) Pniakowska, A.; Kumaranchira Ramankutty, K.; Obstarczyk, P.; PerićBakulić, M.; Sanader Maršić, Ž.; Bonačić-Koutecký, V.; Bürgi, T.; Olesiak-Bańska, J. Gold-Doping Effect on Two-Photon Absorption and Luminescence of Atomically Precise Silver Ligated Nanoclusters. *Angew. Chem., Int. Ed.* **2022**, *61*, No. e202209645.
(180) Musnier, B.; Wegner, K. D.; Comby-Zerbino, C.; Trouillet, V.; Jourdan, M.; Häusler, I.; Antoine, R.; Coll, J.-L.; Resch-Genger, U.; Le Guével, X. High Photoluminescence of Shortwave Infrared-Emitting Anisotropic Surface Charged Gold Nanoclusters. *Nanoscale* **2019**, *11*, 12092−12096.
(181) Pramanik, G.; Humpolickova, J.; Valenta, J.; Kundu, P.; Bals, S.; Bour, P.; Dracinsky, M.; Cigler, P. Gold Nanoclusters with Bright Near-Infrared Photoluminescence. *Nanoscale* **2018**, *10*, 3792−3798.
(182) Le Guével, X.; Wegner, K. D.; Würth, C.; Baulin, V. A.; Musnier, B.; Josserand, V.; Resch-Genger, U.; Coll, J. Tailoring the SWIR Emission of Gold Nanoclusters by Surface Ligand Rigidification and Their Application in 3D Bioimaging. *Chem. Commun.* **2022**, *58*, 2967−2970.
(183) Guo, M.; Zhang, G.; Zhao, R.; Ma, H.; Yan, Y.; Yang, S.; Meng, J.; Huang, Y.; Zhang, X.-D.; Wang, H.; Zhang, R. Ligand Engineering of Gold Nanoclusters for NIR-II Imaging. *ACS Appl. Nano Mater.* **2023**, *6*, 15945−15958.
(184) Chen, Y.; Montana, D. M.; Wei, H.; Cordero, J. M.; Schneider, M.; Le Guével, X.; Chen, O.; Bruns, O. T.; Bawendi, M. G. Shortwave Infrared in Vivo Imaging with Gold Nanoclusters. *Nano Lett.* **2017**, *17*, 6330−6334.
(185) Pyo, K.; Thanthirige, V. D.; Kwak, K.; Pandurangan, P.; Ramakrishna, G.; Lee, D. Ultrabright Luminescence from Gold Nanoclusters: Rigidifying the Au(I)-Thiolate Shell. *J. Am. Chem. Soc.* **2015**, *137*, 8244−8250.
(186) Yi, S.; Hu, Q.; Chi, Y.; Qu, H.; Xiao, Y. Bright and Renal-Clearable Au Nanoclusters with NIR-II Excitation and Emission for High-Resolution Fluorescence Imaging of Kidney Dysfunction. *ACS Mater. Lett.* **2023**, *5*, 2164−2173.
(187) Deng, H.; Huang, K.; Xiu, L.; Sun, W.; Yao, Q.; Fang, X.; Huang, X.; Noreldeen, H. A. A.; Peng, H.; Xie, J.; Chen, W. Bis-Schiff Base Linkage-Triggered Highly Bright Luminescence of Gold Nanoclusters in Aqueous Solution at the Single-Cluster Level. *Nat. Commun.* **2022**, *13*, 3381.
(188) Zheng, J.; Zhang, C.; Dickson, R. M. Highly Fluorescent, Water-Soluble, Size-Tunable Gold Quantum Dots. *Phys. Rev. Lett.* **2004**, *93*, 077402.
(189) Huang, Y.; Chen, K.; Liu, L.; Ma, H.; Zhang, X.; Tan, K.; Li, Y.; Liu, Y.; Liu, C.; Wang, H.; Zhang, X. Single Atom-Engineered NIR-II Gold Clusters with Ultrahigh Brightness and Stability for Acute Kidney Injury. *Small* **2023**, *19*, 2300145.
(190) Wang, S.; Meng, X.; Das, A.; Li, T.; Song, Y.; Cao, T.; Zhu, X.; Zhu, M.; Jin, R. A 200-fold Quantum Yield Boost in the Photoluminescence of Silver-Doped Ag_xAu_{25-x} Nanoclusters: The 13 Th Silver Atom Matters. *Angew. Chem., Int. Ed.* **2014**, *53*, 2376−2380.
(191) Haye, L.; Diriwari, P. I.; Alhalabi, A.; Gallavardin, T.; Combes, A.; Klymchenko, A. S.; Hildebrandt, N.; Le Guével, X.; Reisch, A. Enhancing Near Infrared II Emission of Gold Nanoclusters via Encapsulation in Small Polymer Nanoparticles. *Adv. Opt Mater.* **2023**, *11*, 2201474.
(192) Tang, B.; Xia, W.; Cai, W.; Liu, J. Luminescent Gold Nanoparticles with Controllable Hydrophobic Interactions. *Nano Lett.* **2022**, *22*, 8109−8114.
(193) Li, Q.; Zeman, C. J.; Schatz, G. C.; Gu, X. W. Source of Bright Near-Infrared Luminescence in Gold Nanoclusters. *ACS Nano* **2021**, *15*, 16095−16105.
(194) Li, Q.; Zeman, C. J.; Ma, Z.; Schatz, G. C.; Gu, X. W. Bright NIR-II Photoluminescence in Rod-Shaped Icosahedral Gold Nanoclusters. *Small* **2021**, *17*, 2007992.
(195) Zhang, B.; Liu, Z.; Zhang, R.; Yao, Q.; Xie, J. Precision Metal Nanoclusters Meet Proteins: Crafting Next-Gen Hybrid Materials. *ACS Nano* **2025**, *19*, 3997−4010.
(196) Zhang, W.; Shi, Y.; Zhang, J.; Shi, G.; Qiao, X.; He, Y.; Lam, J. W. Y.; Zhao, Z.; Xie, J.; Pang, X.; Tang, B. Z. Precision Synthesis of Ultrastable Hydrophilic Metal Nanocluster Assemblies. *Macromolecules* **2024**, *57*, 4556−4566.
(197) Song, X.; Wei, J.; Cai, X.; Liu, Y.; Wu, F.; Tong, S.; Li, S.; Yao, Q.; Xie, J.; Yang, H. Organotropic Engineering of Luminescent Gold Nanoclusters for In Vivo Imaging of Lung Orthotopic Tumors. *ACS Nano* **2024**, *18*, 33555−33565.
(198) Zhang, B.; Matus, M. F.; Yao, Q.; Song, X.; Wu, Z.; Hu, W.; Häkkinen, H.; Xie, J. Unraveling the Stoichiometric Interactions and Synergism between Ligand-Protected Gold Nanoparticles and Proteins. *J. Am. Chem. Soc.* **2025**, *147*, 6404−6414.
(199) Luo, L.; Liu, Z.; Kong, J.; Gianopoulos, C. G.; Coburn, I.; Kirschbaum, K.; Zhou, M.; Jin, R. Three-Atom-Wide Gold Quantum

Rods with Periodic Elongation and Strongly Polarized Excitons. *Proc. Natl. Acad. Sci. U. S. A.* **2024**, *121*, No. e2318537121.
(200) Li, Y.; Song, Y.; Zhang, X.; Liu, T.; Xu, T.; Wang, H.; Jiang, D.; Jin, R. Atomically Precise Au $_{42}$ Nanorods with Longitudinal Excitons for an Intense Photothermal Effect. *J. Am. Chem. Soc.* **2022**, *144*, 12381−12389.
(201) Baghdasaryan, A.; Liu, H.; Ren, F.; Hsu, R.; Jiang, Y.; Wang, F.; Zhang, M.; Grigoryan, L.; Dai, H. Intratumor Injected Gold Molecular Clusters for NIR-II Imaging and Cancer Therapy. *Proc. Natl. Acad. Sci. U. S. A.* **2024**, *121*, No. e2318265121.
(202) Suyama, M.; Takano, S.; Tsukuda, T. Synergistic Effects of Pt and Cd Codoping to Icosahedral **Au** $_{13}$ Superatoms. *J. Phys. Chem. C* **2020**, *124*, 23923−23929.
(203) Liu, H.; Hong, G.; Luo, Z.; Chen, J.; Chang, J.; Gong, M.; He, H.; Yang, J.; Yuan, X.; Li, L.; Mu, X.; Wang, J.; Mi, W.; Luo, J.; Xie, J.; Zhang, X. D. Atomic-Precision Gold Clusters for NIR-II Imaging. *Adv. Mater.* **2019**, *31*, 1901015.
(204) Zhu, M.; Eckenhoff, W. T.; Pintauer, T.; Jin, R. Conversion of Anionic [Au 25 (SCH 2 CH 2 Ph) 18] - Cluster to Charge Neutral Cluster via Air Oxidation. *J. Phys. Chem. C* **2008**, *112*, 14221−14224.
(205) Nienhaus, K.; Wang, H.; Nienhaus, G. U. Nanoparticles for Biomedical Applications: Exploring and Exploiting Molecular Interactions at the Nano-Bio Interface. *Mater. Today Adv.* **2020**, *5*, 100036.
(206) Zhu, Z.-J.; Yeh, Y.-C.; Tang, R.; Yan, B.; Tamayo, J.; Vachet, R. W.; Rotello, V. M. Stability of Quantum Dots in Live Cells. *Nat. Chem.* **2011**, *3*, 963−968.
(207) Nienhaus, K.; Nienhaus, G. U. Mechanistic Understanding of Protein Corona Formation around Nanoparticles: Old Puzzles and New Insights. *Small* **2023**, *19*, 2301663.
(208) Mutas, M.; Strelow, C.; Kipp, T.; Mews, A. Specific Binding and Internalization: An Investigation of Fluorescent Aptamer-Gold Nanoclusters and Cells with Fluorescence Lifetime Imaging Microscopy. *Nanoscale* **2018**, *10*, 20453−20461.
(209) Shang, L.; Yang, L.; Wang, H.; Nienhaus, G. U. In Situ Monitoring of the Intracellular Stability of Nanoparticles by Using Fluorescence Lifetime Imaging. *Small* **2016**, *12*, 868−873.
(210) Yu, Z.; Musnier, B.; Wegner, K. D.; Henry, M.; Chovelon, B.; Desroches-Castan, A.; Fertin, A.; Resch-Genger, U.; Bailly, S.; Coll, J.-L.; Usson, Y.; Josserand, V.; Le Guével, X. High-Resolution Shortwave Infrared Imaging of Vascular Disorders Using Gold Nanoclusters. *ACS Nano* **2020**, *14*, 4973−4981.
(211) Liu, P.; Shi, T.; Li, H.; Chen, H.; Huang, Y.; Ma, H.; Zhu, T.; Zhao, R.; Li, Y.; Xin, Q.; Liu, L.; Sun, S.; Nie, H.; Long, W.; Wang, H.; Wang, J.; Zhang, X.-D.; Ming, D. Airy Beam Assisted NIR-II Light-Sheet Microscopy. *Nano Today* **2022**, *47*, 101628.
(212) Zhao, Z.; Chen, H.; He, K.; Lin, J.; Cai, W.; Sun, Y.; Liu, J. Glutathione-Activated Emission of Ultrasmall Gold Nanoparticles in the Second Near-Infrared Window for Imaging of Early Kidney Injury. *Anal. Chem.* **2023**, *95*, 5061−5068.
(213) Li, S.; Yang, N.; Ma, Q.; Li, S.; Tong, S.; Luo, J.; Song, X.; Yang, H. Tailoring Oxidation Responsiveness of Gold Nanoclusters via Ligand Engineering for Imaging Acute Kidney Injury. *Anal. Chem.* **2023**, *95*, 16153−16159.
(214) Zhao, Z.; He, K.; Liu, B.; Nie, W.; Luo, X.; Liu, J. Intrarenal PH-Responsive Self-Assembly of Luminescent Gold Nanoparticles for Diagnosis of Early Kidney Injury. *Angew. Chem., Int. Ed.* **2024**, *63*, No. e202406016.
(215) Tan, Y.; Cai, W.; Luo, C.; Tang, J.; Kwok, R. T. K.; Lam, J. W. Y.; Sun, J.; Liu, J.; Tang, B. Z. Rapid Biotransformation of Luminescent Bimetallic Nanoparticles in Hepatic Sinusoids. *J. Am. Chem. Soc.* **2022**, *144*, 20653−20660.
(216) Li, S.; Ma, Q.; Wang, C.; Yang, K.; Hong, Z.; Chen, Q.; Song, J.; Song, X.; Yang, H. Near-Infrared II Gold Nanocluster Assemblies with Improved Luminescence and Biofate for In Vivo Ratiometric Imaging of H $_2$ S. *Anal. Chem.* **2022**, *94*, 2641−2647.
(217) Zhou, K.; Cai, W.; Tan, Y.; Zhao, Z.; Liu, J. Highly Controllable Nanoassemblies of Luminescent Gold Nanoparticles with Abnormal Disassembly-Induced Emission Enhancement for In Vivo Imaging Applications. *Angew. Chem., Int. Ed.* **2022**, *61*, No. e202212214.
(218) Wang, W.; Kong, Y.; Jiang, J.; Xie, Q.; Huang, Y.; Li, G.; Wu, D.; Zheng, H.; Gao, M.; Xu, S.; Pan, Y.; Li, W.; Ma, R.; Wu, M. X.; Li, X.; Zuilhof, H.; Cai, X.; Li, R. Engineering the Protein Corona Structure on Gold Nanoclusters Enables Red-Shifted Emissions in the Second Near-infrared Window for Gastrointestinal Imaging. *Angew. Chem., Int. Ed.* **2020**, *59*, 22431−22435.
(219) Wang, X.; Jiao, M.; Tian, F.; Lu, X.; Xiong, H.; Liu, F.; Wan, Y.; Zhang, X.; Wan, H. A Biomimetic Nanoplatform with Improved Inflammatory Targeting Behavior for ROS Scavenging-Based Treatment of Ulcerative Colitis. *Adv. Healthc Mater.* **2023**, *12*, 2301450.
(220) Liang, M.; Hu, Q.; Yi, S.; Chi, Y.; Xiao, Y. Development of an Au Nanoclusters Based Activatable Nanoprobe for NIR-II Fluorescence Imaging of Gastric Acid. *Biosens Bioelectron* **2023**, *224*, 115062.
(221) Li, D.; Liu, Q.; Qi, Q.; Shi, H.; Hsu, E. C.; Chen, W.; Yuan, W.; Wu, Y.; Lin, S.; Zeng, Y.; Xiao, Z.; Xu, L.; Zhang, Y.; Stoyanova, T.; Jia, W.; Cheng, Z. Gold Nanoclusters for NIR-II Fluorescence Imaging of Bones. *Small* **2020**, *16*, 2003851.
(222) Yang, G.; Liu, K.; Wang, Y.; Pan, X.; Ye, J.; Li, Y.; Du, F.; Feng, T.; Yuan, X. Phosphorylation of NIR-II Emitting Au Nanoclusters for Targeted Bone Imaging and Improved Rheumatoid Arthritis Therapy. *Aggregate* **2024**, *5*, No. e435.
(223) Song, X.; Zhu, W.; Ge, X.; Li, R.; Li, S.; Chen, X.; Song, J.; Xie, J.; Chen, X.; Yang, H. A New Class of NIR-II Gold Nanocluster-Based Protein Biolabels for In Vivo Tumor-Targeted Imaging. *Angew. Chem., Int. Ed.* **2021**, *60*, 1306−1312.
(224) Yang, Y.; Yu, Y.; Chen, H.; Meng, X.; Ma, W.; Yu, M.; Li, Z.; Li, C.; Liu, H.; Zhang, X.; Xiao, H.; Yu, Z. Illuminating Platinum Transportation While Maximizing Therapeutic Efficacy by Gold Nanoclusters *via* Simultaneous Near-Infrared-I/II Imaging and Glutathione Scavenging. *ACS Nano* **2020**, *14*, 13536−13547.
(225) Nie, W.; He, K.; Zhao, Z.; Luo, X.; Liu, J. Luminescent Gold Nanoparticles with Discrete DNA Valences for Precisely Controlled Transport at the Subcellular Level. *Angew. Chem., Int. Ed.* **2023**, *62*, No. e202314896.
(226) Pang, Z.; Yan, W.; Yang, J.; Li, Q.; Guo, Y.; Zhou, D.; Jiang, X. Multifunctional Gold Nanoclusters for Effective Targeting, Near-Infrared Fluorescence Imaging, Diagnosis, and Treatment of Cancer Lymphatic Metastasis. *ACS Nano* **2022**, *16*, 16019−16037.
(227) Tang, L.; Zeng, X.; Zhou, H.; Gui, C.; Luo, Q.; Zhou, W.; Wu, J.; Li, Q.; Li, Y.; Xiao, Y. Theranostic Gold Nanoclusters for NIR-II Imaging and Photodynamic Therapy. *Chem. Res. Chin Univ* **2021**, *37*, 934−942.
(228) Kong, Y.; Santos-Carballal, D.; Martin, D.; Sergeeva, N. N.; Wang, W.; Liu, G.; Johnson, B.; Bhayana, B.; Lin, Z.; Wang, Y.; Le Guével, X.; de Leeuw, N. H.; Zhou, D.; Wu, M. X. A NIR-II-Emitting Gold Nanocluster-Based Drug Delivery System for Smartphone-Triggered Photodynamic Theranostics with Rapid Body Clearance. *Mater. Today* **2021**, *51*, 96−107.
(229) Dan, Q.; Yuan, Z.; Zheng, S.; Ma, H.; Luo, W.; Zhang, L.; Su, N.; Hu, D.; Sheng, Z.; Li, Y. Gold Nanoclusters-Based NIR-II Photosensitizers with Catalase-like Activity for Boosted Photodynamic Therapy. *Pharmaceutics* **2022**, *14*, 1645.
(230) Hu, S.; Huang, L.; Zhou, L.; Wu, T.; Zhao, S.; Zhang, L. Single-Excitation Triple-Emission Down-/Up-Conversion Nanoassemblies for Tumor Microenvironment-Enhanced Ratiometric NIR-II Fluorescence Imaging and Chemo-/Photodynamic Combination Therapy. *Anal. Chem.* **2023**, *95*, 3830−3839.
(231) Zhao, H.; Wang, H.; Li, H.; Zhang, T.; Zhang, J.; Guo, W.; Fu, K.; Du, G. Magnetic and Near-Infrared-II Fluorescence Au-Gd Nanoclusters for Imaging-Guided Sensitization of Tumor Radiotherapy. *Nanoscale Adv.* **2022**, *4*, 1815−1826.
(232) Yu, M.; Ye, Z.; Liu, S.; Zhu, Y.; Niu, X.; Wang, J.; Ao, R.; Huang, H.; Cai, H.; Liu, Y.; Chen, X.; Lin, L. Redox-Active Ferrocene Quencher-Based Supramolecular Nanomedicine for NIR-II Fluorescence-Monitored Chemodynamic Therapy. *Angew. Chem., Int. Ed.* **2024**, *63*, No. e202318155.
(233) Amendola, V.; Pilot, R.; Frasconi, M.; Maragò, O. M.; Iatì, M. A. Surface Plasmon Resonance in Gold Nanoparticles: A Review. *J. Phys.: Condens. Matter* **2017**, *29*, 203002.

https://doi.org/10.1021/acs.chemrev.4c00835
Chem. Rev. 2025, 125, 5195−5227

(234) Kumar, P. P. P.; Lim, D.-K. Photothermal Effect of Gold Nanoparticles as a Nanomedicine for Diagnosis and Therapeutics. *Pharmaceutics* **2023**, *15*, 2349.
(235) Luo, L.; Liu, Z.; Du, X.; Jin, R. Near-Infrared Dual Emission from the Au $_{42}$ (SR) $_{32}$ Nanocluster and Tailoring of Intersystem Crossing. *J. Am. Chem. Soc.* **2022**, *144*, 19243−19247.
(236) Liu, Z.; Li, Y.; Kahng, E.; Xue, S.; Du, X.; Li, S.; Jin, R. Tailoring the Electron-Phonon Interaction in Au $_{25}$ (SR) $_{18}$ Nanoclusters via Ligand Engineering and Insight into Luminescence. *ACS Nano* **2022**, *16*, 18448−18458.
(237) Devadas, M. S.; Thanthirige, V. D.; Bairu, S.; Sinn, E.; Ramakrishna, G. Temperature-Dependent Absorption and Ultrafast Luminescence Dynamics of Bi-Icosahedral Au $_{25}$ Clusters. *J. Phys. Chem. C* **2013**, *117*, 23155−23161.
(238) Gu, W.; Zhou, Y.; Wang, W.; You, Q.; Fan, W.; Zhao, Y.; Bian, G.; Wang, R.; Fang, L.; Yan, N.; Xia, N.; Liao, L.; Wu, Z. Concomitant Near-Infrared Photothermy and Photoluminescence of Rod-Shaped Au $_{52}$ (PET) $_{32}$ and Au $_{66}$ (PET) $_{38}$ Synthesized Concurrently. *Angew. Chem., Int. Ed.* **2024**, *63*, No. e202407518.
(239) Musnier, B.; Henry, M.; Vollaire, J.; Coll, J.; Usson, Y.; Josserand, V.; Le Guével, X. Optimization of Spatial Resolution and Scattering Effects for Biomedical Fluorescence Imaging by Using Subregions of the Shortwave Infrared Spectrum. *J. Biophotonics* **2021**, *14*, No. e202000345.
(240) Mier, W.; Mier, D. Advantages in Functional Imaging of the Brain. *Front. Hum. Neurosci.* **2015**, *9*, 249.
(241) Kim, B.; Kim, H.; Kim, S.; Hwang, Y. A Brief Review of Non-Invasive Brain Imaging Technologies and the near-Infrared Optical Bioimaging. *Appl. Microsc* **2021**, *51*, 9.
(242) Qin, Z.; She, Z.; Chen, C.; Wu, W.; Lau, J. K. Y.; Ip, N. Y.; Qu, J. Y. Deep Tissue Multi-Photon Imaging Using Adaptive Optics with Direct Focus Sensing and Shaping. *Nat. Biotechnol.* **2022**, *40*, 1663−1671.
(243) Wang, F.; Wan, H.; Ma, Z.; Zhong, Y.; Sun, Q.; Tian, Y.; Qu, L.; Du, H.; Zhang, M.; Li, L.; Ma, H.; Luo, J.; Liang, Y.; Li, W. J.; Hong, G.; Liu, L.; Dai, H. Light-Sheet Microscopy in the near-Infrared II Window. *Nat. Methods* **2019**, *16*, 545−552.
(244) Wang, F.; Ma, Z.; Zhong, Y.; Salazar, F.; Xu, C.; Ren, F.; Qu, L.; Wu, A. M.; Dai, H. In Vivo NIR-II Structured-Illumination Light-Sheet Microscopy. *Proc. Natl. Acad. Sci. U. S. A.* **2021**, *118*, No. e2023888118.
(245) Zhang, K.; Chen, F.; Wang, L.; Hu, J. Second Near-Infrared (NIR-II) Window for Imaging-Navigated Modulation of Brain Structure and Function. *Small* **2023**, *19*, 2206044.
(246) Wei, Z.; Liu, Y.; Li, B.; Li, J.; Lu, S.; Xing, X.; Liu, K.; Wang, F.; Zhang, H. Rare-Earth Based Materials: An Effective Toolbox for Brain Imaging, Therapy, Monitoring and Neuromodulation. *Light Sci. Appl.* **2022**, *11*, 175.
(247) Wan, H.; Yue, J.; Zhu, S.; Uno, T.; Zhang, X.; Yang, Q.; Yu, K.; Hong, G.; Wang, J.; Li, L.; Ma, Z.; Gao, H.; Zhong, Y.; Su, J.; Antaris, A. L.; Xia, Y.; Luo, J.; Liang, Y.; Dai, H. A Bright Organic NIR-II Nanofluorophore for Three-Dimensional Imaging into Biological Tissues. *Nat. Commun.* **2018**, *9*, 1171.
(248) Zhang, X. D.; Wang, H.; Antaris, A. L.; Li, L.; Diao, S.; Ma, R.; Nguyen, A.; Hong, G.; Ma, Z.; Wang, J.; Zhu, S.; Castellano, J. M.; Wyss-Coray, T.; Liang, Y.; Luo, J.; Dai, H. Traumatic Brain Injury Imaging in the Second Near-Infrared Window with a Molecular Fluorophore. *Adv. Mater.* **2016**, *28*, 6872−6879.
(249) Ren, F.; Jiang, Z.; Han, M.; Zhang, H.; Yun, B.; Zhu, H.; Li, Z. NIR-II Fluorescence Imaging for Cerebrovascular Diseases. *VIEW* **2021**, *2*, 20200128.
(250) Xie, N.; Hou, Y.; Wang, S.; Ai, X.; Bai, J.; Lai, X.; Zhang, Y.; Meng, X.; Wang, X. Second Near-Infrared (NIR-II) Imaging: A Novel Diagnostic Technique for Brain Diseases. *Rev. Neurosci* **2022**, *33*, 467−490.
(251) Werner, R. A.; Pomper, M. G.; Buck, A. K.; Rowe, S. P.; Higuchi, T. SPECT and PET Radiotracers in Renal Imaging. *Semin Nucl. Med.* **2022**, *52*, 406−418.
(252) Liu, P.; Johnson, S. E.; Xie, X.; Gao, L.; Haney, C. R.; Zhao, M.; Jin, J. Targeted Design of a Recombinant Tracer for SPECT Renal Imaging. *Theranostics* **2021**, *11*, 9118−9132.
(253) Werner, R. A.; Chen, X.; Lapa, C.; Koshino, K.; Rowe, S. P.; Pomper, M. G.; Javadi, M. S.; Higuchi, T. The next Era of Renal Radionuclide Imaging: Novel PET Radiotracers. *Eur. J. Nucl. Med. Mol. Imaging* **2019**, *46*, 1773−1786.
(254) Nikken, J. J.; Krestin, G. P. MRI of the Kidney—State of the Art. *Eur. Radiol* **2007**, *17*, 2780−2793.
(255) Hansen, K.; Nielsen, M.; Ewertsen, C. Ultrasonography of the Kidney: A Pictorial Review. *Diagnostics* **2016**, *6*, 2.
(256) Uppot, R. N.; Harisinghani, M. G.; Gervais, D. A. Imaging-Guided Percutaneous Renal Biopsy: Rationale and Approach. *American Journal of Roentgenology* **2010**, *194*, 1443−1449.
(257) Thompson, L. E.; Joy, M. S. Endogenous Markers of Kidney Function and Renal Drug Clearance Processes of Filtration, Secretion, and Reabsorption. *Curr. Opin Toxicol* **2022**, *31*, 100344.
(258) Burns, A. A.; Vider, J.; Ow, H.; Herz, E.; Penate-Medina, O.; Baumgart, M.; Larson, S. M.; Wiesner, U.; Bradbury, M. Fluorescent Silica Nanoparticles with Efficient Urinary Excretion for Nanomedicine. *Nano Lett.* **2009**, *9*, 442−448.
(259) Du, B.; Jiang, X.; Das, A.; Zhou, Q.; Yu, M.; Jin, R.; Zheng, J. Glomerular Barrier Behaves as an Atomically Precise Bandpass Filter in a Sub-Nanometre Regime. *Nat. Nanotechnol* **2017**, *12*, 1096−1102.
(260) Kang, H.; Gravier, J.; Bao, K.; Wada, H.; Lee, J. H.; Baek, Y.; El Fakhri, G.; Gioux, S.; Rubin, B. P.; Coll, J.; Choi, H. S. Renal Clearable Organic Nanocarriers for Bioimaging and Drug Delivery. *Adv. Mater.* **2016**, *28*, 8162−8168.
(261) Huang, J.; Jiang, Y.; Li, J.; He, S.; Huang, J.; Pu, K. A Renal-Clearable Macromolecular Reporter for Near-Infrared Fluorescence Imaging of Bladder Cancer. *Angew. Chem.* **2020**, *132*, 4445−4450.
(262) Yao, C.; Chen, Y.; Zhao, M.; Wang, S.; Wu, B.; Yang, Y.; Yin, D.; Yu, P.; Zhang, H.; Zhang, F. A Bright, Renal-Clearable NIR-II Brush Macromolecular Probe with Long Blood Circulation Time for Kidney Disease Bioimaging. *Angew. Chem., Int. Ed.* **2022**, *61*, No. e202114273.
(263) Antaris, A. L.; Chen, H.; Cheng, K.; Sun, Y.; Hong, G.; Qu, C.; Diao, S.; Deng, Z.; Hu, X.; Zhang, B.; Zhang, X.; Yaghi, O. K.; Alamparambil, Z. R.; Hong, X.; Cheng, Z.; Dai, H. A Small-Molecule Dye for NIR-II Imaging. *Nat. Mater.* **2016**, *15*, 235−242.
(264) Wang, W.; Ma, Z.; Zhu, S.; Wan, H.; Yue, J.; Ma, H.; Ma, R.; Yang, Q.; Wang, Z.; Li, Q.; Qian, Y.; Yue, C.; Wang, Y.; Fan, L.; Zhong, Y.; Zhou, Y.; Gao, H.; Ruan, J.; Hu, Z.; Liang, Y.; Dai, H. Molecular Cancer Imaging in the Second Near-Infrared Window Using a Renal-Excreted NIR-II Fluorophore-Peptide Probe. *Adv. Mater.* **2018**, *30*, 1800106.
(265) Yang, Y.; Wang, P.; Lu, L.; Fan, Y.; Sun, C.; Fan, L.; Xu, C.; El-Toni, A. M.; Alhoshan, M.; Zhang, F. Small-Molecule Lanthanide Complexes Probe for Second Near-Infrared Window Bioimaging. *Anal. Chem.* **2018**, *90*, 7946−7952.
(266) Li, Y.; Li, X.; Xue, Z.; Jiang, M.; Zeng, S.; Hao, J. Second Near-Infrared Emissive Lanthanide Complex for Fast Renal-Clearable in Vivo Optical Bioimaging and Tiny Tumor Detection. *Biomaterials* **2018**, *169*, 35−44.
(267) Huang, J.; Xie, C.; Zhang, X.; Jiang, Y.; Li, J.; Fan, Q.; Pu, K. Renal-clearable Molecular Semiconductor for Second Near-Infrared Fluorescence Imaging of Kidney Dysfunction. *Angew. Chem.* **2019**, *131*, 15264−15271.
(268) Poon, W.; Zhang, Y.-N.; Ouyang, B.; Kingston, B. R.; Wu, J. L. Y.; Wilhelm, S.; Chan, W. C. W. Elimination Pathways of Nanoparticles. *ACS Nano* **2019**, *13*, 5785−5798.
(269) Brenner, A. I.; Koshy, J.; Morey, J.; Lin, C.; DiPoce, J. The Bone Scan. *Semin Nucl. Med.* **2012**, *42*, 11−26.
(270) Chen, D.; Liu, Y.; Zhang, Z.; Liu, Z.; Fang, X.; He, S.; Wu, C. NIR-II Fluorescence Imaging Reveals Bone Marrow Retention of Small Polymer Nanoparticles. *Nano Lett.* **2021**, *21*, 798−805.
(271) Mi, C.; Zhang, X.; Yang, C.; Wu, J.; Chen, X.; Ma, C.; Wu, S.; Yang, Z.; Qiao, P.; Liu, Y.; Wu, W.; Guo, Z.; Liao, J.; Zhou, J.; Guan, M.; Liang, C.; Liu, C.; Jin, D. Bone Disease Imaging through the Near-Infrared-II Window. *Nat. Commun.* **2023**, *14*, 6287.

https://doi.org/10.1021/acs.chemrev.4c00835
Chem. Rev. 2025, 125, 5195−5227

(272) Chaffer, C. L.; Weinberg, R. A. A Perspective on Cancer Cell Metastasis. *Science* **2011**, *331*, 1559−1564.
(273) Fares, J.; Fares, M. Y.; Khachfe, H. H.; Salhab, H. A.; Fares, Y. Molecular Principles of Metastasis: A Hallmark of Cancer Revisited. *Signal Transduct. Target. Ther.* **2020**, *5*, 28.
(274) Valastyan, S.; Weinberg, R. A. Tumor Metastasis: Molecular Insights and Evolving Paradigms. *Cell* **2011**, *147*, 275−292.
(275) Ganesh, K.; Massagué, J. Targeting Metastatic Cancer. *Nat. Med.* **2021**, *27*, 34−44.
(276) Esposito, M.; Ganesan, S.; Kang, Y. Emerging Strategies for Treating Metastasis. *Nat. Cancer* **2021**, *2*, 258−270.
(277) Dogan, N. U.; Dogan, S.; Favero, G.; Köhler, C.; Dursun, P. The Basics of Sentinel Lymph Node Biopsy: Anatomical and Pathophysiological Considerations and Clinical Aspects. *J. Oncol* **2019**, *2019*, 1−10.
(278) Moncayo, V. M.; Aarsvold, J. N.; Alazraki, N. P. Lymphoscintigraphy and Sentinel Nodes. *J. Nucl. Med.* **2015**, *56*, 901−907.
(279) Vidal-Sicart, S.; Valdés Olmos, R. Using Lymphoscintigraphy as a Prognostic Tool in Patients with Cancer. *Res. Rep. Nucl. Med.* **2016**, *6*, 1.
(280) Li, J.; Chen, X.; Qi, M.; Li, Y. Sentinel Lymph Node Biopsy Mapped with Methylene Blue Dye Alone in Patients with Breast Cancer: A Systematic Review and Metaanalysis. *PLoS One* **2018**, *13*, No. e0204364.
(281) Maeda, H.; Nakamura, H.; Fang, J. The EPR Effect for Macromolecular Drug Delivery to Solid Tumors: Improvement of Tumor Uptake, Lowering of Systemic Toxicity, and Distinct Tumor Imaging in Vivo. *Adv. Drug Deliv Rev.* **2013**, *65*, 71−79.
(282) Ma, Z.; Wan, H.; Wang, W.; Zhang, X.; Uno, T.; Yang, Q.; Yue, J.; Gao, H.; Zhong, Y.; Tian, Y.; Sun, Q.; Liang, Y.; Dai, H. A Theranostic Agent for Cancer Therapy and Imaging in the Second Near-Infrared Window. *Nano Res.* **2019**, *12*, 273−279.
(283) Hong, L.; Li, W.; Li, Y.; Yin, S. Nanoparticle-Based Drug Delivery Systems Targeting Cancer Cell Surfaces. *RSC Adv.* **2023**, *13*, 21365−21382.
(284) Ling, M.; Sun, R.; Li, G.; Syeda, M. Z.; Ma, W.; Mai, Z.; Shao, L.; Tang, L.; Yu, Z. NIR-II Emissive Dye Based Polymer Nanoparticle Targeting EGFR for Oral Cancer Theranostics. *Nano Res.* **2022**, *15*, 6288−6296.
(285) Li, H.; Wang, M.; Huang, B.; Zhu, S.-W.; Zhou, J.-J.; Chen, D.-R.; Cui, R.; Zhang, M.; Sun, Z.-J. Theranostic Near-Infrared-IIb Emitting Nanoprobes for Promoting Immunogenic Radiotherapy and Abscopal Effects against Cancer Metastasis. *Nat. Commun.* **2021**, *12*, 7149.
(286) Tian, R.; Ma, H.; Zhu, S.; Lau, J.; Ma, R.; Liu, Y.; Lin, L.; Chandra, S.; Wang, S.; Zhu, X.; Deng, H.; Niu, G.; Zhang, M.; Antaris, A. L.; Hettie, K. S.; Yang, B.; Liang, Y.; Chen, X. Multiplexed NIR-II Probes for Lymph Node-Invaded Cancer Detection and Imaging-Guided Surgery. *Adv. Mater.* **2020**, *32*, 1907365.
(287) Zhou, H.; Yi, W.; Li, A.; Wang, B.; Ding, Q.; Xue, L.; Zeng, X.; Feng, Y.; Li, Q.; Wang, T.; Li, Y.; Cheng, X.; Tang, L.; Deng, Z.; Wu, M.; Xiao, Y.; Hong, X. Specific Small-Molecule NIR-II Fluorescence Imaging of Osteosarcoma and Lung Metastasis. *Adv. Healthc Mater.* **2020**, *9*, 1901224.
(288) Li, J.; Zhu, F.; Lou, K.; Tian, H.; Luo, Q.; Dang, Y.; Liu, X.; Wang, P.; Wu, L. Tumor Microenvironment Enhanced NIR II Fluorescence Imaging for Tumor Precise Surgery Navigation via Tetrasulfide Mesoporous Silica-Coated Nd-Based Rare-Earth Nanocrystals. *Mater. Today Bio* **2022**, *16*, 100397.
(289) Wang, P.; Fan, Y.; Lu, L.; Liu, L.; Fan, L.; Zhao, M.; Xie, Y.; Xu, C.; Zhang, F. NIR-II Nanoprobes in-Vivo Assembly to Improve Image-Guided Surgery for Metastatic Ovarian Cancer. *Nat. Commun.* **2018**, *9*, 2898.
(290) Traverso, N.; Ricciarelli, R.; Nitti, M.; Marengo, B.; Furfaro, A. L.; Pronzato, M. A.; Marinari, U. M.; Domenicotti, C. Role of Glutathione in Cancer Progression and Chemoresistance. *Oxid Med. Cell Longev* **2013**, *2013*, 1−10.
(291) Chen, S.; Li, S.; Wang, Y.; Chen, Z.; Wang, H.; Zhang, X.-D. Gold Nanoclusters for Tumor Diagnosis and Treatment. *Adv. Nanobiomed Res.* **2023**, *3*, 2300082.
(292) Bongsu, J.; Vullev, V. I.; Anvari, B. Revisiting Indocyanine Green: Effects of Serum and Physiological Temperature on Absorption and Fluorescence Characteristics. *IEEE J. Sel. Top. Quantum Electron.* **2014**, *20*, 149−157.

https://doi.org/10.1021/acs.chemrev.4c00835
Chem. Rev. 2025, 125, 5195−5227